

Drew University College of the Liberal Arts

Department of Chemistry

**Secondary Aerosol Formation from Heterogeneous Reactions Involving  
 $\alpha$ -(+)-Pinene and Kaolinite**

Baldwin Honors Thesis in Chemistry by Jed-Joan Edziah

May 2017

Committee:

Dr. Ryan Z. Hinrichs

Dr. Mary-Ann Pearsall

Dr. Robert Murawski

## **Acknowledgements**

I am grateful for the support of my professors, family and friends. I would like to thank Dr. Ryan Hinrichs, who was consistently supportive and provided me with the opportunity to study in his lab. My experience in the Hinrichs lab has challenged and inspired me; I will fondly remember how I developed as a chemist during this research project. I am grateful to Dr. Mary-Ann Pearsall and Dr. Robert Murawski who were valuable members of my thesis committee. I would like to thank my mom, Mercy Edziah, who is an example to me of the brilliance of women in science and the importance of a lifelong love of learning. Finally, I would like to thank my friends who cheered me on throughout this process. I am truly appreciative and blessed. Thank you!

## Table of Contents

Acknowledgements.....	1
Abstract.....	3
List of Frequently Used Abbreviations.....	4
<b>1.0. Introduction.....</b>	<b>5</b>
1.1. Secondary Organic Aerosols .....	5
1.2. Pinene Emission .....	11
1.3. SOA Formation from Gas-Phase Monoterpene Oxidation .....	15
1.4. SOA Formation from Heterogeneous Monoterpene Oxidation .....	30
<b>2.0. Modeling Heterogeneous Reactions of (<math>\alpha</math>)-(+)-Pinene and Kaolinite.....</b>	<b>38</b>
2.1. Fourier Transform Infrared Spectroscopy .....	38
2.2. Experimental Methods .....	48
<b>3.0. Reaction of <math>\alpha</math>-(+)-Pinene and Kaolinite at a Relative Humidity Level of 30% ...</b>	<b>52</b>
3.1. Experimental Details .....	52
3.2. DRIFTS Analysis .....	52
3.3. Product Analysis Using Gas Chromatography-Mass Spectrometry .....	62
3.4. Identification and Discussion of Dimer Products Using GC-MS .....	74
<b>4.0. The Effect of Relative Humidity on Reactions between (<math>\alpha</math>)-(+)-Pinene and Kaolinite.....</b>	<b>85</b>
4.1. The Importance of Relative Humidity in Atmospheric Chemistry .....	85
4.2. Modeling Water Uptake on the Kaolinite Surface .....	85
4.3. Assessing the Effect of Relative Humidity on Reactivity .....	96
<b>5.0. Placing Findings in the Context of Atmospheric Chemistry .....</b>	<b>100</b>
5.1. Calculating the Net Uptake Coefficient.....	100
5.2. Discussion.....	108
Bibliography .....	113

**Abstract**

Secondary organic aerosols (SOA) are an abundant class of atmospheric particulates that impact climate, human health, and atmospheric chemistry. While there is extensive research on gas-phase chemistry that converts volatile organic compounds to less volatile SOA components, heterogeneous pathways in which low volatility organic SOA components are produced from direct reactions of volatile organic compounds with mineral dust aerosols are not well characterized. To better understand this heterogeneous chemistry, we used diffuse reflectance infrared Fourier transform spectroscopy (DRIFTS) to monitor the formation of surface-adsorbed organic products from heterogeneous reactions between gaseous ( $\alpha$ )-(+)-pinene and kaolinite clay at various relative humidity levels. Gas chromatography and mass spectrometry identified  $\alpha$ -terpineol, fenchol, endo-borneol and high molecular weight dimers, which significantly increase SOA quantity and mass, as the major organic products. The rate of organic product formation inversely correlated with the relative humidity level indicating that  $\text{H}_2\text{O}_{(\text{g})}$  molecules compete with  $\alpha$ -pinene molecules for surface sites on kaolinite. Using a laminar flow reactor, the uptake coefficient for reactions between  $\alpha$ -pinene and kaolinite was calculated to be  $1.6 \times 10^{-6}$ . Kinetic and product analyses suggest that the reaction between kaolinite and ( $\alpha$ )-(+)-pinene leads to the formation of lower volatility organics that promote SOA production.

### **List of Frequently Used Abbreviations**

**CCN:** Cloud Condensation Nuclei

**POA:** Primary Organic Aerosol

**SOA:** Secondary Organic Aerosol

**VOC:** Volatile Organic Aerosol

**SVOC:** Semi-Volatile Organic Aerosol

**ELVOC:** Extremely Low Volatility Aerosol

**TgC:** Teragrams of Carbon

**IR/FTIR:** Infrared Spectroscopy/Fourier Transform Infrared Spectroscopy

**DRIFTS:** Diffuse Reflectance Fourier Transform Spectroscopy

**RH:** Relative Humidity

**scm:** Standard Cubic Centimeter per Minute

**GC-MS/MS:** Gas Chromatography-Mass Spectrometry/Mass Spectrometry

**BET Theory:** Brunauer–Emmett–Teller Theory

**LFR:** Laminar Flow Reactor

## **1.0. Introduction**

### **1.1. Secondary Organic Aerosols**

Aerosols are airborne solid and liquid particles that exist in the troposphere and have various sources and chemical properties; aerosols can impact climate, human health, and atmospheric chemistry. Aerosols can absorb and scatter solar radiation which allows them to affect atmospheric heating and cooling cycles (Hallquist et al., 2009). Aerosols are often hygroscopic; therefore, they provide surface area upon which water vapor can condense and ice crystals can form. This role enables aerosols to promote cloud formation by behaving as cloud condensation nuclei (CCN) or cloud seeds (Hallquist et al., 2009). Inhalation of aerosols, which may be toxic or mutagenic, has been linked to increased human mortality rates (Pandis et al., 1992; Baltensperger et al., 2008). Inhaled aerosols penetrate into lung tissue, inhibit the clearance of toxic material from alveoli and promote lung diseases (Gradon et al., 2000). The sizes of aerosol particles are on the order of micrometers; thus, aerosols can be dislodged from lung tissue, carried through the blood stream, and deposited into organs such as the liver, kidney and brain (Peters et al., 2006). The entry of these ultrafine particulates into the central nervous system is especially concerning because preliminary studies suggest that prolonged exposure to high aerosol concentrations may lead to the development of neurodegenerative diseases such as Alzheimer's and Parkinson's (Peters et al., 2006). Atmospheric aerosols can also react with trace gases, including anthropogenic pollutants such as ozone and nitrous oxide, and modify the tropospheric concentrations of these gases (Hallquist et al., 2009). The ability of aerosols to chemically react implies that their properties may be altered as they reside in the atmosphere for longer time periods. Although aerosols are often

classified by their size, the climate, health and atmospheric chemistry implications of aerosols vary with their chemical characteristics. Therefore, a comprehensive understanding of the climate, health, and atmospheric chemistry effects of aerosols necessitates analyses of their chemical composition, which depends on their source and formation pathways. The chemical compositions of aerosols are significantly affected by the chemical modifications that they undergo as a result of reactions with trace gaseous pollutants (i.e.  $\text{NO}_3$ ,  $\text{O}_3$ ,  $\text{HNO}_3$ ), volatile organic compounds and other atmospheric particulates.

Aerosols can be broadly classified according to their source and chemical composition. For instance, natural aerosols such as mineral dust and sea spray particles are characterized as both primary and predominantly inorganic, while primary organic aerosols (POAs) emitted from the burning of biomass can be considered as both natural and anthropogenic. Secondary organic aerosols (SOA) are not emitted directly into the atmosphere but are formed in the atmosphere as a result of chemical reactions that reduce the volatility of gaseous organic compounds. A reduction in the vapor pressure of a volatile organic compound (VOC) allows the VOC gas to condense into a liquid or semi-solid particle. The conglomeration of low-volatility organic compounds in the atmosphere leads to the formation of secondary organic aerosols (SOA). Relative to primary organic aerosols, which are emitted at a rate of approximately 35 teragrams of carbon (TgC) per year, secondary organic aerosols (SOA) are estimated to have atmospheric concentrations between 140 and 910 TgC annually (Hallquist et al., 2009). While primary aerosols are well characterized, secondary organic aerosols (SOA) are an abundant class of aerosols that are not extensively understood. Characterization of SOA

is therefore critical in order to assess the environmental and health implications of these particulates. This study investigates reactions between volatile organic compounds and mineral dust aerosols that may lead to the formation of SOA components in the atmosphere.

Volatile organic compounds (VOC) are released into the atmosphere by plants and gaseous pollution. Monoterpenes, which have the chemical formula  $C_{10}H_{16}$ , are the most important class of VOC because they contribute significantly to SOA formation and growth. Analyses of the chemical composition of SOA using chromatographic and spectroscopic techniques reveal that SOA are composed primarily of low volatility organic compounds that are generated from the oxidization of monoterpene compounds (Zhang et al., 2015; Rindelaub, 2016).

The formation of low volatility SOA components from gas-phase reactions of VOC with ozone and radical species (i.e.  $NO_3$  and OH) has been widely analyzed. In these gas-phase processes, ozone and radical species oxidize VOC to form oxygenated organic compounds that may be classified as semi-volatile or extremely low volatility organic compounds (SVOC/ELVOC) (Figure 1). The addition of oxygen atoms to VOC via chemical reactions increases their mass and more importantly enables them to participate in strong dipole-dipole intermolecular interactions; the net effect of these factors is a reduction in the vapor pressure of the VOC. Oxidized organic compounds with adequately low vapor pressures can partition to the condensed phase and contribute to the formation of new SOA or increase the size of a pre-existing SOA (Kroll & Seinfeld, 2008). It is important to consider that the chemical properties of SVOC/ELVOC may change once they become a part of a secondary organic aerosol because they



continue to react with the other chemical components that make up the mass of a secondary organic particulate. Therefore, relative to their precursors (i.e. monoterpene compounds), SOA are larger, structurally diverse and chemically complex (Hallquist et al., 2009).

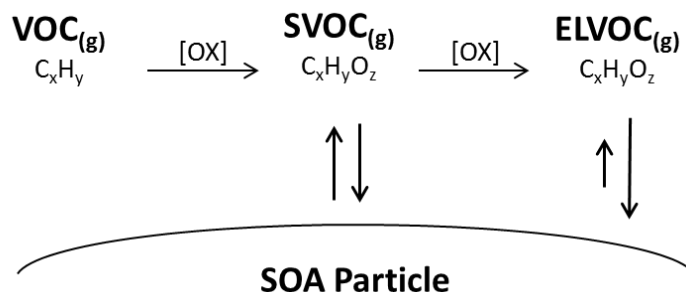


**Figure 1. Schematic of Gas-Phase SOA Formation and Growth.** [OX] = O<sub>3</sub>, NO<sub>3</sub>, OH or O<sub>2</sub>. VOC = volatile organic compound. SVOC = semi-volatile organic compound. ELVOC = extremely low volatility organic compound. SOA = secondary organic aerosol. The oxidation of VOC in the gas-phase forms less volatile SVOC/ELVOC products that can lead to new SOA formation or condense onto pre-existing SOA. ELVOC are more likely to partition into the condensed phase than SVOC because they are significantly less volatile.

This study focuses on heterogeneous pathways that lead to SOA formation and growth. Heterogeneous pathways involving reactions between volatile organic compounds and solid phase primary aerosols have not been thoroughly characterized. In these proposed heterogeneous pathways, VOC in the gas-phase collide with and react on the surfaces of solid phase primary or secondary aerosols. The surfaces of these particles often possess acidic and oxidative sites that facilitate the conversion of VOC to SVOC and ELVOC (Figure 2). In this study, we focus on reactions between (α)-(+)-pinene, an abundant VOC, and kaolinite, which is a clay component of mineral dust aerosols. We

assume that reactivity occurs immediately after ( $\alpha$ )-(+)-pinene collides with a reactive site on the kaolinite surface and that the VOC is not adsorbed to the surface.

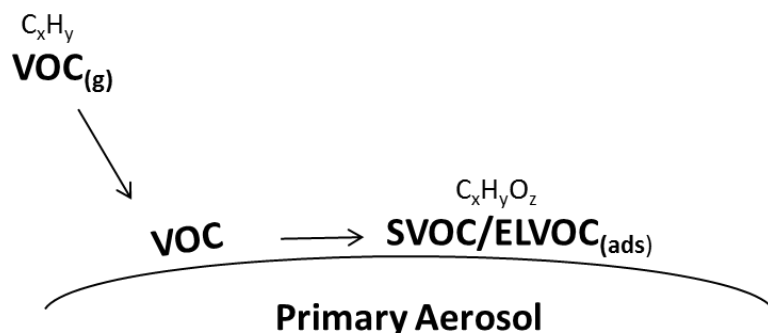


**Figure 2. Schematic of Heterogeneous SOA Formation and Growth.** VOC = volatile organic compound. SVOC = semi-volatile organic compound. ELVOC = extremely low volatility organic compound. In the heterogeneous pathway for SOA formation, lower volatility organics are formed on the surface of a primary aerosol.

SOA formation and growth via heterogeneous pathways differ significantly from gas-phase pathways because of the presence of a solid surface upon which organic compounds can react. It is significant to note that VOC, SVOC and ELVOC that are in contact with the surface of a mineral dust particle are not oxidized exclusively by the solid surface but can also be oxidized by atmospheric oxidants such as ozone,  $NO_3$  and OH. Therefore, heterogeneous pathways that lead to SOA formation and growth are quite complicated and difficult to fully characterize. Field and laboratory studies reveal that mineral aerosols significantly uptake strongly acidic oxides such as  $H_2SO_4$  and  $HNO_3$  in the atmosphere and demonstrate that heterogeneous pathways for SOA formation and growth are primarily acid catalyzed (Usher et al., 2003; Jang et al., 2002). Jang et al. observed that SOA yield as a result of heterogeneous reactions between organic aliphatic aldehydes and solid inorganic aerosols increased by a factor of 5 in the presence of oxoacids. Thus, the ability of heterogeneous pathways to contribute to SOA formation

may be strongly correlated with their ability uptake inorganic acids. Therefore, in heavily polluted environments where the concentrations of oxoacids are relatively higher, the impact of heterogeneous pathways on SOA formation may be more significant. Yet, most models used to predict global and regional SOA yields account primarily for the impact of gas-phase mechanisms and do not thoroughly account for the impact of heterogeneous pathways for SOA formation. Zheng et al. reported that in January 2013, pollution events in eastern and central China led to substantial haze formation that harmed the environment and human health in this region (2015). In order to model Eastern Asia's heightened atmospheric particulate matter, which they observed was composed primarily of inorganic sulfate, nitrate and ammonium, they explored the U.S. Environmental Protection Agency's WRF-CMAQ model for predicting atmospheric aerosol concentrations. The original WRF-CMAQ model accounts primarily for gas-phase and aqueous phase reaction mechanisms and led to normalized mean biases, which correlate to the mean error of a computational model, ranging from  $-40$  to  $-60$  %. Proposing that the missing source of particulate matter could be attributed to heterogeneous reactive pathways, Zheng et al. revised WRF-CMAQ to include 9 heterogeneous pathways in addition to the 2 heterogeneous pathways already present in the model. The revised WRF-CMAQ model yielded normalized mean biases ranging from  $-4.1$  to  $5.7$  % which evidenced a significant improvement in the accuracy of the model. Hence, while the production of SOA from heterogeneous reactions may likely not exceed those produced by gas phase mechanisms, comprehensive analyses of these pathways are necessary to fully characterize tropospheric SOA concentrations.

Incorporating heterogeneous pathways into models of atmospheric SOA will improve the accuracy of global SOA emission predictions and refine characterizations of the health, climate and atmospheric chemistry effects of SOA. Heterogeneous reactions between VOC and mineral aerosols may also lead to irreversible modifications of the chemical and physical properties of mineral particles. For example, the coating of mineral dust particles with organic compounds may add polar groups to the aerosol, thereby increasing its hygroscopicity, or may block the aerosol's surface sites. These factors can either enhance or reduce the aerosol's ability to serve as a cloud condensation nuclei (CCN) (Woodill et al., 2013). Chemical changes may impact the ability of a mineral aerosol to behave as an allergen and may increase its toxicity to human health systems (Hallquist et al., 2009). Organic coated mineral particles may have enhanced reactivity towards volatile organic compounds, HNO<sub>3</sub>, OH and ozone which may lead to ozone depletion and increases in SOA mass (Usher et al., 2003). This study proposes that reactions between VOC and mineral aerosols, in particular, are viable pathways to be considered for the formation and growth of SOA. In this study, ( $\alpha$ )-(+)-pinene, which is the most abundant monoterpene responsible for SOA, is used as a model VOC and kaolinite clay serves as a model for mineral dust aerosols.

## **1.2. Pinene Emission**

Pinene is a biogenic volatile organic compound (BVOC) that is emitted in significant quantities by a variety of plants. Pinene can also be synthetically produced and is used industrially as a solvent, as a flavoring agent, and for the preparation of other organic compounds. Pinene is often used for the production of household products and cosmetics because of its characteristic "pine" scent. Pinene exists as two primary

structural isomers:  $\alpha$ -pinene and  $\beta$ -pinene. Each isomer type has two main enantiomers that are referred to as the plus and minus forms (Figure 3). Pinene belongs to a class of compounds known as monoterpenes which are characterized by a molecular formula of  $C_{10}H_{16}$  and are the result of linking two isoprene compounds. Monoterpenes can be emitted into the atmosphere by gaseous pollution and by plants. The global emission of pinene varies greatly and is not well characterized. However, using the Model of Emissions of Gases and Aerosols from Nature (MEGAN), Sakulyanontvittaya et al. estimated that the emission of  $\alpha$ -pinene is approximately,  $370.4 \pm 367.7 \mu\text{g m}^{-2} \text{h}^{-1}$  in the United States (2008). Pinene is believed to be the most significant precursor VOC for the formation of secondary organic aerosols; therefore, the atmospheric chemistry of pinene is extensively studied.

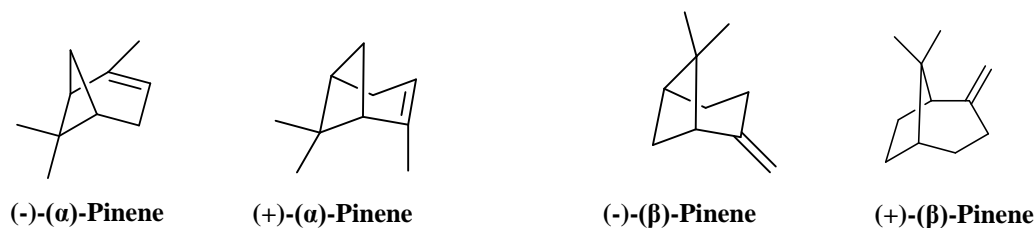


**Figure 3. Structural Forms of Pinene.** Structures to the left represent enantiomers of  $\alpha$ -pinene isomer and structures to the right represent enantiomers of  $\beta$ -pinene.

Natural pinene emissions vary with plant species and season, which encompasses differences in light intensity, temperature,  $\text{CO}_2$  concentration and humidity level (Loreto et al., 1996). In a study of monoterpene emission from *Pinus densiflora*, a species of red pine found in the northeast region of North America, increased monoterpene emission correlated with elevated light intensity and temperature; the effect of  $\text{CO}_2$  was not assessed in this particular study (Yokouchi & Ambe, 1984). For *Pinus densiflora*, at a

given intensity of light, the rate of  $\alpha$ -pinene release was found to be log-linearly correlated with temperature; this indicates that the rate of  $\alpha$ -pinene emission increased exponentially as temperature increased (Yokouchi & Ambe, 1984). These findings support the observed relationship between pinene emission and temperature cited in other studies (i.e. Loreto et al., 1996). Therefore, in coniferous plants, which usually emit larger quantities of pinene, temperature appears to be the main factor controlling pinene emission (Loreto et al., 1996; Yokouchi & Ambe, 1984). This suggests that increased global temperatures due to the greenhouse effect may increase pinene emission.

The abundance of  $\alpha$ -pinene in the atmosphere supports its use as a model VOC for the study of SOA formation. In a study of *Quercus ilex*, an evergreen plant found in the Mediterranean,  $\alpha$ -pinene accounted for 40 % of the total monoterpene emitted from this plant species (Loreto et al., 1996). The MEGAN calculations performed by Sakulyanontvittaya et al. estimated that  $\alpha$ -pinene accounted for approximately 15.6 % of the total monoterpene emissions in the United States (Table 1) (Figure 4). Thus, of the select monoterpenes analyzed in this study,  $\alpha$ -pinene had the highest relative emission rate followed by limonene (14.9 %), which is also commonly used as a model VOC in studies of SOA (i.e. Lederer et al., 2016).

Table 1: Emission Rates and Percentages for Select Monoterpenes in the United States		
	Emission Rate ( $\mu\text{g m}^{-2} \text{hr}^{-1}$ )	Approximate Percent of Total MT Emission (%)
Myrecene	$134.4 \pm 127.7$	5.64
Sabinine	$81.50 \pm 73.75$	3.42
Limonene	$355.0 \pm 360.1$	14.9
3-carene	$71.80 \pm 81.20$	3.02
<i>trans</i> - & $\beta$ -ocimene	$255.6 \pm 336.3$	10.7
$\beta$ -pinene	$199.2 \pm 180.6$	8.36
$\alpha$ -pinene	$370.4 \pm 367.7$	15.6
Other Monoterpenes	$913.5 \pm 895.5$	38.4
<b>Total Monoterpene Emission</b>	$2381 \pm 1114$	

**Table 1. Emission Rates and Percentages for Select Monoterpenes in the United States.** Adapted from MEGANv2.02 calculations reported by Sakulyanontvittaya et al., 2008. MT = monoterpene. Of the select monoterpenes analyzed,  $\alpha$ -pinene has the highest emission ( $370.4 \pm 367.7 \mu\text{g m}^{-2} \text{hr}^{-1}$ , 15.6 %) followed by limonene ( $355.0 \pm 360.1 \mu\text{g m}^{-2} \text{hr}^{-1}$ , 14.9 %). These estimates demonstrate that significant quantities of  $\alpha$ -pinene are emitted into the atmosphere.

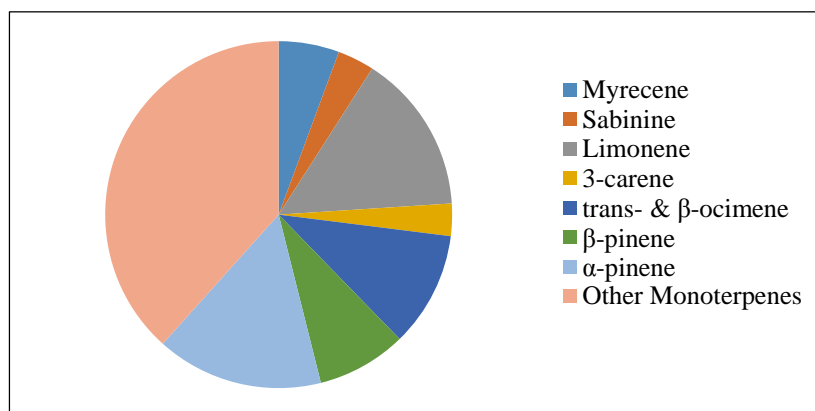


**Figure 4. Relative Emissions of Select Monoterpenes in the United States.** Adapted from MEGANv2.02 calculations reported by Sakulyanontvittaya et al., 2008. Demonstrates that of the select monoterpenes analyzed,  $\alpha$ -pinene accounts for the largest fraction of monoterpene emission, followed by limonene.

It is evident that significant quantities of  $\alpha$ -pinene are emitted into the atmosphere.

Therefore,  $\alpha$ -pinene can be considered a characteristic VOC for the study of SOA

formation. A large number of studies use  $\alpha$ -pinene to model both gas-phase and

heterogeneous reaction pathways that lead to SOA formation and growth (i.e. Zhang et

al., 2015). This study uses  $\alpha$ -pinene as a model for understanding heterogeneous pathways for secondary organic aerosol (SOA) formation and growth in the troposphere.

### 1.3. SOA Formation from Gas-Phase Monoterpene Oxidation

The general mechanism for the formation of SOA in the gas-phase involves the oxidation and subsequent condensation of gas-phase volatile organic compounds. The process of condensing a gas to a liquid or solid begins with nucleation and continues with growth.

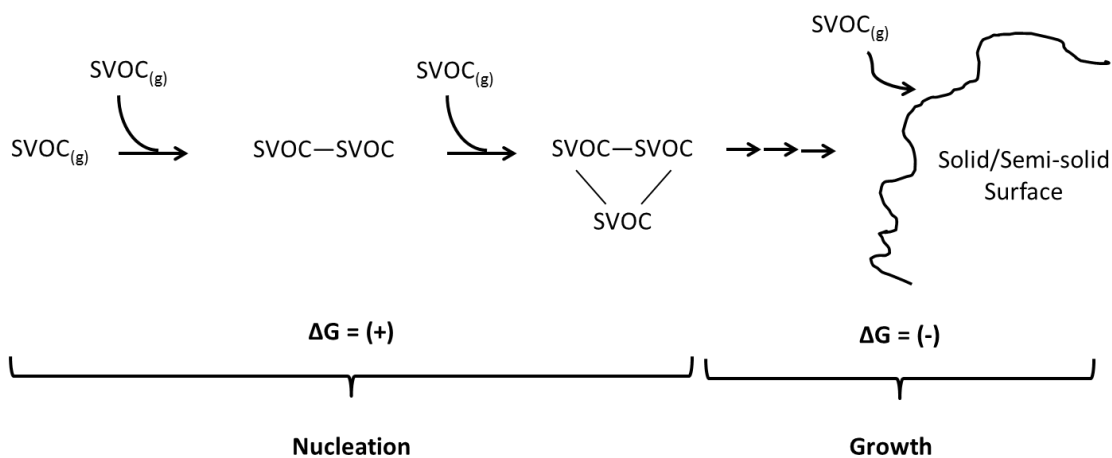


**Figure 5. Scheme of Gas-Phase Nucleation and Growth of SOA.** The entropic disadvantage of nucleation outweighs the enthalpic benefit which leads to a (+)  $\Delta G$  for nucleation process. Growth involves the condensation of liquid or low-volatility gaseous organics; this process is relatively more entropically favorable and is also enthalpically advantageous. Hence, the  $\Delta G$  of growth = (-), and we can understand how nucleation is more thermodynamically hindered than growth.

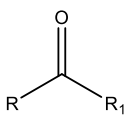
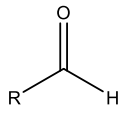
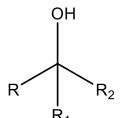
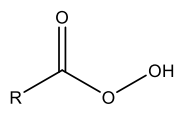
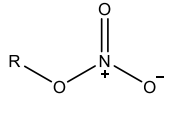
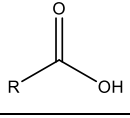
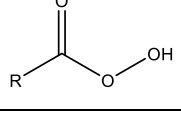
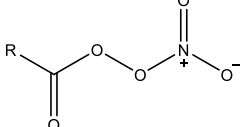
The conversion of a gas to a condensed phase is a more thermodynamically drastic process relative to the condensation of a liquid or low-volatility gas unto a solid. Gas molecules are more dispersed and experience far lesser intermolecular interactions relative to liquids and solids. Thus, the process of nucleation has a high free energy barrier because of the unfavorable change in entropy associated with converting a gas to a



liquid or solid cluster without a substantial enthalpic benefit (Figure 5). While the growth of an SOA is not entropically favorable, it is relatively enthalpically favorable because condensed organics can experience significant intermolecular interactions with one another and with the particle surface. Hence, the free energy barrier for the growth of an SOA is relatively lower than the free energy barrier for nucleation, which most studies of gas-phase SOA refer to as new particle formation. Some studies propose that new SOA formation is initiated by the formation of clusters of sulfuric acid ( $\text{H}_2\text{SO}_4$ ), ammonia ( $\text{NH}_3$ ) and water that range between 1 and 2 nm in size (Laaksonen et al., 2008). The ability of these molecules to form strong dipole-dipole and hydrogen bonding interactions likely increases the favorability of their nucleation (Laaksonen et al., 2008). Yet the observation of new SOA in regions where sulfuric acid concentrations are low (i.e. coniferous forests) raises the question of how SOA are formed in such environments. In order to answer this question, Laaksonen et al. assessed the chemical compositions of new SOA particles formed in Finland's Hyytiälä forestry field station using an aerodyne aerosol mass spectrometer (AMS) and an ultrafine organic tandem differential mobility analyzer (UFO-TDMA). Laaksonen et al. found that the AMS mass spectra for large (300 – 700 nm) and small (< 200 nm) particulates were identical and composed primarily of oxidized forms of  $\alpha$ -pinene. The observation that newly nucleated particles (approximately 10 nm in size) were also significantly made up of oxidized  $\alpha$ -pinene molecules led Laaksonen et al. to conclude that especially in boreal forest environments, new SOA particle formation was controlled by the nucleation of oxidized monoterpenes rather than sulfuric acid. Overall, nucleation processes that initiate gas-phase SOA formation are quite difficult and complicated. When extant particles (i.e. mineral dust and

other solid or semi-solid seed particles) are present in the gas-phase, nucleation is not necessary for SOA formation because the extant particles provide surface area upon which a gaseous organic compound can condense. Many studies of gas-phase SOA use seed particles, which are usually inorganic solids such as ammonium sulfate, in order to bypass the process of nucleation and to focus solely on SOA particle growth (i.e. Ehn et al., 2014). However, we demonstrate in this study that SOA can form by growth on mineral dust surfaces without gas-phase oxidation.

A VOC can undergo condensation only if it experiences a significant reduction in its vapor pressure. Increasing the molecular weight of a VOC or adding oxygen containing groups to its structure via an oxidative pathway are two common methods by which the vapor pressure of a VOC can be reduced. An increase in molecular weight correlates with an increase in the electron density of a VOC which increases its London dispersion force attractions, while the addition of polar groups allow a VOC to participate in relatively stronger dipole-dipole intermolecular interactions. These two effects inhibit the molecules of a VOC from escaping into the gas-phase and explain how the addition of atoms and polar groups to a VOC can lead to considerable reductions in vapor pressure. Table 2 summarizes the multiplicative factors by which the vapor pressure of a VOC can change upon the addition of various oxygen-containing functionalities. The values cited in Table 2 reveal that the oxidation of a VOC can lead to substantial reductions in its vapor pressure.

Table 2: Multiplicative Changes to VOC Vapor Pressure by Various Functional Groups		
Functional Group Addition	Structure	Multiplicative Change in Vapor Pressure (298 K)
Ketone	-C(O)- 	0.10
Aldehyde	-C(O)H 	0.085
Alcohol	-OH 	$5.7 \times 10^{-3}$
Hydroperoxyl	-OOH 	$2.5 \times 10^{-3}$
Nitrate	-ONO <sub>2</sub> 	$6.8 \times 10^{-3}$
Carboxylic Acid	-C(O)OH 	$3.1 \times 10^{-4}$
Peroxyacid	-C(O)OOH 	$3.2 \times 10^{-3}$
Acyl peroxyxynitrate	-C(O)OONO <sub>2</sub> 	$2.7 \times 10^{-3}$

**Table 2. Multiplicative Changes to VOC Vapor Pressure by Various Functional Groups.** Adapted from Kroll & Seinfeld, 2008. [R, R<sub>1</sub>, R<sub>2</sub>] represent any additional chemical group. Oxidation of VOC by complex mechanisms involving OH radicals, O<sub>3</sub>, and NO<sub>3</sub> radicals results in the addition of functionalities to the VOC that greatly reduce vapor pressure by 90 to 99 %.

The addition of a ketone, which represents the smallest change in vapor pressure cited in Table 2, results in an order of magnitude reduction in VOC vapor pressure. The polarity of the C=O bond in a ketone allows a molecule to participate in dipole-dipole intermolecular interactions that inhibit it from entering into the gas-phase. Table 2 reveals that the addition of polar groups containing alcohol (OH) groups leads to vapor pressure reductions of 3 to 4 orders of magnitude. These more substantial decreases in volatility can be attributed to the strong hydrogen bonding interactions in which OH groups can participate. While N-O bonds are less polar than C-O bonds, the addition of NO<sub>2</sub> groups via nitrate or acyl peroxy nitrate functionalities also correlate to vapor pressure reductions of 3 orders of magnitude. Thus, the significant vapor pressure reduction caused by nitrate and acyl peroxy nitrate groups may be due to the fact that these functionalities contain multiple oxygen atoms, which would lead to increased dipole-dipole intermolecular interactions. Overall, the values presented in Table 2 are consistent with our understanding of intermolecular forces. The strengthening of intermolecular interactions by the addition of various functionalities has significant implications for SOA formation and growth. When oxidation of a VOC leads to a sufficient decrease in its vapor pressure, the less volatile organic compound is more likely to nucleate, which forms a new particulate, or condense on a pre-existing solid or semi-solid surface. The condensation of low volatility organics onto solid or semi-solid surfaces leads to SOA growth; therefore, the oxidation of volatile organic compounds in the gas phase promotes secondary organic aerosols.

VOC oxidation in the gas phase by ozone (O<sub>3</sub>), hydroxyl (OH) radicals, and nitrate (NO<sub>3</sub>) radicals leads to the formation of low volatility organics that contribute to

SOA formation and size (Kroll & Seinfeld, 2008). These oxidants add oxygen containing functionalities to VOC by various complex mechanisms which reduce the vapor pressure of the VOC thereby allowing it to partition into the condensed phase (Kroll & Seinfeld, 2008). While they are not outlined in this study, some gas-phase pathways may be reversible under certain conditions while others may lead to higher volatility products such as acetone, formaldehyde, CO<sub>2</sub> and NO<sub>2</sub> (Kroll & Seinfeld, 2008). Figure 6 presents the major products formed when  $\alpha$ -pinene is oxidized by O<sub>3</sub>, OH, and NO<sub>3</sub>. Figure 6 reveals that pinonaldehyde is a common major product of  $\alpha$ -pinene oxidation by OH, O<sub>3</sub> and NO<sub>3</sub> in the gas-phase. The presence of an aldehyde and a ketone in the structure of pinonaldehyde results in a significant reduction in the vapor pressure of  $\alpha$ -pinene. While pinonaldehyde is the most significant common major product,  $\alpha$ -pinene oxidation by OH, O<sub>3</sub> and NO<sub>3</sub> produces common trace products such as pinonic acid, norpinonic acid, norpinonaldehyde, and pinic acid (Zhang et al., 2015; Jang and Kamens, 1999; Capouet et al., 2004; Perraud et al., 2010). Figure 6 illustrates that the products of  $\alpha$ -pinene oxidation by different oxidants leads to variability in the product types and yields. While pinic acid is not abundantly generated, the presence of 2 carboxylic acid groups in the molecule's structure corresponds to a substantial vapor pressure reduction and indicates that O<sub>3</sub> is perhaps the most important gas-phase pathway for the formation of low-volatility organic compounds. Although Figure 6 depicts the notable gas-phase products of  $\alpha$ -pinene oxidation, not all of the products presented contribute to the formation or growth of SOA; thus, it is necessary to keep in mind that the volatility of a gas-phase organic product controls whether it will partition into the condensed phase and contribute to SOA.

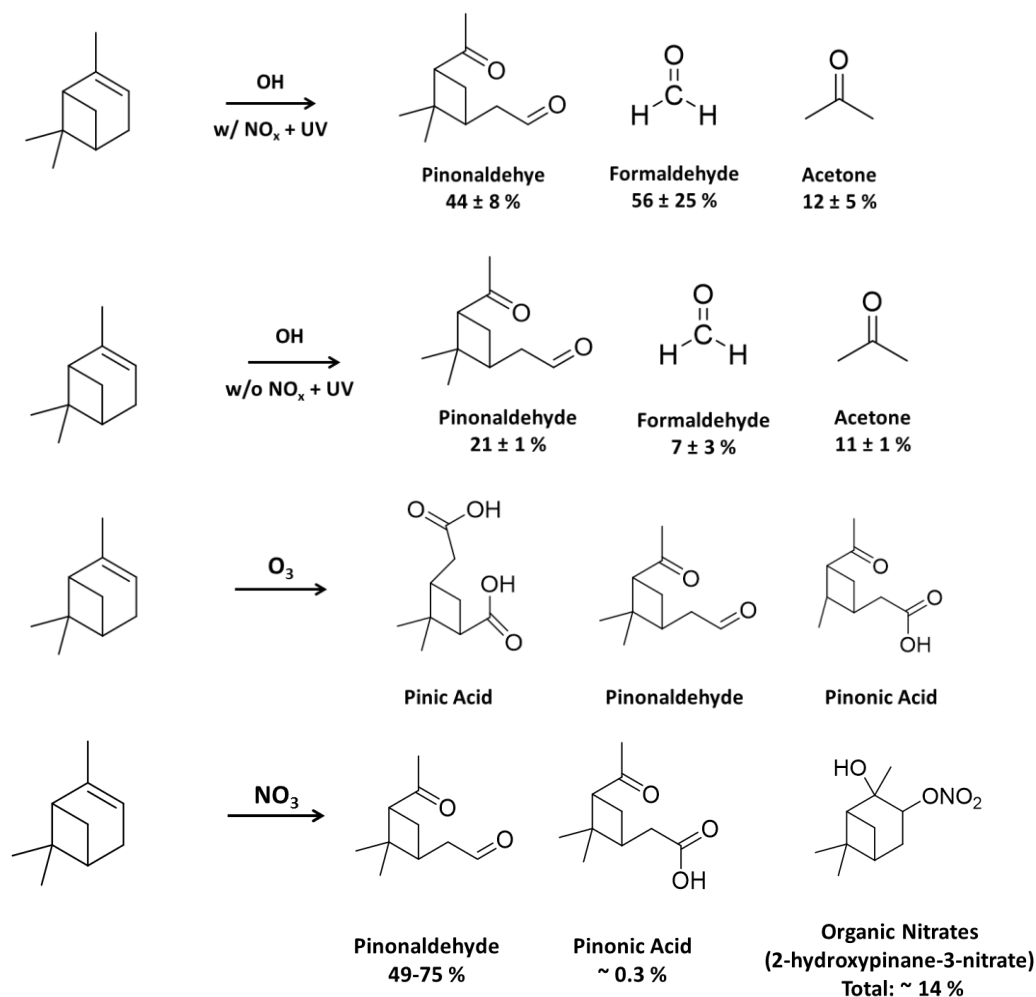


**Figure 6. Major Products of  $\alpha$ -Pinene Oxidation by OH, O<sub>3</sub>, and NO<sub>3</sub> in the Gas-phase.** Adapted from (Zhang et al., 2015), (Jang and Kamens, 1999), (Capouet et al., 2004), and (Perraud et al., 2010). Reveals that pinonaldehyde is a common major organic product of  $\alpha$ -pinene oxidation by OH, O<sub>3</sub>, and NO<sub>3</sub>. Illustrates that different gas-phase oxidants result in products with differing structures, volatilities and yields.

For heterogeneously produced  $\alpha$ -pinene oxidation products, which are the focus of this study, volatility likely determines whether products remain adsorbed to a surface and thereby contribute to SOA, or desorb. However, for now, we will consider gas-phase  $\alpha$ -pinene oxidation initiated by OH, NO<sub>3</sub> and O<sub>3</sub> in greater detail.

Gas-phase oxidative processes involving  $\alpha$ -pinene have been extensively studied and characterized. A comprehensive mechanism for the OH radical initiated oxidation of

$\alpha$ -pinene was proposed by Capouet et al. using a theoretical box model of laboratory simulations generated from structure activity relationships (SARs), density functional theory (DFT) and statistical rate theories (Capouet et al., 2004). The calculations were validated using laboratory experiments involving Fourier transform infrared spectroscopy (FTIR). Capouet et al. compared their experimental and computational product yields for reactions between  $\alpha$ -pinene and OH at varying conditions involving UV light, visible light and NO<sub>x</sub>. For pinonaldehyde, acetone, and formaldehyde, the percent differences (%) between the experimental and computational yields were approximately 12, 5.8, and 60, respectively. This reveals that the computational values are most accurate when predicting pinonaldehyde and acetone yields from reactions between OH and  $\alpha$ -pinene. The production of formaldehyde and acetone, which have very few atoms and therefore weak intermolecular interactions, reveals that gas-phase pathways of monoterpene oxidation do not lead solely to less volatile organics. Thus, in the context of SOA, pinonaldehyde is really the sole significant product of OH initiated  $\alpha$ -pinene oxidation. Having evaluated the accuracy of their model, Capouet et al. used the model to outline the mechanism for the formation of pinonaldehyde from the reaction of  $\alpha$ -pinene and OH. The initial oxidation of  $\alpha$ -pinene by OH radicals leads to the formation of three primary intermediates that are generated either by a hydrogen abstraction pathway or a hydroxyl addition pathway (Figure 7).

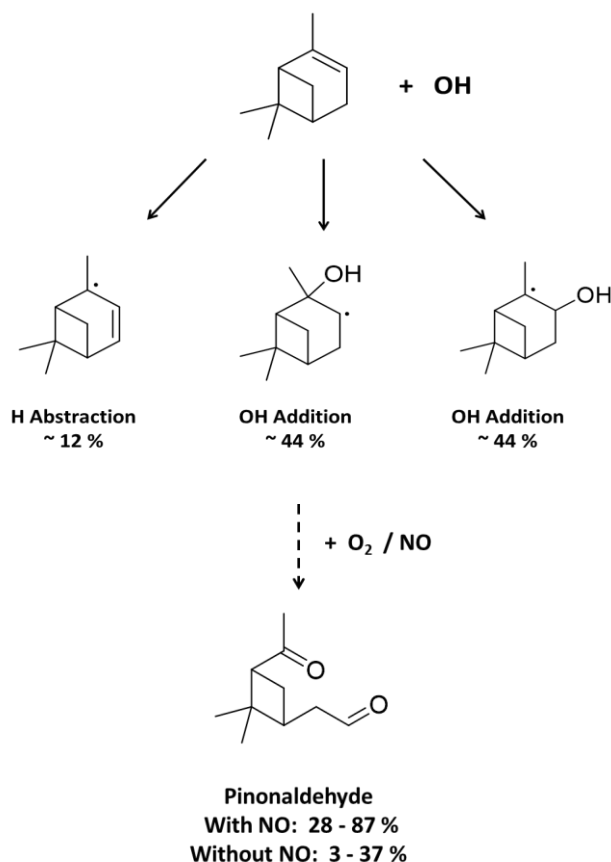


**Figure 7. Hydroxyl Radical Initiated  $\alpha$ -Pinene Oxidation in the Gas-phase.** Adapted from Capouet et al., 2004. Note: product yields presented are per step and do not represent overall yields. Initial oxidation products are produced via hydrogen abstraction or hydroxyl addition. Additional oxidation of these initial products by O<sub>2</sub> or NO leads to the formation of pinonaldehyde which is a significant low-volatility product of OH-initiated  $\alpha$ -pinene oxidation.

As depicted by Figure 7, products formed by means of OH addition accounted for approximately 88 % of the product yielded after the initial oxidation step while the radical compound formed by hydrogen abstraction accounted for 12 % of the product yield following the initial oxidation step. Following the initial oxidation step, other oxidants such as O<sub>2</sub> and NO can interact with the lower volatility organic intermediates to form progressively less volatile organics. In the OH initiated pathways reported by Capouet et al., pinonaldehyde was among the major organic products generated, and in the presence of NO<sub>x</sub>, the yield of pinonaldehyde increased from 3 – 37 % to 28 – 87 %.



These findings indicate that  $\alpha$ -pinene and its oxidized derivatives are considerably reactive in the presence of nitrogen-containing oxidants.

The reactivity of nitrogen-containing oxidants and  $\alpha$ -pinene was also studied by Perraud et al. who performed and analyzed the  $\text{NO}_3$  radical initiated oxidation of  $\alpha$ -pinene using atmospheric pressure chemical ionization mass spectrometry (APCI-MS) (Perraud et al., 2010). The formation of pinonaldehyde (mwt = 168 amu) from the oxidation of  $\alpha$ -pinene by a nitrogen-containing oxidant was verified by a m/z peak of 169 in the mass spectra of their products, which they attributed to the presence of a [pinonaldehyde-hydrogen]<sup>+</sup> ion. Perraud et al. also observed an ion at 185 m/z which they attributed to pinonic acid (mwt = 184 amu). They reported that the vapor pressure of pinonic acid was 2 orders of magnitude less than that of pinonaldehyde and that this property directly correlated with their observation that pinonic acid accounted for a greater composition of the SOA mass produced. Perraud et al. suggest that pinonic acid's lower vapor pressure allowed it partition into the condensed phase and serve as a surface upon which semivolatile organic compounds can condense. These findings highlight how variations in the vapor pressures of  $\alpha$ -pinene-derived low volatility products lead to differences in the ability of each product to contribute to SOA formation. This suggests that significantly low volatility organic products in the gas-phase control SOA particle quantity and size.

Dimers are a class of extremely low volatility organic compounds (ELVOC) that significantly impact SOA formation and size. Organic dimers are oligomers composed of two monomer compounds which are structurally similar and joined by covalent bonds. In this study, " $\alpha$ -pinene-derived dimers" will not refer to compounds containing two pinene

molecules, but will rather reference high molecular weight products of  $\alpha$ -pinene oxidation processes that have between 15 and 20 carbon atoms and variable quantities of oxygen and hydrogen atoms. The significantly larger molecular weights and lower vapor pressures of dimers relative to their parent VOC makes them more likely to exist in the condensed phase. This allows dimers to serve as surface sites for the condensation of other low volatility products. Thus, dimers play a key role in SOA.

Organic dimers formed from gas-phase reactions between  $\alpha$ -pinene and ozone were analyzed by Zhang et al. who synthesized SOA derived from reactions of  $\alpha$ -pinene and ozone at varying conditions. Zhang et al. used liquid chromatography and mass spectrometry (LC-MS) following electrospray ionization to characterize the organic products of this reaction after they were separated from the bulk SOA mass (Zhang et al., 2015). Once again, it is significant to note that the organic products that are part of an SOA may be chemically distinct from gas-phase products because gas-particle partitioning is controlled by volatility and organic products may undergo chemical changes as a result of interactions with SOA components once they partition into the particle phase. Thus, the products of  $O_3$ -initiated  $\alpha$ -pinene oxidation reported in Figure 6 comprise only a fraction of the organic SOA components analyzed by Zhang et al. The organic components of the SOA were characterized by mass saturation concentration into extremely low volatility (ELVOC:  $< 3 \times 10^{-4} \mu\text{g m}^{-3}$ ), low volatility (LVOC:  $3 \times 10^{-4}$ - $0.3 \mu\text{g m}^{-3}$ ), semivolatile (SVOC:  $0.3$ - $300 \mu\text{g m}^{-3}$ ), and intermediate volatility (IVOC:  $300$ - $3 \times 10^6 \mu\text{g m}^{-3}$ ) organic compounds (Zhang et al., 2015). SVOC were found to be the major components in SOA derived from gas-phase reactions between  $\alpha$ -pinene and ozone. Zhang et. al reported that while dimers constituted less than 45% of the total SOA mass,

ELVOC (dimer) products ( $C_{14-19}H_{24-28}O_{5-9}$ ) were produced, initially, at a faster rate than SVOC/LVOC (monomer) products. This indicates that gas-phase dimer formation is kinetically favorable (Zhang et al., 2015). Zhang et al. suggest that compounds with the molecular formulas  $C_8H_{11}O_4$  and  $C_9H_{13}O_4$  are among the major building blocks of the dimer products that constitute gas-phase  $\alpha$ -pinene-derived SOA. The mechanism and structure for the formation of a dimer ( $C_{17}H_{26}O_6$ ) produced by Zhang et al. (and for pinic acid) is outlined in Figure 8.

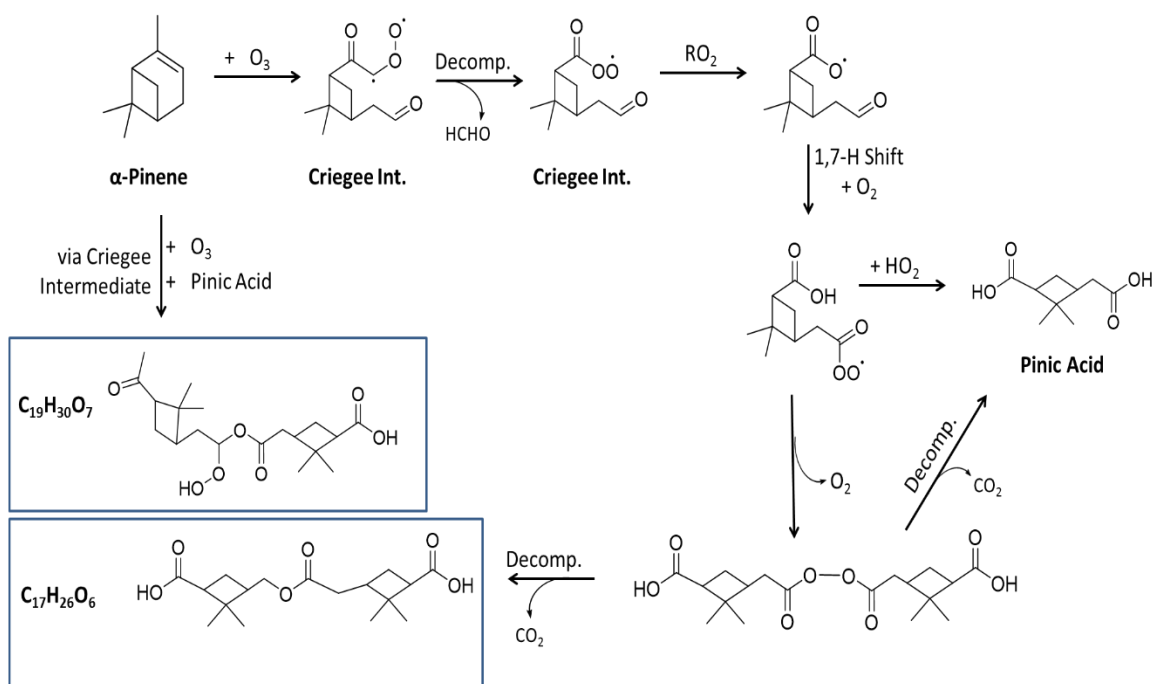


**Figure 8. Mechanism and Structure of  $\alpha$ -Pinene Derived Dimer Products and Pinic Acid.** Adapted from Zhang et al., 2015 and Kristensen et al., 2016. Dimers derived from reaction between  $\alpha$ -pinene and ozone possess multiple oxygen-containing functionalities indicating that the compounds have considerably low vapor pressures. This scheme also outlines the formation of pinic acid which is present both in the gas-phase and in the particle phase.

The dimers observed by Zhang et al., like the structure of the  $C_{17}H_{26}O_6$  compound depicted in Figure 8, contained primarily ester functionalities along with carboxylic acid and alcohol groups. Figure 8 includes the formation of a dimer ester compound

( $C_{19}H_{30}O_7$ ) proposed by Kristensen et al. which is formed as a result of  $\alpha$ -pinene ozonolysis via a slightly different Criegee intermediate than the one shown for the formation of  $C_{17}H_{26}O_6$  (2016). The dimers detected by Zhang et al. were a result of ozonolysis reactions of  $\alpha$ -pinene in the presence of ammonium sulfate seed particles which were used to initiate SOA formation. Likewise, Ehn et al. observed dimers generated in the Jülich Plant Atmosphere Chamber (JPAC) from ozone initiated  $\alpha$ -pinene oxidation in the presence of ammonium sulfate seed aerosols. The dimers observed by Ehn et al. were characterized by molecular formulas of  $C_{19-20}H_{28-32}O_{10-18}$  and were significant components of SOA mass (Ehn et al., 2014). The use of solid ammonium sulfate aerosols (10 nm) for the seeding or initiation of SOA formation resulted in the decline of the relative concentrations of the ELVOC products. This observation was coupled with an increase in the SOA mass yield from 1% to 10%. While the decline of ELVOC production may be due to diffusion-limiting affects, these findings point to the ability of inorganic aerosols to impact SOA formation.

The role of inorganic seed aerosols in SOA formation was studied by Inuma et al. who performed ozonolysis reactions of limonene in the presence of neutral ( $Na_2SO_4$ ), acidic ( $(NH_4)_2SO_4/H_2SO_4$ ) and strongly acidic ( $H_2SO_4$ ) solid or liquid sulfate seed particles. Using high pressure liquid chromatography (HPLC) and mass spectrometry (MS), Inuma et al. compared the total organic compound (TOC) produced in the presence of these seed particles. Inuma et al. used high temperature conditions in order to volatilize the organic products formed using the various seed particles; they observed that at 650 °C, the change in total organic product ( $\Delta TOC$ ) ( $\mu g C m^{-3}$ ) for  $Na_2SO_4$ ,  $(NH_4)_2SO_4/H_2SO_4$ , and  $H_2SO_4$  were  $121 \pm 11$ ,  $109 \pm 7$ , and  $89.6 \pm 11.1$ , respectively

(Iinuma et al., 2007). When the temperature was raised to 850 °C, the  $\Delta$ TOC values for products formed in the presence of  $\text{Na}_2\text{SO}_4$  and  $(\text{NH}_4)_2\text{SO}_4/\text{H}_2\text{SO}_4$  remained the same while the  $\Delta$ TOC for  $\text{H}_2\text{SO}_4$  increased by  $20 \mu\text{g C m}^{-3}$ . Iinuma et al. propose that this difference in organic product formation in the presence of  $\text{H}_2\text{SO}_4$  seeds is due to the formation of acid-catalyzed high molecular weight sulfur-ester dimers with  $m/z$  465 ( $\text{C}_{20}\text{H}_{33}\text{O}_{10}\text{S}^-$ ) and  $m/z$  485 ( $\text{C}_{20}\text{H}_{33}\text{O}_{11}\text{S}^-$ ). Figure 9 outlines a mechanistic pathway proposed by Iinuma et al. for the formation of the sulfate-ester dimers from limonaldehyde, which is a product of limonene ozonolysis.

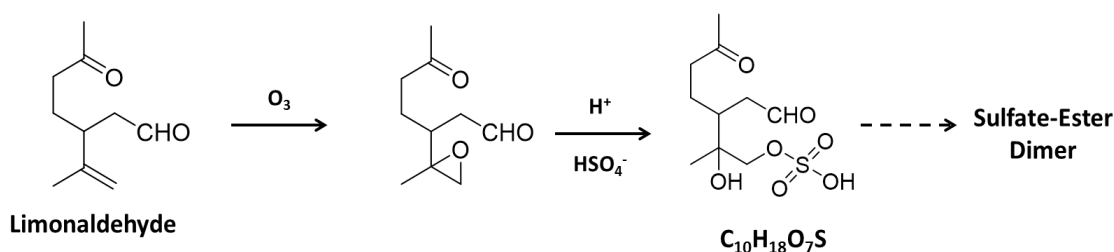


**Figure 9. Proposed Mechanistic Pathway for the Formation of Limonene-Derived Sulfate-Ester Dimers.** Adapted from Iinuma et al., 2007. The formation of sulfur containing dimers from oxidation products of limonene and  $\text{O}_3$  in the presence of  $\text{H}_2\text{SO}_4$  seed particles indicates that dimers are formed by both gas-phase and heterogeneous phase reactions.

As illustrated in the above mechanism, Iinuma et al. suggest that sulfate-ester dimers were formed from the oxidation products of limonene ozonolysis. Their idea that dimers are formed from oxidized monoterpene products corroborates with the observations and proposed mechanism reported by Zhang et al. for  $\alpha$ -pinene-derived dimers in the presence of  $\text{O}_3$ . The observation of Iinuma et al. that dimers formed using  $\text{H}_2\text{SO}_4$  seed particles contained sulfur atoms suggests that dimer formation occurred as a result of heterogeneous chemical reactions between the oxidized products and the seed aerosols. The gas-phase mechanisms for SOA formation that we have considered have revealed that low volatility organics, especially dimers, contribute significantly to SOA mass and

formation. Thus, the presence of sulfur atoms in the dimers identified by Iinuma et al. suggests that SOA can be produced via both gas-phase and heterogeneous pathways. Based on the findings of Iinuma et al., heterogeneous pathways for SOA formation are likely primarily acid catalyzed. Thus, Zhang et al. and Ehn et al. did not observe heterogeneous reactivity likely because the ammonium sulfate seeds they used were not sufficiently acidic. Duporte et al. studied reactions between the products of  $\alpha$ -pinene ozonolysis and acidified ammonium sulfate particles using liquid chromatography coupled with high-resolution quadrupole time-of-flight mass spectrometry and electrospray ionization (2016). Duporte et al. observed the production of organosulfate (R-OSO<sub>3</sub>H) dimers that indicated heterogeneous reactivity; Figure 10 outlines the mechanisms and structures of the observed dimer products.

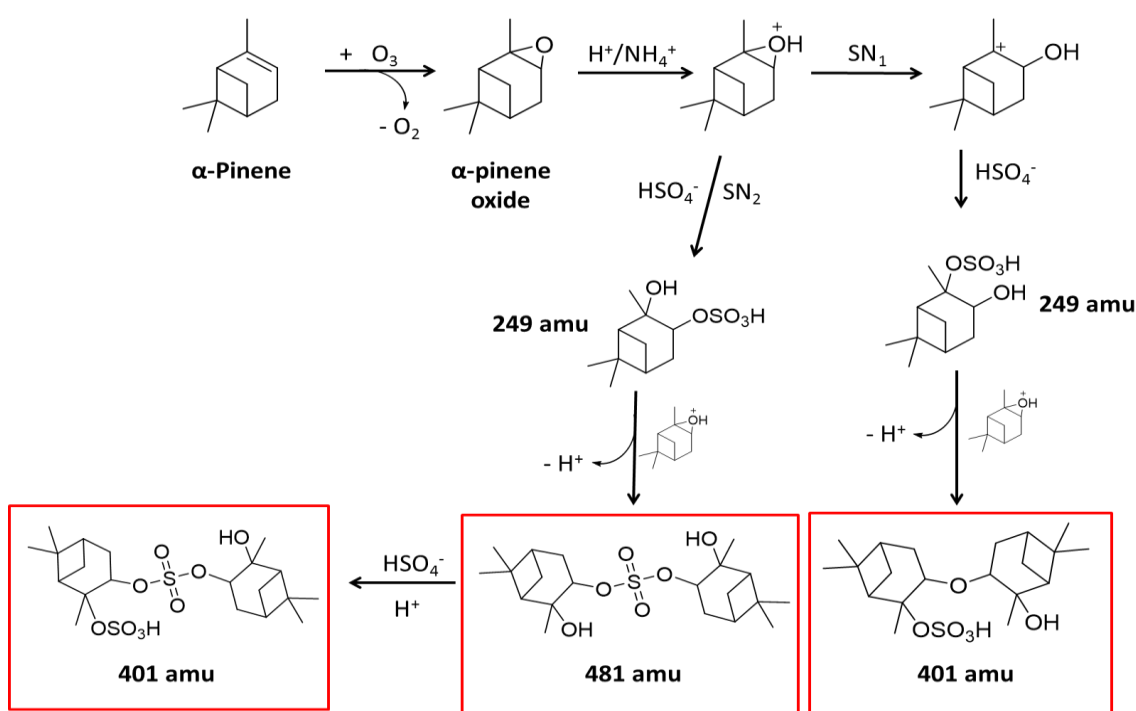


**Figure 10. Mechanisms and Structures for the Formation of  $\alpha$ -Pinene Derived Organosulfate Dimer Products.** Adapted from Duporte et al., 2016. A product of  $\alpha$ -pinene ozonolysis ( $\alpha$ -pinene oxide) was reacted with ammonium sulfate particles to yield higher molecular weight organosulfate dimer compounds. The presence of sulfates in the dimers indicates that heterogeneous reactivity occurred.

The dimer products observed by Duporte et al. generally have molecular weights above 400 amu and are formed by the linkage of oxidized monomer products via an oxygen-containing functionality. The presence of sulfate and alcohol groups in these dimers indicates that they have extremely low volatilities and are likely irreversibly bound to the surface of the ammonium sulfate particles. Hence, these dimer compounds are viable components of SOA. This study examines the formation of SOA components from reactions between ( $\alpha$ )-(+)-pinene and kaolinite clay, which is a major clay component of mineral dust.

#### **1.4. SOA Formation from Heterogeneous Monoterpene Oxidation**

Mineral dust particles are a significant portion of primary, inorganic atmospheric aerosols and we propose that they can act as seeds for SOA via unique heterogeneous pathways. Like other aerosols, mineral dust aerosols can affect atmospheric processes and atmospheric chemistry. Perhaps the longest range atmospheric impact that mineral particles can have involves their role in cloud formation by acting as cloud condensation nuclei. Mineral aerosols can serve as cloud condensation nuclei (CCN) by providing surface sites upon which water vapor can partition into the condensed phase (Usher et al., 2003). By serving as CCN, mineral particles can promote cloud formation and impact climate. Mineral surfaces can uptake trace gases (i.e.  $\text{HNO}_3$  (g)); therefore, mineral aerosols can alter atmospheric concentrations of these gases. The surfaces of mineral aerosols can also facilitate heterogeneous reactions involving volatile organic compounds in the atmosphere.

Studying the atmospheric impact of mineral aerosols is relevant because substantial emissions of mineral aerosols into the atmosphere occur globally and

annually. Figure 11 illustrates that large quantities of mineral dust are emitted into the atmosphere from arid regions (the Sahara in Figure 11). Emissions of mineral dust particles differ considerably in varying regions and seasons. However, the global emission of mineral dust aerosols ranges from 1000 to 3000 Tg per year, which is two orders of magnitude larger than the emission of volatile organic compounds (Usher et al., 2003).

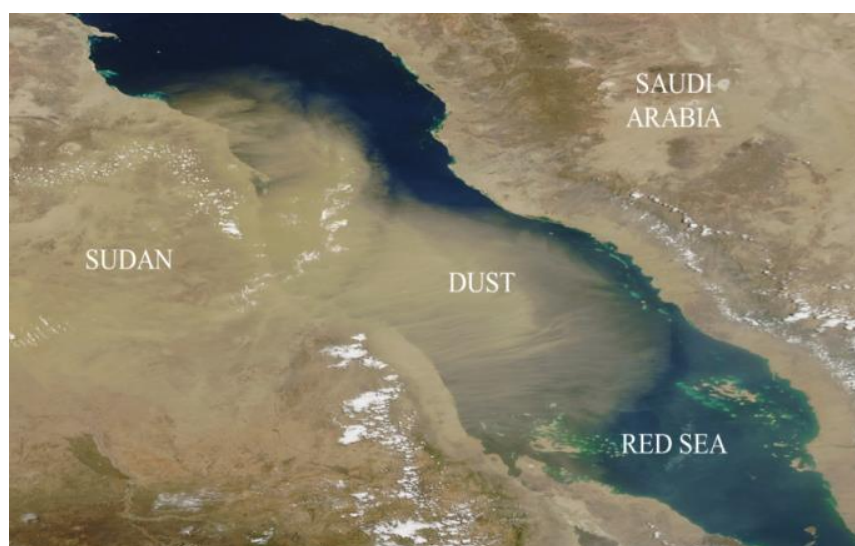


**Figure 11.** *Observatory, N. E., Dust Over The Red Sea.* <http://earthobservatory.nasa.gov>, June 15, 2016. Image of dust storm that occurred above the Red Sea. It illustrates the magnitude of mineral dust emissions initiated by dust storms in the Saharan region.

Mineral particles having diameters of about 2 microns ( $\mu\text{m}$ ) can have lifetimes on the order of weeks in the atmosphere and can travel long distances. Dust storms originating in desert regions of Northern Africa, the Middle East, and Central Asia can account for approximately 90% of the mineral dust aerosols generated annually (Usher et al., 2003). Mineral aerosols can also be generated from anthropogenic sources. Improper agricultural activities (i.e. the dust bowl) can generate up to 20-50% of the mineral dust aerosols produced globally (Usher et al., 2003). The exact chemical compositions of



mineral dust aerosols are source dependent. Mineral aerosols are composed primarily of aluminum and silicon oxides; approximately 60 % of mineral aerosol mass can be attributed to  $\text{SiO}_2$ , sometimes in the form of quartz, and 10-15 % can be attributed to  $\text{Al}_2\text{O}_3$  (Usher et al., 2003). The bulk of  $\text{Al}_2\text{O}_3$  found in mineral particles exists in the form of aluminum silicates, which are major components of mineral dust, such as illite, micas, and kaolinite. The abundance of calcium, iron and magnesium oxides in mineral aerosols vary greatly with source location. The chemical composition of mineral dust aerosols dictates their ability to facilitate cloud formation and participate in heterogeneous atmospheric chemistry.

The presence of reactive mineral particles in the midst of volatile organic compounds in the atmosphere presents an intriguing question: can mineral aerosols promote secondary organic aerosol formation? Romanías et al. used diffuse reflectance infrared Fourier transform spectroscopy (DRIFTS), selected-ion flow-tube mass spectroscopy (SIFT-MS), and long path transmission Fourier transform infrared spectroscopy (FTIR) to study interactions between VOC and dried Saharan dust samples (2016). The VOC used in these studies were toluene ( $\text{C}_7\text{H}_8$ ), which is primarily generated by anthropogenic sources, and limonene ( $\text{C}_{10}\text{H}_{16}$ ), which is part of the monoterpene class of BVOC. For approximately 2 hours, 10 ppm of each VOC at room temperature were mixed with a bulk air flow (total air flow = 250 sccm) and allowed to interact with the Saharan dust surfaces contained in the DRIFTS chamber. For both limonene and toluene, the percentage of VOC recovered after flushing the dust samples with dry air was significantly dependent on the source location of the dust, and slightly dependent on the  $\text{SiO}_2$  content of each sample. Relative to toluene adsorption, which was associated with a

desorption percentage  $\leq 70$  %, limonene adsorption to most of the dust surfaces was considerably more irreversible (desorption  $\leq 5$  %) (Romanías et al., 2016). These findings may indicate that monoterpene volatile organic compounds have stronger interactions than other organic VOC with mineral aerosol surfaces.

In order to investigate heterogeneous reactions between limonene and mineral dust aerosols, prior work in the Hinrichs lab used DRIFTS and gas chromatography-mass spectrometry (GC-MS) (Lederer et al., 2016). At a relative humidity of 30 %, surface concentrations of organic matter on the mineral samples ranged from  $0.8 \times 10^{18} \text{ m}^{-2}$  (for  $\alpha$ -alumina) to  $4.7 \times 10^{18} \text{ m}^{-2}$  (for kaolinite). Limonene diol was determined to be the major product for reactions performed with kaolinite, montmorillonite, Arizona test dust and silica.  $\alpha$ -Alumina and  $\gamma$ -alumina exhibited more diverse product distributions; carveol, terpineol, carvone and limonene oxide were among the organic products identified on these mineral surfaces (Figure 12). The chemical reactivity of limonene and mineral dust samples suggests that monoterpenes do not simply adsorb to mineral surfaces. Rather, mineral surfaces facilitate chemical transformations of VOC to generate distinct chemical compounds. Similar to reactions between VOC and atmospheric oxidants (i.e.  $\text{NO}_3$ , OH,  $\text{O}_3$ ), reactions between limonene and mineral dust yield oxidized lower volatility organic products (Figure 12). For example, the addition of an alcohol group to limonene, which forms carveol causes a factor of  $5.7 \times 10^{-3}$  reduction in vapor pressure (Table 2).

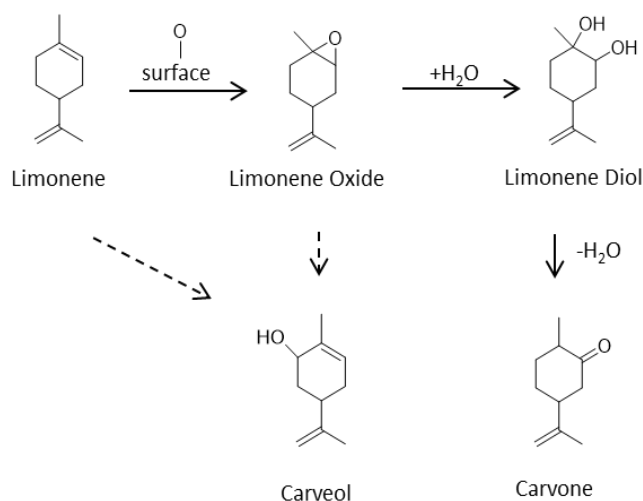


**Figure 12. Products and Mechanisms for Reaction of Limonene with Mineral Samples.** Adapted from Lederer et al. Reactions of limonene and mineral surfaces generate oxidized lower volatility products.

The formation of low volatility products from heterogeneous reactions between  $\alpha$ -pinene and kaolinite has been assessed; however, these studies are seldom performed in the context of atmospheric chemistry. Low volatility organic compounds are the main components of secondary organic aerosols; therefore, aerosolized mineral particles that are coated with chemically aged or low volatility organics can viably contribute to the global SOA budget. Cheshchevoi et al. studied the products of heterogeneous reactions between  $\alpha$ -pinene and kaolinite using gel permeation chromatography, infrared spectroscopy (IR), ultraviolet spectroscopy and proton nuclear magnetic resonance spectroscopy (1989). The goal of Cheshchevoi et al. was to evaluate whether kaolinite could effectively catalyze the formation of high-molecular weight  $\alpha$ -pinene dimers, which are of interest industrially because they are potential biofuels. Therefore, the reactions were performed under dry conditions and with saturated  $\alpha$ -pinene vapor ( $\sim 4.75$  Torr at  $25^\circ\text{C}$ ). The primary organic products of these reactions were  $\alpha$ -pinene dimers that possessed an average molecular weight of 500 amu (Cheshchevoi et al., 1989). Strong bands ranging from  $2853$  to  $2962\text{ cm}^{-1}$  in the IR spectra of the products indicated the

presence of  $\text{-CH}_3$  and  $\text{-CH}_2$  groups while very weak bands at  $1720\text{ cm}^{-1}$  and  $3450\text{ cm}^{-1}$  indicate small concentrations of  $\text{C=O}$  and  $\text{OH}$  groups, respectively. Cheshchevoi et al. propose that the dimers they observed were primarily saturated  $\alpha$ -pinene-derived monomers that contained a few  $\text{C=C}$  and oxygen atoms (Cheshchevoi et al., 1989).

Dimer formation is a major pathway for the production of air-polluting secondary organic aerosols. The high molecular weights of dimers and the presence of oxygen atoms cause them to have very low vapor pressures. Thus, monoterpene-derived dimers irreversibly coat mineral surfaces and result in long-term changes in their chemical nature. Therefore, dimer coated mineral particles are essentially secondary organic aerosols. Dimer coated mineral particles may continue to interact with VOC in the atmosphere which would increase their mass and chemical complexity. In the reactions between limonene and mineral dust samples reported by Lederer et al., limonene-derived dimers were not observed. Yet, limonene-derived dimers via a heterogeneous pathway were observed by Iinuma et al. whose findings are reported in section 1.3. Similar to the findings of Iinuma et al., Li et al. observed limonene derived dimer and trimer formation from solution-phase reactions between limonene and sulfuric acid droplets using gas chromatography-mass spectrometry (GC-MS). Although no structures were reported, Li et al. mentioned that limonene dimer and trimer products were observed primarily at sulfuric acid concentrations of 57.8 weight percent (wt %) and relative humidity levels below 20 % (Li et al., 2010). These findings illustrate the importance of acid-catalysis in dimer formation and suggest that monoterpene dimer formation can occur without significant oxidation. However, the question of whether monoterpene-derived dimer formation, which contributes significantly to SOA, occurs at atmospherically relevant

conditions is critical and has not been thoroughly investigated. This study seeks to answer this question using a heterogeneous reaction model involving kaolinite clay and ( $\alpha$ )-(+)-pinene. The findings of Cheshchevoi et al. suggest that  $\alpha$ -pinene may be a viable precursor VOC for the formation of mineral aerosols that are coated with significantly low volatility organics. However, the reaction conditions used by Cheshchevoi et al., which involved drying the kaolinite clay at 400 K and using saturated  $\alpha$ -pinene vapor at 298 K, are atmospherically irrelevant. This study investigates the heterogeneous reactivity of  $\alpha$ -pinene and kaolinite at atmospherically relevant conditions in order to assess  $\alpha$ -pinene's ability to serve as a precursor for SOA formation.

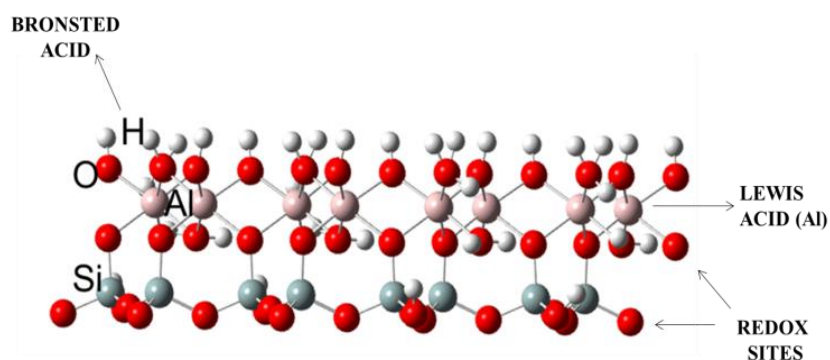


**Figure 13. Chemical Structure of Kaolinite Clay.** Overall chemical formula:  $\text{Al}_2\text{Si}_2\text{O}_5(\text{OH})_4$ . Chemical composition of kaolinite allows the mineral surface to possess various reactive sites.

This study uses kaolinite ( $\text{Al}_2\text{Si}_2\text{O}_5(\text{OH})_4$ ), a major phyllosilicate clay component of mineral dust particles, to model the atmospheric chemical activity of mineral dust aerosols. Kaolinite is composed of two primary repeating sheets (Figure 13): a tetrahedral silica layer ( $\text{SiO}_4$ ) and an octahedral alumina layer ( $\text{AlO}_6$ ). The alumina sheets of kaolinite are lined with hydroxyl groups (OH) that participate in hydrogen bonding interactions with basal oxygens on the silica sheets. The chemical structure of kaolinite

generates a variety of reactive sites on the clay surface (Figure 13). The surface hydroxyl groups on kaolinite can serve as Brønsted-Lowry acids by donating acidic protons in chemical reactions, and surface aluminum atoms can serve as Lewis acids by receiving electrons from electron-rich donors. Surface oxygen atoms can accept electrons from reducing agents and thereby facilitate reduction-oxidation (REDOX) reactions on the kaolinite surface. Therefore, the chemical composition of the kaolinite surface promotes acid-catalyzed reactivity. The reactive potential of the kaolinite surface provides insight into the nature of the chemical activity of mineral aerosols in the atmosphere.

Infrared spectrometry is the main method used in this study to assess the heterogeneous reaction between  $\alpha$ -(+)-pinene and kaolinite. Chapter 2 describes how Fourier transform infrared spectroscopy is used to identify the chemical functionalities in samples of kaolinite exposed to  $\alpha$ -pinene and outlines the experimental methods. Chapter 3 provides a detailed analysis of the reaction performed between  $\alpha$ -pinene and kaolinite at a relative humidity level of 30 % and includes analyses of product formation. Chapter 4 characterizes the effect that water adsorption onto kaolinite has on heterogeneous reactivity with  $\alpha$ -pinene. Chapter 5 evaluates and discusses the atmospheric implications of reactions between ( $\alpha$ )-(+) -pinene and kaolinite.

## 2.0. Modeling Heterogeneous Reactions of ( $\alpha$ )-(+)-Pinene and Kaolinite

### 2.1. Fourier Transform Infrared Spectroscopy

The primary method for studying the heterogeneous reactivity of ( $\alpha$ )-(+)-pinene and kaolinite involves the use of Fourier transform infrared spectroscopy (FTIR). Infrared (IR) spectroscopy is used to identify the chemical functionalities that constitute a given chemical sample or analyte. An IR spectrometer passes polychromatic light (light of varying frequencies) through the analyte and measures the absorption (or transmission) of light at each frequency. IR spectroscopy takes advantage of the fact that the different vibrational motions of chemical groups absorb varying frequencies of IR light. The absorption of specific frequencies of IR light allows transitions from low to high energy states to occur between the quantized vibrational energy levels. When a molecule absorbs IR light, transitions between its vibrational energy levels are coupled with distinct modes of oscillation about the molecule's center-of-mass. Therefore, chemical bonds and groups do not experience molecular vibrations or absorb IR light unless the frequency of light introduced by the IR spectrophotometer is equivalent to the vibrational frequency of a distinct vibrational mode.

$$E_{\text{photon}} = h\nu = E_{\text{vib}}^{n=i} - E_{\text{vib}}^{n=0} \quad \text{Eq. 1}$$

Equation 1 describes the energy associated with transitions between vibrational energy levels where  $n=0$  represents the ground state vibrational energy level and  $n=i$  represents a higher energy vibrational state. The constant  $h$  denotes Planck's constant ( $6.62607 \times 10^{-34}$  J Hz<sup>-1</sup>) and  $\nu$  represents frequency in Hertz (Hz).

The motion of a molecular vibration can be approximated as simple harmonic motion. The frequency of a molecular vibration is described by Equation 2 where  $\nu$  ( $\text{s}^{-1}$ ) denotes the frequency of vibration,  $k$  ( $\text{N m}^{-1}$ ) denotes the force constant and  $\mu$  ( $\text{kg atom}^{-1}$ ) represents the reduced mass of the atoms involved in the vibration (Equation 3).

$$\nu = \frac{1}{2\pi} \sqrt{\frac{k}{\mu}} \quad \text{Eq. 2}$$

$$\mu = \frac{m_1 \cdot m_2}{m_1 + m_2} \quad \text{Eq. 3}$$

When a molecule oscillates, the inter-nuclear distances between atoms continually change as a result of the motion. Using a reduced mass of the chemical bond or group allows us to view it as a single entity and makes characterizing the nature of the vibration more feasible. Information about the absorption of IR light by various chemical groups is processed and translated into a spectrum by the FTIR spectrophotometer instrument. The processed signal is displayed as a spectrum with percent transmittance (Eq. 4) or absorbance on the y-axis and wavenumber on the x-axis.

$$\%T = \frac{I}{I_0} \times 100\% \quad \text{Eq. 4}$$

The frequency of IR light often used by spectrophotometers corresponds to a wavelength range of 2.5 to 15  $\mu\text{m}$ . The unit of wavenumber ( $\text{cm}^{-1}$ ) is the reciprocal of the wavelengths in the IR range measured in centimeters; thus, the wavelengths of IR light used by an IR spectrophotometers vary from approximately 670 to 4000  $\text{cm}^{-1}$ .



Absorbance and transmittance are related by Equation 5 where  $I$  denotes the intensity of light that is transmitted and  $I_o$  denotes the initial intensity of IR light.

$$Abs = -\log\left(\frac{I}{I_o}\right) = -\log(T) \quad \text{Eq. 5}$$

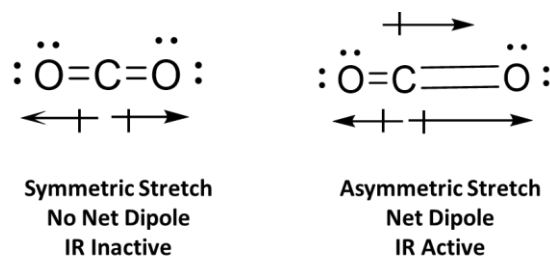
Absorbance for a liquid phase sample is described by Beer-Lambert's Law (Eq. 6) where  $\epsilon$  represents the molar absorptivity ( $\text{M}^{-1} \text{cm}^{-1}$ ),  $c$  signifies the concentration (M) and  $l$  symbolizes the pathlength (cm).

$$Abs = \epsilon \cdot c \cdot l \quad \text{Eq. 6}$$

Equation 7 describes the absorbance of a gas-phase sample where  $\sigma$  represents the absorption cross-section ( $\text{cm}^2 \text{molecule}^{-1}$ ),  $N$  symbolizes the density of the sample ( $\text{molecule cm}^{-3}$ ) and  $l$  represents the pathlength (cm). Absorbance is proportional to concentration; therefore, the unit of absorbance on the y-axis of an IR spectrum indicates the relative concentrations of each chemical group.

$$Abs = \sigma \cdot N \cdot l \quad \text{Eq. 7}$$

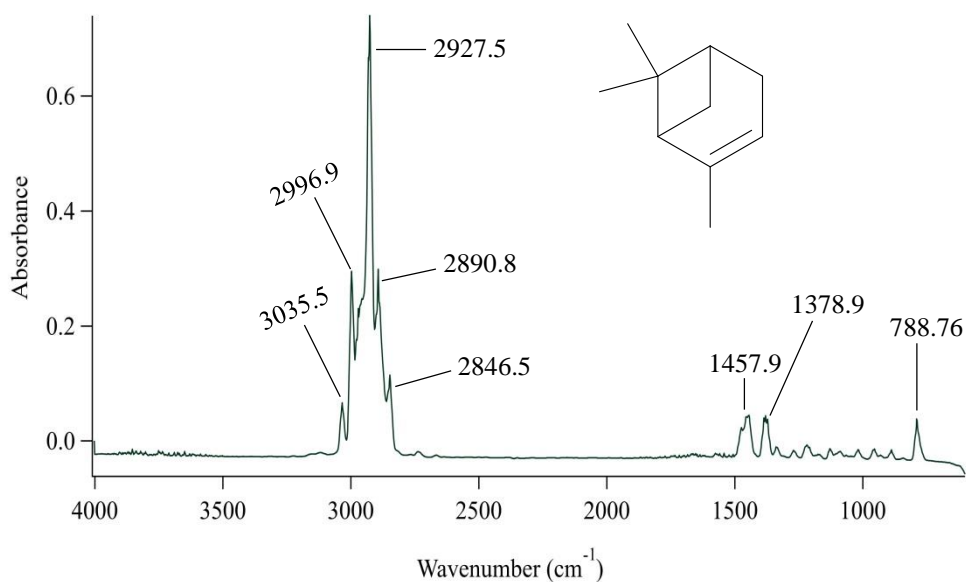
The various principles governing IR absorption make it possible for chemists to use IR spectroscopy to make distinctions between different chemical groups. It is important to note that vibrational modes that do not lead to changes in the dipole moment of bonds or groups are not detected via IR spectroscopy and are considered IR inactive; Figure 14 illustrates an example of an IR active and inactive vibration for  $\text{CO}_2$ . Generally, absorption bands that occur at higher wavenumbers correspond to stretching vibrational modes which involve changes in the lengths of bonds about their center of mass.



**Figure 14. Examples of IR Active and Inactive Vibrational Modes of  $\text{CO}_2$ .** The symmetric stretch of  $\text{CO}_2$  is IR inactive because it does not correspond to a net change in dipole while the asymmetric stretch of  $\text{CO}_2$  is IR active because it corresponds to a net change in dipole. Molecular vibrations must be associated with a net change in dipole in order for them to be detected via IR spectroscopy.

Absorption bands that occur at lower wavenumbers generally evidence bending mode vibrations which result in changes in bond angles. The patterns and wavenumbers of absorbance peaks (or bands) in an IR spectrum correspond to characteristic molecular vibrational modes.

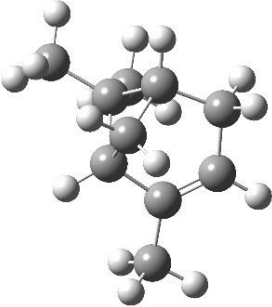
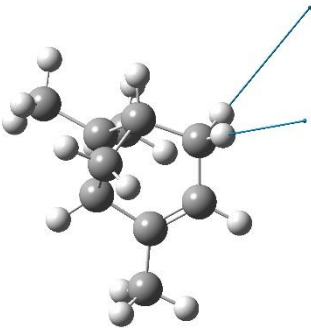
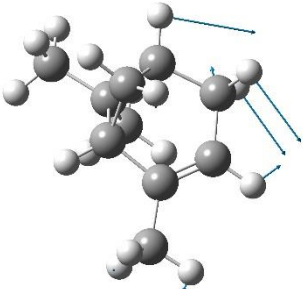
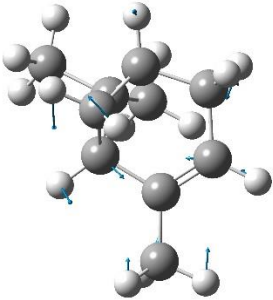
A characteristic IR spectrum of gaseous ( $\alpha$ )-(+)-pinene taken by a 10m-pathlength FTIR gas cell instrument is depicted in Figure 15. The significant medium and strong intensity absorbance peaks that occur between 2800 and 3000  $\text{cm}^{-1}$  are characteristic of the various stretching mode vibrations of  $\text{sp}^3$  hybridized C-H bonds. Significant peaks above the baseline between 788 and 1458  $\text{cm}^{-1}$  have low absorbance intensities and can be attributed to the bending mode vibrations of C-H bonds in ( $\alpha$ )-(+)-pinene. The weak intensity absorbance band at 3035.5  $\text{cm}^{-1}$  is characteristic of the stretching mode vibration of the  $\text{sp}^2$  hybridized C-H bond in ( $\alpha$ )-(+)-pinene.



**Figure 15.** IR spectrum of Gaseous  $\alpha$ -Pinene Taken by FTIR Gas Cell. Medium and strong intensity peaks (2996.9, 2927.5, 2890.8, and 2846.5  $\text{cm}^{-1}$ ) =  $\text{sp}^3$  hybridized C-H stretches. Weak intensity peak (3035.5  $\text{cm}^{-1}$ ) =  $\text{sp}^2$  hybridized C-H stretches. Weak intensity peaks (1457.9, 1378.9, 788.76  $\text{cm}^{-1}$ ) = C-H bends. Patterns associated with absorbance bands in IR spectroscopy allow us to characterize the FTIR spectrum of  $\alpha$ -pinene.

In order to better characterize the FTIR of gaseous  $\alpha$ -pinene, Gaussian 03 and GaussView software were used to calculate the lowest energy electronic structure and the vibrational frequencies of  $\alpha$ -pinene using density functional theory (DFT) (Basis Set: 6-311G(d)). These calculations provided further insight into the nature of the various stretching and bending modes associated with the FTIR spectrum of  $\alpha$ -pinene (Table 3). Table 3 (a) provides a 3-dimensional illustration of the optimized lowest electronic energy structure of  $\alpha$ -pinene generated using density functional theory. In Table 3 (b-d), the vector arrows indicate the movement of the atoms associated with the identified vibrational modes. Our Gaussian frequency calculations suggest that the stretching mode band centered at 2996.9  $\text{cm}^{-1}$  can be attributed to symmetric stretches of the  $\text{CH}_2$  group adjacent to the  $\text{C}=\text{C}$  in  $\alpha$ -pinene; in this mode, the two hydrogen atoms are

simultaneously stretched and compressed about the central carbon upon absorption of IR light.

<b>Table 3: Select Molecular Vibrational Modes of Gaseous <math>\alpha</math>-Pinene Generated Using Density Functional Theory</b>	
<p><b>(a) Computed <math>\alpha</math>-Pinene Structure</b></p> 	<p><b>(b) 2996.8 cm<sup>-1</sup> Symmetric C-H Stretches of CH<sub>2</sub> Group</b></p> 
<p><b>(c) 1374.4 cm<sup>-1</sup> Wagging Bends of C-H in CH<sub>2</sub> and CH Groups</b></p> 	<p><b>(d) 778.6 cm<sup>-1</sup> Bends of C-H in Various Groups</b></p> 

**Table 3. Select Molecular Vibrational Modes of Gaseous  $\alpha$ -Pinene Generated Using Density Functional Theory.** (DFT/6-311G(d)) (a) Lowest electronic energy structure of  $\alpha$ -pinene computed by Gaussian using DFT (b) symmetric C-H stretches of CH<sub>2</sub> group at 2996.8 cm<sup>-1</sup> (c) wagging bends of C-H in CH<sub>2</sub> and CH groups at 1374.4 cm<sup>-1</sup> (d) bends of C-H in various groups at 778.6 cm<sup>-1</sup>. Gaussian computations allow us to more thoroughly characterize the FTIR absorbance bands in the spectrum of gaseous  $\alpha$ -pinene.

According to our computation, the absorbance peak around 1374.4 cm<sup>-1</sup> corresponds to C-H bending mode vibrations of the CH<sub>2</sub> group adjacent to the C=C and of the CH group adjacent to the CH<sub>2</sub> group in  $\alpha$ -pinene. The bending mode of the CH<sub>2</sub> group is referred to as an out-of-plane wagging vibration because the two hydrogens simultaneously translate

out of plane in one direction while the central carbon atom translates out of plane in the opposite direction. The absorbance band around  $778.6\text{ cm}^{-1}$  may be attributed to bending vibrational modes of C-H in various groups. Thus, our Gaussian computations enable us to more thoroughly characterize the FTIR spectrum of  $\alpha$ -pinene. Table 4 summarizes the wavenumbers, intensities and peaks assignments that correspond to the FTIR of gaseous  $\alpha$ -pinene, which is the model VOC used in our study of SOA formation and growth.

<b>Table 4: Summary of Peak Assignments for FTIR spectrum of Gaseous <math>\alpha</math>-Pinene</b>		
<b>Wavenumber (<math>\text{cm}^{-1}</math>)</b>	<b>Intensity</b>	<b>Peak Assignment</b>
3035.5	weak	$\text{sp}^2$ hybridized C-H stretches
2996.9	strong	symmetric $\text{sp}^3$ hybridized C-H stretches of $\text{CH}_2$ groups
2927.5	very strong	$\text{sp}^3$ hybridized C-H stretches
2890.8	strong	$\text{sp}^3$ hybridized C-H stretches
2846.5	medium	$\text{sp}^3$ hybridized C-H stretches
1457.9	weak	C-H bends
1378.9	weak	C-H bends of $\text{CH}_2$ (wagging) and CH groups
788.76	weak	various C-H bends

**Table 4. Summary of Peak Assignments for FTIR spectrum of Gaseous  $\alpha$ -Pinene.** Using the general patterns of IR absorbance bands and Gaussian computations, the absorbance bands in the FTIR of  $\alpha$ -pinene can be assigned to various molecular vibrational modes.

In order to use IR to study surface chemistry, we use diffuse reflectance infrared Fourier transform spectroscopy (DRIFTS). DRIFTS is a method of FTIR that allows us to identify chemical functionalities present in powdered solid samples. The diffuse reflectance segment of a DRIFTS system (Harrick Scientific) is often added as an

accessory to a standard FTIR instrument. DRIFTS analyzes the surface of the clay sample using the same IR absorption principles that govern traditional FTIR analyses. Thus, DRIFTS can be used to make distinctions between the chemical functionalities present on the surface of a clay sample.

In order to fully understand how DRIFTS analyses are performed, it is important to clearly define what constitutes clay surface area in the DRIFTS system. Fine solid particle samples are packed tightly into the chamber of the DRIFTS accessory; thus, the clay sample that is analyzed possesses a thickness of approximately 1 centimeter (Figure 16).

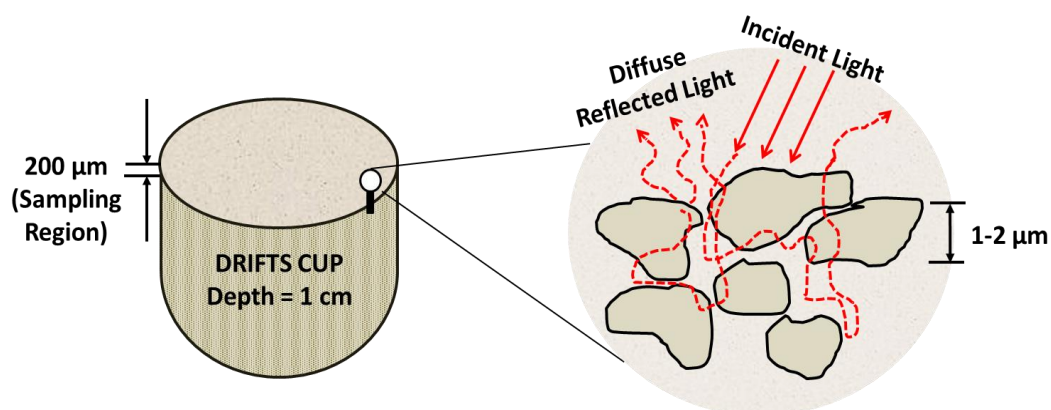


**Figure 16. Clay Packing and Clay Surface Analyses in the DRIFTS System.** Clay packed into the DRIFTS chamber has thickness/depth of ~ 1 cm. Incident light = solid lines and diffuse reflected light = dashed lines. DRIFTS absorption or transmission signals account for diffuse reflectance on the non-geometric surface area.

As a result, the sample has a geometric surface area (equal to  $2\pi r$  of the cup radius) which corresponds to the top-most layer and a non-geometric surface area that includes the surfaces of particles below the top-most layer. Incident IR radiation undergoes diffuse reflectance which means that the photons are scattered by particles within the packed clay sample as shown in Figure 16. Thus, the IR samples not just the geometric surface area

but also the top 0.2 mm of the non-geometric surface area; it is reasonable to assume that the surface areas of particles at the very bottom of the DRIFTS chamber experience less IR light and do not contribute significantly to diffuse reflectance signals. Frequencies of light that are heavily absorbed after interactions with the non-geometric surface are weakly transmitted. Thus, the intensity of diffuse transmission signals is significantly less than the intensity of transmission signals resulting from specular reflection. In order to minimize specular reflection and increase the accuracy of a diffuse reflectance FTIR spectrum, the size of the particles used to pack the DRIFTS chamber must be adequately small.

Fine kaolinite clay is packed into the DRIFTS chamber in order to assess the chemical functionalities present on the clay surface. Figure 17 depicts the DRIFTS spectrum of kaolinite clay, which is used in this study as a model for mineral dust aerosols, and Table 5 summarizes the peak assignments made by Bougeard et al. using computational and experimental studies for the IR of kaolinite (2000). Similar to the characterization of absorbance peaks in the FTIR spectrum of  $\alpha$ -pinene, absorbance bands in the DRIFTS spectrum of kaolinite correspond to unique molecular vibrational modes of the various chemical groups associated with the structure of kaolinite. The strong absorbance bands ranging from  $3400 - 3700 \text{ cm}^{-1}$  correspond to various stretching modes involving hydroxyl (OH) groups. Significant absorbance peaks between  $700 - 1500 \text{ cm}^{-1}$  correspond to the lattice vibrations of silicon and aluminum oxides.

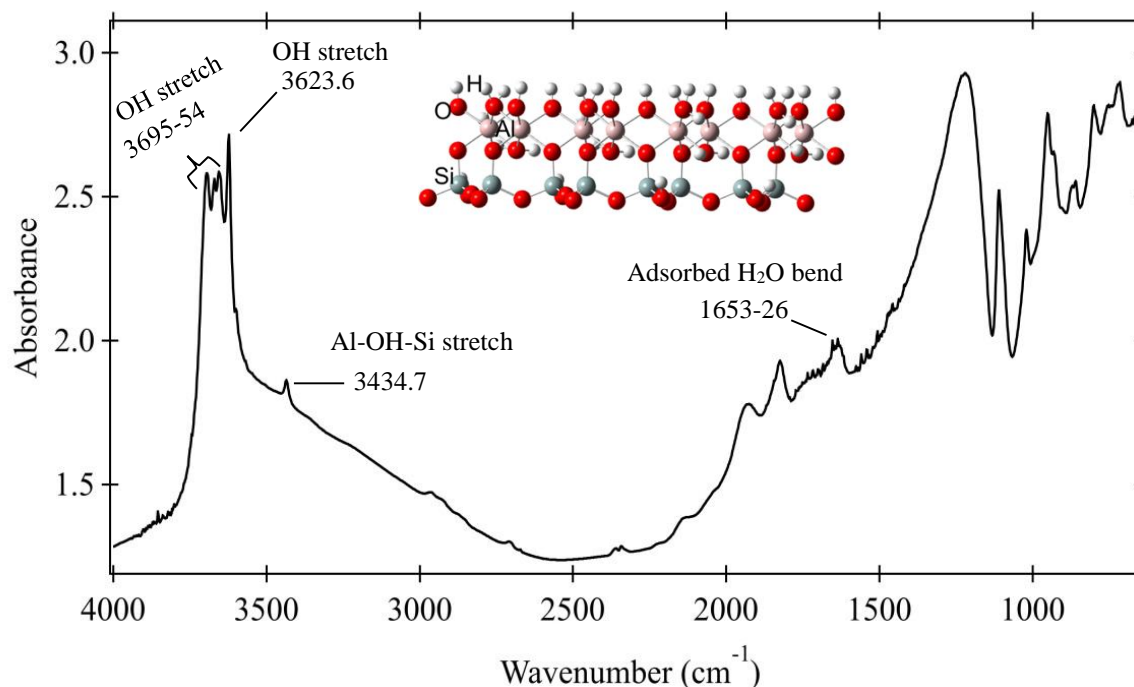


**Figure 17. DRIFTS Spectrum of Kaolinite Clay.** Absorbance bands around 3400 – 3700 cm<sup>-1</sup> correspond to various stretching modes involving hydroxyl (OH) groups. Peaks between 700 – 1500 cm<sup>-1</sup> correspond to lattice vibrations of Si and Al oxides. Bands around 1653-26 cm<sup>-1</sup> indicate H-O-H bending of adsorbed water. DRIFTS characterizes the chemical structure of kaolinite clay and adsorbed molecules.

<b>Wavenumber (cm<sup>-1</sup>)</b>	<b>Peak Assignment</b>
3695-54	O-H stretching of surface hydroxyls
3623.6	O-H stretching of surface hydroxyls
3434.7	O-H stretching of surface hydroxyl attached to Al and Si atoms
1653-26	H-O-H bending of surface adsorbed water
1500-700	Lattice vibrations of Si and Al oxides

**Table 5. Peak Assignments for Kaolinite DRIFTS spectrum.** Adapted from Bougeard et al., 2000. Summary of the peak assignments made in the DRIFTS spectrum of kaolinite clay (Figure 17). Bands at 3434.7 cm<sup>-1</sup> and 1653-26 cm<sup>-1</sup> indicate stretching and bending modes, respectively, of surface adsorbed water. Thus, DRIFTS allows us to also characterize molecules that are associated with (or adsorbed to) the clay surface.



The aforementioned absorbance bands in the DRIFTS spectrum of kaolinite are characteristic of the clay's unique molecular structure. In addition to providing insight about the chemical functionalities that constitute the structure of kaolinite, DRIFTS also identifies chemical functionalities on the clay surface that are associated with the kaolinite surface but not necessarily part of the clay's chemical structure. For example, absorbance bands occurring around  $1653\text{-}26\text{ cm}^{-1}$  indicate the bending modes of surface adsorbed water molecules on the kaolinite surface. Thus, DRIFTS is an effective technique for characterizing both the chemical nature of kaolinite and the molecules adsorbed on its surface. In Chapter 3, as we discuss the reactions performed between kaolinite and ( $\alpha$ )-(+)-pinene using DRIFTS, we will observe changes in the absorbance bands corresponding to surface adsorbed molecules, such as water and organic compounds, as a result of heterogeneous reactivity. Hence in this study, DRIFTS enables us to answer the question of whether heterogeneous reactivity involving  $\alpha$ -pinene and mineral aerosols can lead to SOA formation and growth in the atmosphere.

## 2.2. Experimental Methods

In our study, a diffuse reflectance infrared Fourier transform spectrometer (DRIFTS) system was created by accessorizing a Nicolet 6700 Fourier transform infrared spectrometer (FTIR) with a DRIFTS chamber (Harrick Scientific). A 937A MKS Mass-Flow Controller adjusted and monitored the flow rates of dry air and humidified air, which was created by bubbling water into the air flow. The dry and wet air flows were adjusted using MKS Mass-Flo® and gauge controllers which allowed a variety of relative humidity levels to be attained. Nitrogen gas was bubbled through a sample of liquid ( $\alpha$ )-(+)-pinene (CAS: 7785-70-8) that was submerged in a cooling bath used to reduce the

vapor pressure of ( $\alpha$ )-(+)-pinene and consisted of NaCl and ice between -4 and -12 °C. A Matheson® flow meter maintained the flow of gaseous ( $\alpha$ )-(+)-pinene (7 ppm) in the system at 6.5 standard cubic centimeters per minute (sccm).

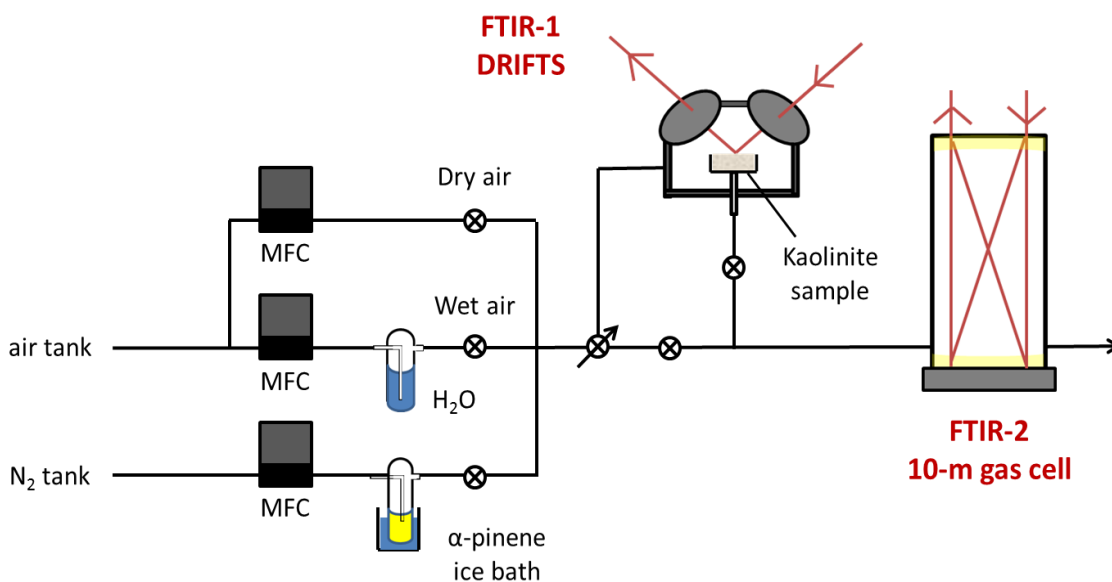


**Figure 18. Schematic of Experimental Set-up.** A series of Mass Flo® controllers and switches allow a humid air mixture containing gaseous  $\alpha$ -(+)-pinene to be created. The air mixture is exposed to kaolinite in the DRIFTS chamber where heterogeneous reactivity takes place. DRIFTS monitors the formation of organic products on the kaolinite surface. The air mixture that exits the DRIFTS chamber is monitored by a 10-m FTIR gas cell in order to assess the  $\alpha$ -pinene concentration.

The total air flow of the pinene gas, dry air and humid air mixture was maintained at 300 sccm. The air mixture was flowed through a sample of kaolinite clay (The Clay Minerals Society) packed onto a metallic frit embedded in the DRIFTS chamber. After the air mixture exited the DRIFTS chamber, a Nicolet 6700 10m-pathlength FTIR gas cell was used to measure the concentration of gaseous ( $\alpha$ )-(+)-pinene by comparison to a calibration curve (Sharpe et al., 2004). Reactions were performed for approximately 16 to 18 hours. DRIFTS collected spectra of the kaolinite surface every 4 minutes and the

FTIR gas cell collected spectra of gaseous ( $\alpha$ )-(+)-pinene every 2 minutes. OMNIC™ series software was used to monitor changes in the C-H stretching region around 2900  $\text{cm}^{-1}$  for the data collected by both FTIRs. Integrations of the areas under the peaks in this region and spectral subtractions were performed using Igor Pro software. After each reaction, the top layer of the kaolinite clay (~ 0.007 g) was extracted, sonicated in acetonitrile for 10 minutes, filtered and analyzed using an Agilent Technologies 5975C inert MSD-7890A gas chromatography-mass spectrometry (GC-MS) instrument.

Gas chromatography and mass spectrometry are distinct analytical techniques that make it possible to characterize chemical compounds. Gas chromatography separates the chemical compounds present in a mixture according to their relative polarities, while mass spectrometry ionizes and fragments chemical compounds in order to generate unique fragmentation patterns. A GC instrument uses heat to vaporize chemical compounds dissolved in a solvent and passes them through a non-polar column (HP-5, 30 m  $\times$  0.32 mm  $\times$  0.25  $\mu\text{m}$  (19091J-413)) referred to as the stationary phase. While inert helium gas (mobile phase) carries the gaseous chemical compounds through the heated column, compounds that are relatively non-polar interact more significantly with the silica column. Thus, smaller molecular weight compounds containing electronegative atoms, such as oxygen atoms, have smaller retention times in the column and are eluted prior to relatively larger molecular weight compounds that contain primarily carbon and hydrogen atoms. GC is therefore an effective tool for separating organic compounds in a mixture. In a GC-MS instrument, separated organics are transferred into a mass spectrometer which bombards the compounds with highly energetic electrons causing them to lose an electron and fragment as a result of electron repulsion. The mass of the

fragments and their charges are analyzed by the MS instrument which determines the mass-to-charge ratios ( $m/z$ ) and relative abundances of each fragment. A given chemical compound has a unique pattern of fragmentation; thus, comparisons between the MS spectra of unknown compounds and a mass spectral library of known compounds makes it possible for chemists to identify chemical products. The combination of GC and MS techniques provided by a GC-MS instrument allows us to separate and identify the organic products generated as a result of reactions between ( $\alpha$ )-(+)-pinene and kaolinite. Analyses of the structures of the organics produced from reactions between  $\alpha$ -pinene and mineral dust will allow us to determine whether this heterogeneous pathway can lead to SOA.

### **3.0. Reaction of $\alpha$ -(+)-Pinene and Kaolinite at a Relative Humidity Level of 30%**

This section outlines the experimental and analytical details of the reaction performed between  $\alpha$ -(+)-pinene and kaolinite at a relative humidity level of 30%.

#### **3.1. Experimental Details**

To attain the necessary conditions for this reaction, dry and humidified air having flow rates of 194 sccm and 100 sccm, respectively, were mixed to attain a relative humidity level of 30 %. Humidified air was flowed through the DRIFTS chamber and a background IR spectrum of the kaolinite clay surface was collected after equilibration. Liquid  $\alpha$ -(+)-pinene was cooled to -11.2 °C and bubbled into the gas phase in order to achieve a gaseous  $\alpha$ -(+)-pinene concentration of 7 ppm, which was measured using the 10m-pathlength FTIR gas cell.

#### **3.2. DRIFTS Analysis**

Figure 19 displays overlaid DRIFTS spectra collected 25, 50, 100, 200, and 400 minutes after the reaction between  $\alpha$ -(+)-pinene and kaolinite began. By overlaying IR spectra from different time points in the reaction, peaks that do not align with one another and vary with time reflect the appearance or disappearance of chemical functionalities due to the reaction. In Figure 19, the characteristic peaks of kaolinite, which remain constant throughout the reaction (i.e. O-H stretching bands between 3400-3700  $\text{cm}^{-1}$  and O-H bending from 952 to 931  $\text{cm}^{-1}$ ) are evident.

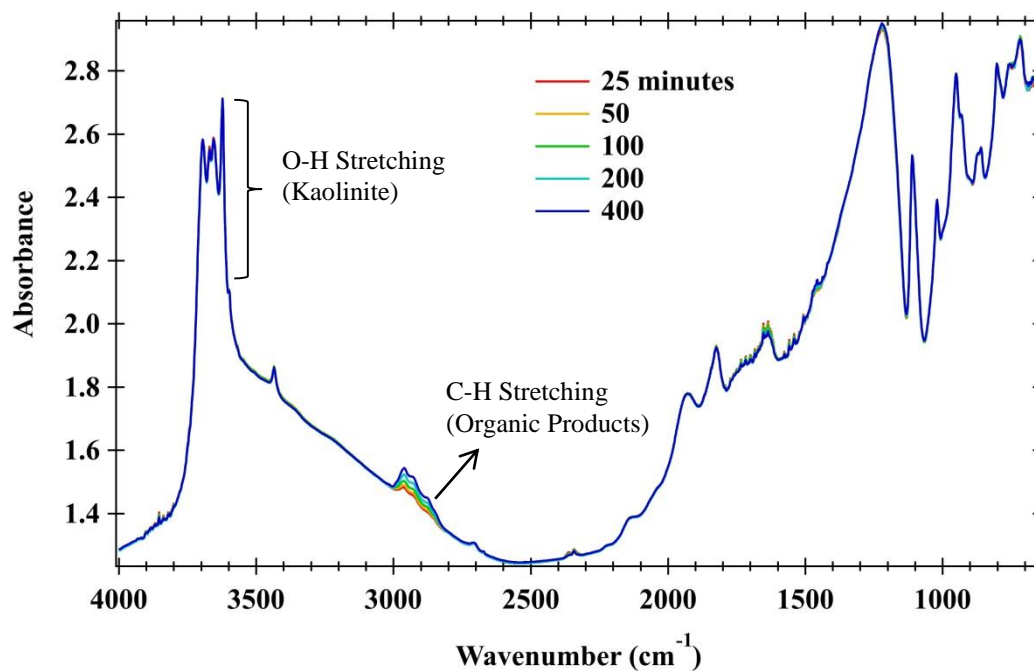


**Figure 19. Overlaid IR Spectra of Kaolinite Surface for Reaction at RH = 30 % for Various Time Points.** Color gradient of peaks in C-H stretching region ( $\sim 2900\text{ cm}^{-1}$ ) reveals that the concentration of organic product adsorbed to the kaolinite surface changes throughout the reaction.

A close look at the region around  $2900\text{ cm}^{-1}$  reveals peaks which, unlike the kaolinite characteristic peaks, appear to increase with time. These peaks characterize the stretching mode frequencies of carbon-hydrogen bonds and remain even when the  $\alpha$ -pinene flow is stopped. Therefore, they indicate the formation of irreversibly adsorbed organic products.

In order to better visualize the spectral changes associated with the adsorbance of organics to the kaolinite surface over time, a spectrum of unreacted kaolinite was subtracted from spectra collected throughout the reaction. The subtraction spectra are depicted in Figure 20; after 25 min of reaction, small peaks corresponding to the C-H stretching modes ( $2900\text{ cm}^{-1}$ ) are visible and they increase in size as the reaction

progresses. The increase in size of the C-H stretching bands over time indicates that more organic product forms and adsorbs to the surface as the reaction progresses.

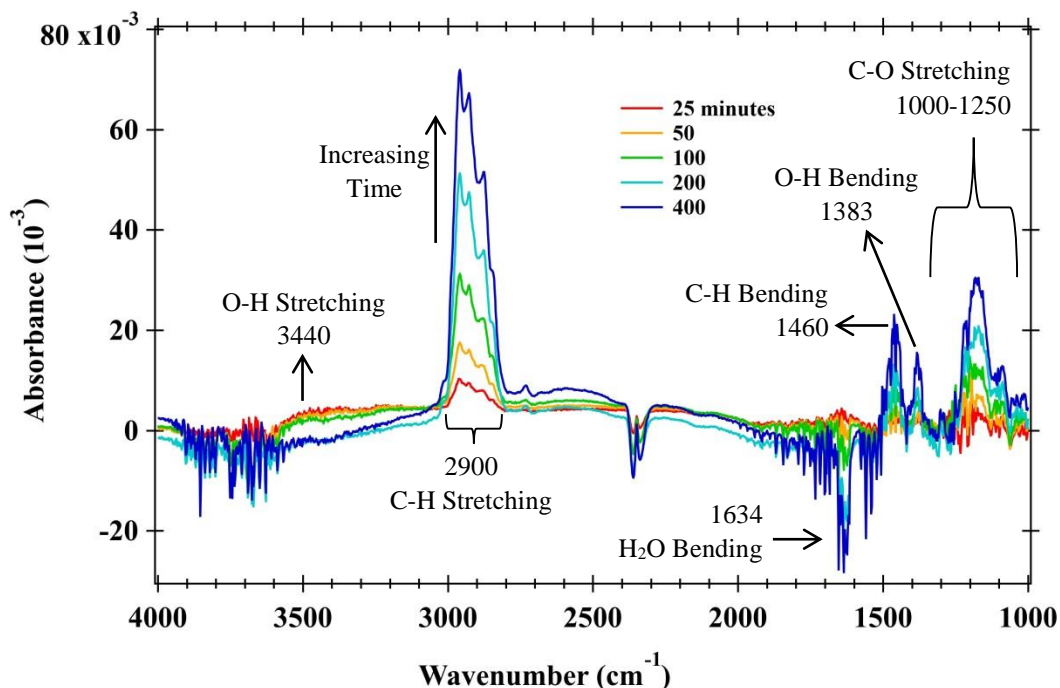


**Figure 20. Subtracted IR Spectra of Kaolinite Surface for Reaction at  $RH = 30\%$  for Various Time Points.** Note: loss in absorbance at  $2350\text{ cm}^{-1}$  corresponds to loss of  $\text{CO}_{2(g)}$  over time. Heights of C-H ( $2900\text{ cm}^{-1}$ ) peaks increase and heights of  $\text{H}_2\text{O}$  bends ( $1634\text{ cm}^{-1}$ ) decrease over time. Demonstrates increasing concentration of organic product adsorbed to kaolinite surface over time and loss of  $\text{H}_2\text{O}$  as reaction progresses.

The increasing adsorbance of organic products to the clay surface over time is also evidenced by increases in C-O stretching bands ( $1000\text{--}1250\text{ cm}^{-1}$ ) and C-H bending vibrations ( $1460\text{ cm}^{-1}$ ). Increases in the C-O stretching bands ( $1000\text{--}1250\text{ cm}^{-1}$ ) and O-H bending vibrations ( $1383\text{ cm}^{-1}$ ) suggest that the organic products contain alcohol (OH) groups; this finding will be confirmed later by GC-MS analyses. As the reaction proceeds, we also observe a decrease in the size of peaks corresponding to the  $\text{H}_2\text{O}$  bending mode of surface adsorbed water molecules ( $1634\text{ cm}^{-1}$ ) which suggests that the mechanism for product formation involves water consumption (see Section 3.3). The

changes in the broad OH stretching mode bands centered around  $3440\text{ cm}^{-1}$  are random and slight; thus, they likely correspond to the OH stretching modes of both surface adsorbed  $\text{H}_2\text{O}$  molecules and alcohol groups on the reaction products. Thus, the combined effect of losing surface adsorbed  $\text{H}_2\text{O}$  and forming hydrated organic products can explain why changes in the OH stretching bands appear to be generally insignificant.

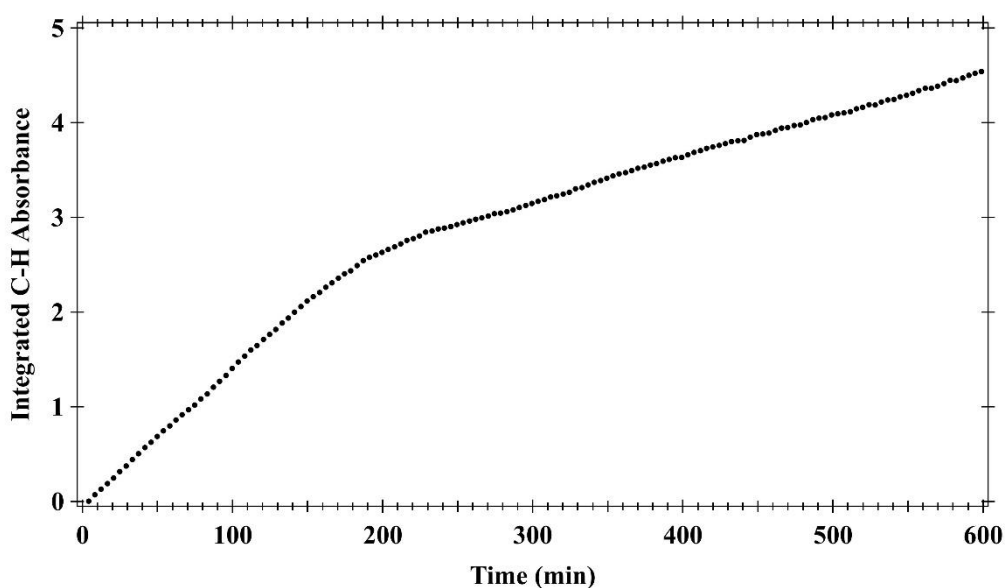


**Figure 21.** *Integrated Absorbance of C-H Stretching Bands vs. Time for Reaction at RH = 30 % for Various Time Points.* Displays that the rate of product formation generally increases over time.

For every DRIFTS spectrum taken of the kaolinite surface, the area under the C-H stretching mode peaks were integrated and plotted against time in order to gain insight into the kinetics of the reaction (Figure 21). This plot illustrates that the rate at which organic product forms on the kaolinite surface generally increases over time. Around 200 min of reactivity, there appears to be a sudden reduction in the rate of organic product formation. This rate reduction is likely due to a sudden change in the  $\alpha$ -pinene



concentration as a result of a fluctuation in the cooling bath's temperature and does not characterize the reactions monitored at other relative humidity levels.

In order to more accurately characterize the rate of organic product formation as a result of reactions between ( $\alpha$ )-(+)-pinene and kaolinite, we will instead consider the plot of integrated C-H absorbance versus time at a relative humidity level of 10 % (Figure 22).

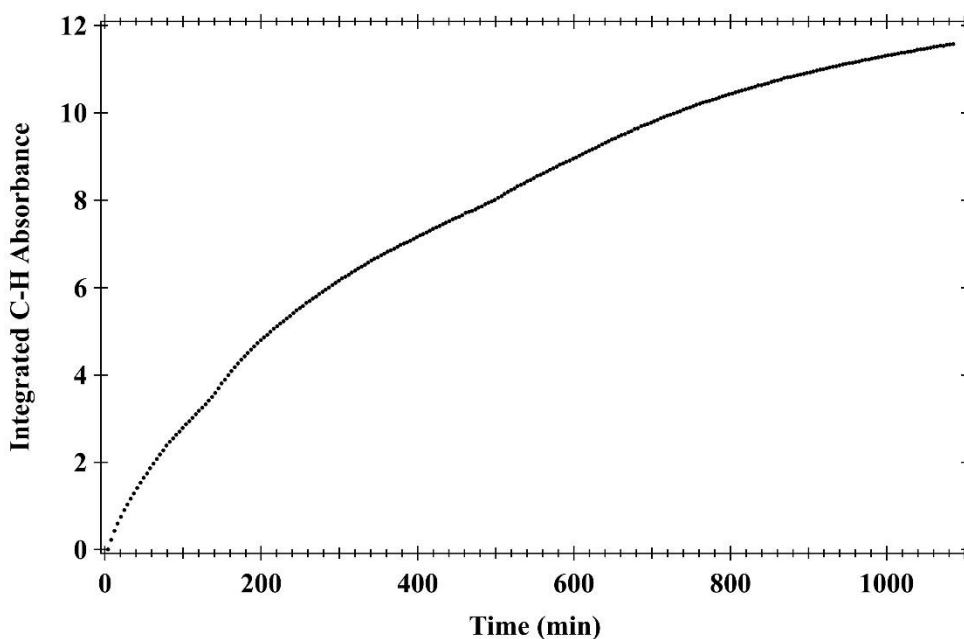
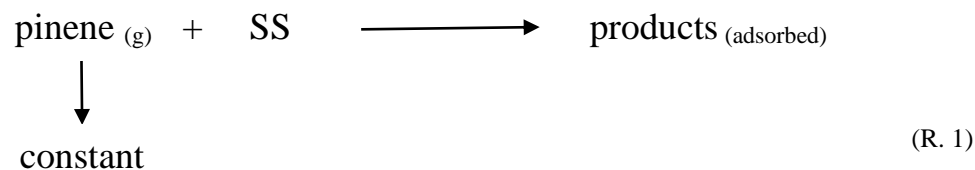


**Figure 22. Integrated Absorbance of C-H Stretching Bands vs. Time for Reaction at RH = 10 % for Various Time Points.** Illustrates that organic product formation generally increases over time. The initial rate of reaction exceeds the latter rate of reaction which may indicate that there are two distinct processes present which control product formation.

In Figure 22, the plot of integrated C-H absorbance versus time is outlined by the black dotted line; this plot demonstrates that the rate  $k$  of organic product formation decreases over time. We can derive an exponential equation that models the concentration of organic product as a function of time by considering the general chemical equation for the reaction of ( $\alpha$ )-(+)-pinene and kaolinite (R.1).



Organic product formation as described by Reaction 1 is a second order process that is dependent on both the concentration of ( $\alpha$ )-(+)-pinene and the availability of surface sites (SS). Therefore, the overall rate of reaction (Eq. 8) is proportional to a rate constant ( $k$ ), the pinene concentration ( $[Pin]$ ) and the surface site concentration ( $[SS]$ ).

$$Rate = k[Pin][SS] \tag{Eq. 8}$$

However, in the reactions performed between ( $\alpha$ )-(+)-pinene and kaolinite in this study, the concentration of ( $\alpha$ )-(+)-pinene is kept constant at 7 ppm because the air mixture flows continuously through the reaction chamber and replenishes any  $\alpha$ -pinene content that is used up for product formation. Therefore, we can re-model the rate of reaction as a pseudo-first order process (Eq. 9) where the rate of reactivity is proportional to  $[SS]$  and a new rate constant  $k_{exp}$  ( $\text{min}^{-1}$ ), which is equivalent to the product of  $k$  and  $[Pin]$ .

$$Rate = k_{exp}[SS] = -\frac{d[SS]}{dt} = \frac{d[P]}{dt} \tag{Eq. 9}$$

Since the surface site concentration decreases over time, we can consider that the rate of product formation is equivalent to the rate of change of the surface site concentration multiplied by a factor of negative 1 (Eq. 9). Separating the terms of the differential equation (Eq. 10) allows us to solve for the surface site concentration at any given point in time throughout the reaction (Eq. 11).

$$\frac{1}{[SS]} d[SS] = -k_{\text{exp}} dt \quad (\text{Eq. 10})$$

$$[SS]_t = [SS]_0 e^{-k_{\text{exp}} t} \quad (\text{Eq. 11})$$

Assuming that the stoichiometric ratios of reactants to products (R. 1) are 1:1 and that no side reactions are responsible for organic product formation, we can consider that the sum of the product  $[P]_t$  and surface site  $[SS]_t$  concentrations at any given time during a reaction are equivalent to the initial surface site concentration  $[SS]_0$ . Hence, we can model the concentration of product at any time ( $t$ ) using Equation 12. Substituting the  $[SS]_t$  term in Equation 12 with Equation 11, allows us to generate a model for the organic product concentration as a function of time (Eq. 13).

$$[P]_t = [SS]_0 - [SS]_t \quad (\text{Eq. 12})$$

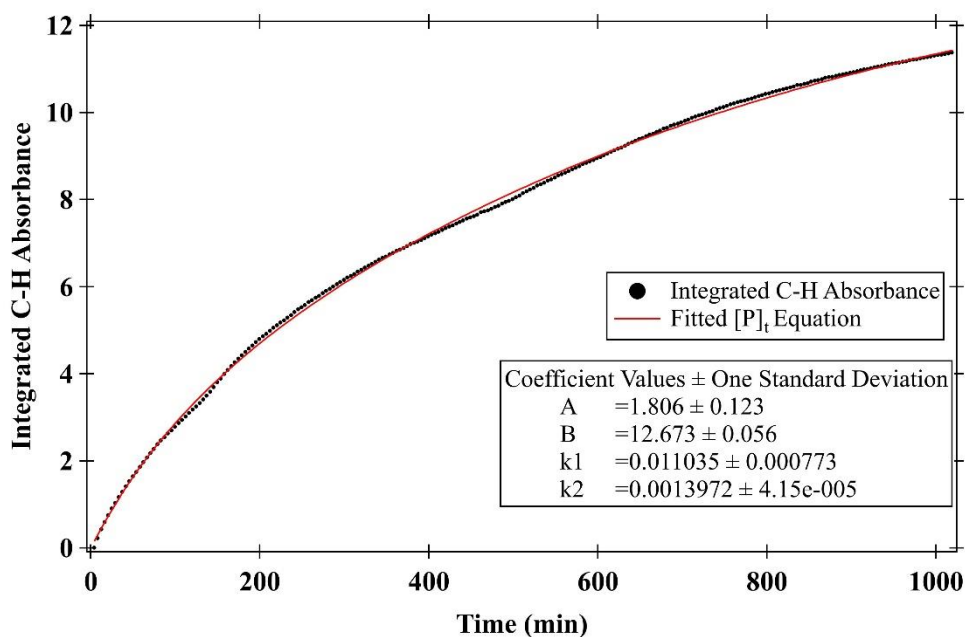
$$[P]_t = [SS]_0 (1 - e^{-k_{\text{exp}} t}) \quad (\text{Eq. 13})$$

Figure 22 indicates that the rate of organic product formation is initially relatively high and that as time progresses, the rate of product formation decreases. This implies that there are two distinct processes that lead to product formation. Therefore, we can model the relationship between organic product concentration and reaction time using two rate constants  $k_1$  and  $k_2$ , which have units of  $\text{min}^{-1}$ .

$$[P]_t = [SS]_0 (1 - e^{-k_1 t}) = A_0 (1 - e^{-k_1 t}) + B_0 (1 - e^{-k_2 t}) \quad (\text{Eq. 14})$$

In Equation 14,  $[P]_t$  represents the concentration of organic product adsorbed to kaolinite at a given time ( $t$ ) and  $[SS]_0$  denotes the initial surface site concentration;  $A_0$  and  $B_0$  (which have units of concentration) are constants that correlate to surface site availability.

Due to the fact that absorbance is proportional to concentration, we can fit our plot of integrated C-H absorbance (which represents the relative concentration of organic product) versus time using Equation 14.



**Figure 23.** Plot of Integrated C-H Absorbance vs. Time for RH = 10 % and Fitted Exponential Growth Model. Fitting  $[P]_t$  (Equation 14) to the plot of integrated absorbance vs. time yields a good fit. Hence, we propose that the rate of organic product formation can be modeled using two rate constants that evidence two distinct processes that control product formation.

Using a single exponential to fit our plot of integrated C-H absorbance yielded a poor fit; however, fitting our plot using two exponentials (as depicted in Figure 23) yields a good fit; this verifies our hypothesis that organic product formation may be controlled by two distinct modes of reactivity. Figure 23 illustrates that the following respective values for  $A_0$ ,  $B_0$ ,  $k_1$ , and  $k_2$  best fit our plot of integrated C-H absorbance vs. time:  $1.806 \pm 0.123$ ,  $12.673 \pm 0.056$ ,  $0.011035 \pm 0.000773$ , and  $0.0013972 \pm .0000415$ ; the values of  $k_1$  and  $k_2$  have units of  $\text{min}^{-1}$  while  $A_0$  and  $B_0$  have units of integrated absorbance. Our fit results demonstrate that the higher rate constant ( $k_1$ ) corresponds to the lesser initial

concentration term ( $A_0$ ) while the lower rate constant ( $k_2$ ) corresponds to the higher initial concentration term ( $B_0$ ). These relationships suggest the presence of a highly reactive surface site that is relatively less abundant on the kaolinite surface and a more abundant surface site that is less reactive with  $\alpha$ -pinene. These findings appear to be consistent with the structure of kaolinite (Figure 13).

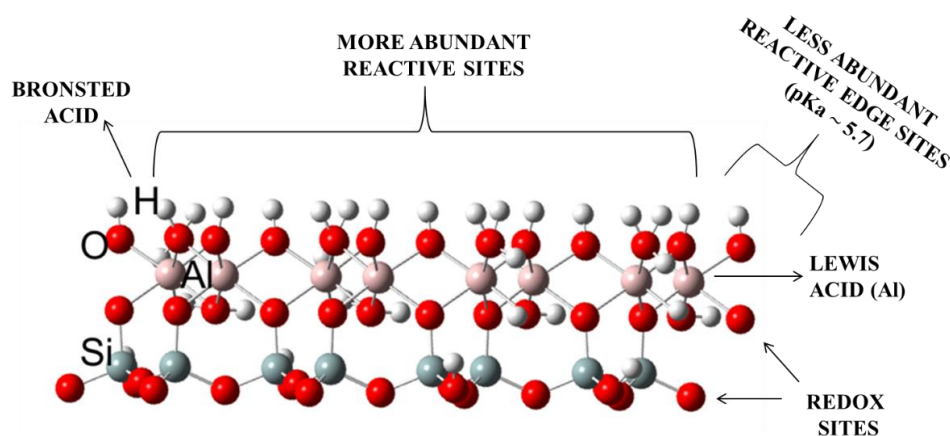


**Figure 13. Chemical Structure of Kaolinite Clay.** Overall chemical formula:  $\text{Al}_2\text{Si}_2\text{O}_5(\text{OH})_4$ . Chemical composition of kaolinite allows the mineral surface to possess various reactive sites. Note: edge sites of Si oxide, which have  $\text{pK}_a = 6.9$ , are not depicted by this image. Structure reveals more abundant less reactive sites on face of kaolinite, and less abundant more reactive sites on the edges of the kaolinite surface.

When we consider the reactive sites on kaolinite, we observe that sites located on the face of the clay are more abundant than those located on the edges. Computational studies using density functional theory (DFT) and first principles molecular dynamics (FPMD) performed by Liu et al. reveal that the reactive edge sites associated with silicon and aluminum oxides on kaolinite have respective  $\text{pK}_a$  values of approximately 6.9 and 5.7, which are fairly acidic (2013). Hence, the edge sites, which are less abundant, may correspond to the more reactive site predicted by our kinetic analyses while the more abundant acidic sites on the face of the kaolinite surface may correspond to the relatively

less reactive sites. If we consider that these are the two processes being described by our kinetic findings in Figure 23, then we are of course insinuating that heterogeneous product formation is somehow dependent on acidity. Using GC-MS analyses, we will later verify the role that acidity plays in the formation of organic products as a result of heterogeneous reactivity. Yet so far, our ability to model the rate of product formation using two exponential terms appears to be consistent with our observations of the chemical structure of kaolinite and indicates that there are two types of reactive sites on the kaolinite surface. Overall, the manner in which the concentration of organic product increases over time suggests that after a given period of time, the surface of kaolinite will become fully saturated and the change in organic product concentration will plateau.

The mechanism of product formation as a result of reactions between kaolinite and  $\alpha$ -pinene may follow the Eley-Rideal heterogeneous mechanism model. This mechanistic model, which is observed for reactions between limonene and mineral dust, suggests that heterogeneous reactivity is not initiated by the adsorption of a VOC to the mineral surface (Lederer et al., 2016). Rather, reactions are initiated following the collision of the VOC with a reactive site on the mineral surface (Lederer et al., 2016). According to this model, organic products form when  $\alpha$ -pinene successfully collides with an acidic site on the clay surface and with surface adsorbed water; therefore, when  $\alpha$ -pinene does not collide successfully with a reactive site, it does not become associated with the clay surface. Figure 24 illustrates the proposed Eley-Rideal reactive model for reactions between  $\alpha$ -pinene and kaolinite.

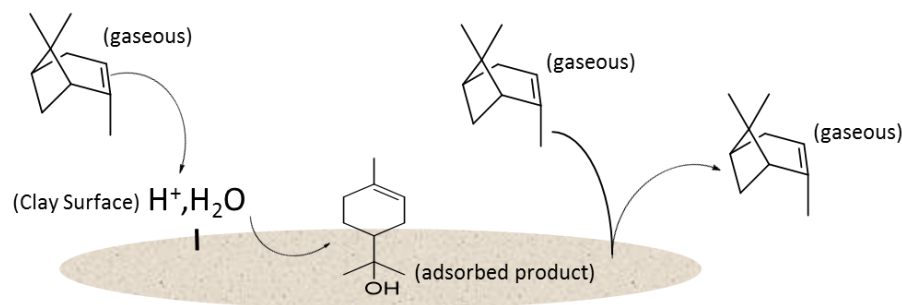


**Figure 24. Scheme of the Eley-Rideal Mechanistic Model for Reactions between Kaolinite and  $\alpha$ -Pinene.** Illustrates that adsorption of organics to the kaolinite surface occurs only after  $\alpha$ -pinene collides and reacts with  $H^+$  and  $H_2O$  supplied by the kaolinite surface.

Our assumption that heterogeneous reactions between  $\alpha$ -pinene and kaolinite follow an Eley-Rideal model is simply based on the fact that this reactive model has been observed for limonene, which is another prevalent VOC that contributes to SOA. Hence, additional studies are needed in order to conclusively determine the heterogeneous mechanistic model for reactions between  $\alpha$ -pinene and kaolinite. In Section 3.3, GC-MS analyses allow us to characterize the nature of the organics produced as a result of reactions between ( $\alpha$ )-(+)-pinene and kaolinite.

### 3.3. Product Analysis Using Gas Chromatography-Mass Spectrometry

Characterization of the reaction products at a relative humidity level of 30% using gas chromatography-mass spectrometry (GC-MS) generated the following total ion chromatogram (TIC) (Figure 25). We confirmed using calibration curves that the peak areas of the monomer products are proportional to the number of pinene molecules that reacted and therefore proportional to their relative concentrations; calibrations were not performed for the dimer products. Hence, the ratio of each peak area to the total peak area

is a good estimate of the yield of the monomer products and provides an approximate yield for the dimer products. The peak with the largest abundance (% yield = 53.68) among the products detected is  $\alpha$ -terpineol, which is therefore identified as the major product. The TIC reveals the presence of high molecular weight dimers (% yield = 16.83) that are significantly fragmented by mass spectra analyses with retention times between 57 and 62 minutes. We consider organic dimers as the second major organic products, and analyze their mass spectra in Section 3.4. The third major reaction product is endo borneol (% yield = 14.27) followed by fenchol (% yield = 7.14).

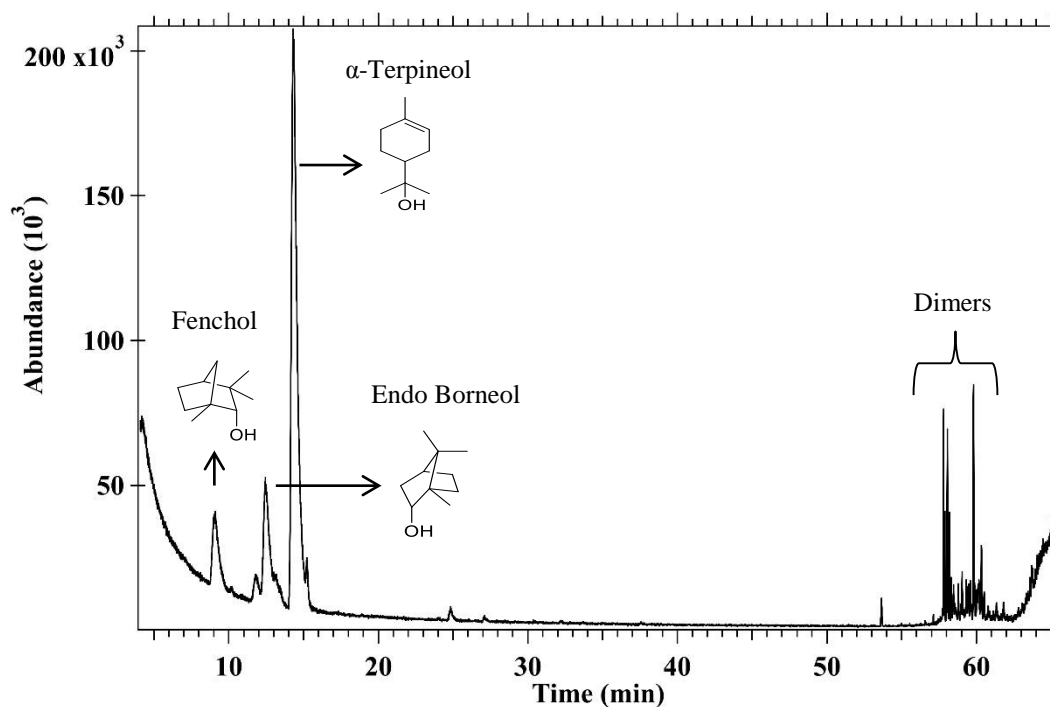


**Figure 25. Total Ion Chromatogram of Products for Reaction at RH = 30%.** Reveals that  $\alpha$ -terpineol is the major product followed by high molecular weight dimers, endo borneol and fenchol.

The TIC of the products generated as a result of reactions between ( $\alpha$ )-(+)-pinene and kaolinite does not display ( $\alpha$ )-(+)-pinene as an eluted surface adsorbed product. This indicates that after colliding with the kaolinite surface, ( $\alpha$ )-(+)-pinene is chemically



transformed via a reaction with the kaolinite surface. Thus, the TIC verifies that the FTIR peaks that change as the reaction progresses (Figure 20) do not indicate adsorbed pinene, but evidence distinct organic products formed as a result of chemical reactions. In order to identify the products in the TIC, the GC-MS compares the mass spectra of the products eluted from the GC at various time points to the mass spectra of compounds in a spectral library. Mass fragmentation patterns are unique to given compounds, thus, similarities between the mass spectra generated by NIST (National Institute of Standards and Technology) and the MS of our products, support the validity of our product determinations.

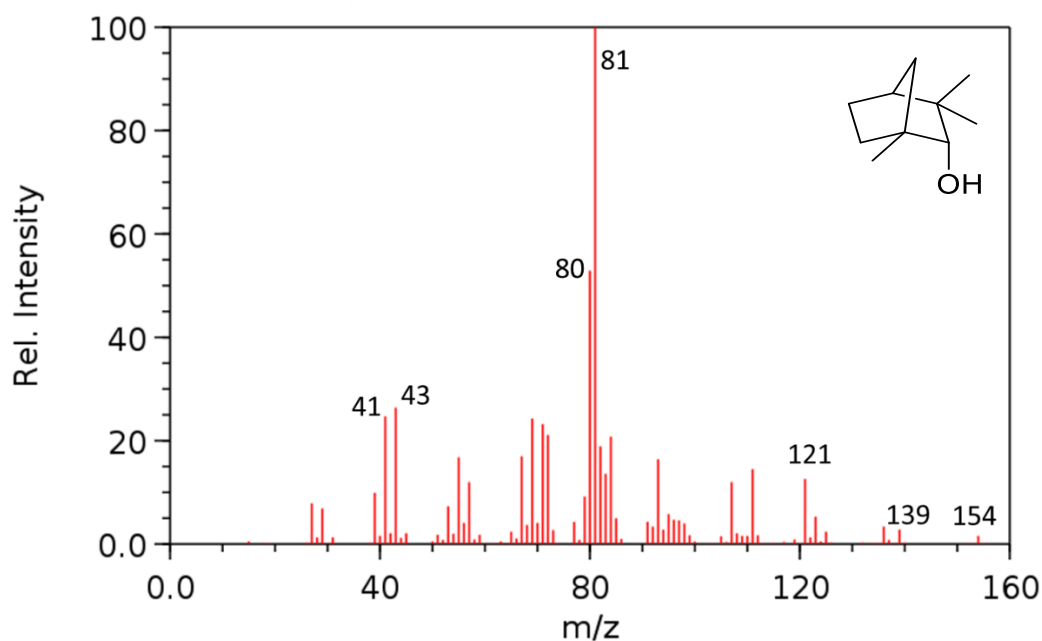


**Figure 26. Mass Spectrum of Standard Fenchol.** Cited from the National Institute of Standards and Technology database. Displays the unique fragmentation pattern of fenchol. The molecular ion of fenchol is evident at m/z 154 and m/z 139 indicate the loss of a methyl group. Other significant fragments include (m/z): 41, 80, 81, and 121.

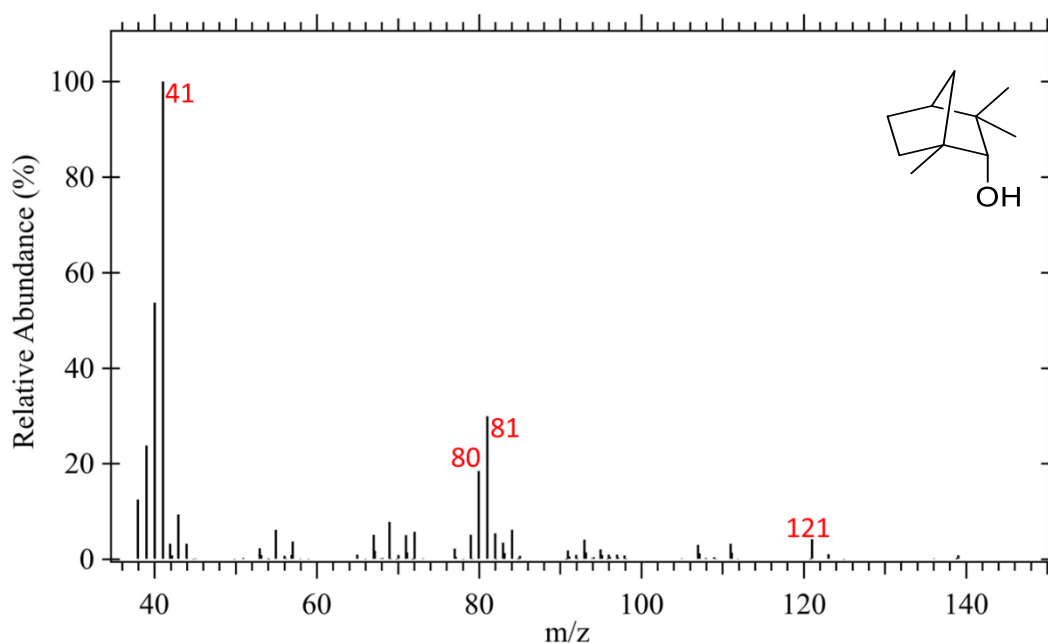


**Figure 27. Mass Spectrum of Fenchol Produced from Heterogeneous Reactions.** Displays fragmentation pattern of fenchol produced from reaction of  $\alpha$ -pinene and kaolinite. Does not display m/z 154 (molecular ion) or m/z 139 (loss of a methyl group). Fragmentation resembles that of pure fenchol. Similar fragments include (m/z): 41, 80, 81, and 121.

Comparisons between the NIST mass spectra of fenchol and the MS of heterogeneously produced fenchol reveal both similarities and differences; similar peaks indicate that fenchol reasonably characterizes the heterogeneously synthesized product in Figure 27. The atomic mass of fenchol is 154.25 amu; therefore, the m/z 154 peak in the NIST MS of fenchol corresponds to the molecular ion; the molecular ion is not observed in the MS of the fenchol product. The atomic mass of a methyl group (CH<sub>3</sub>) is approximately 15 amu; thus, the fragment at m/z 139 in the NIST MS of fenchol (Figure 26), which does not occur in the MS of heterogeneously produced fenchol, likely corresponds to the loss of a methyl group (Figure 28). Common fragments in the MS of

the fenchol product and the NIST MS of fenchol include  $m/z$  41,  $m/z$  80,  $m/z$  81, and  $m/z$  121; these fragments correlate to losses of various groups from the fenchol molecule.

Figure 28 outlines probable structures for the fenchol fragments observed in the mass spectra of standard and heterogeneously generated fenchol.

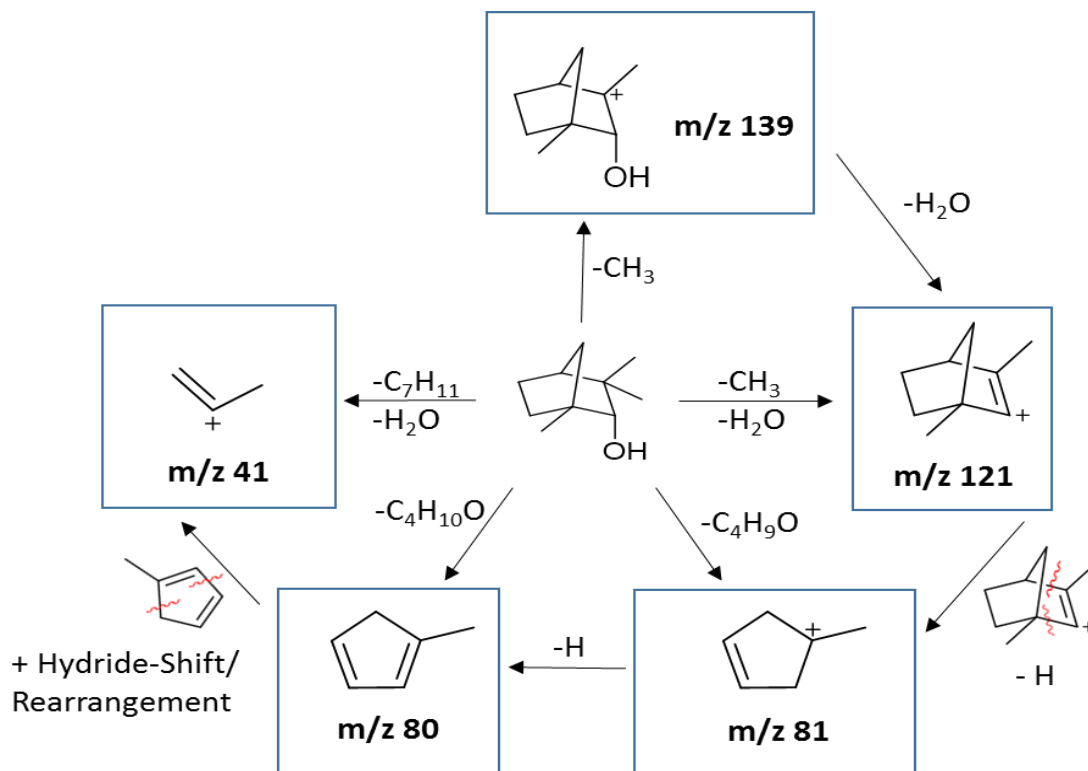


**Figure 28. Proposed Structures of Mass Fragments of Fenchol.** Red lines indicate places of bond cleavage. Illustrates the losses and structures associated with the mass fragments of fenchol ( $m/z$ ): 41, 80, 81, 121 and 139.

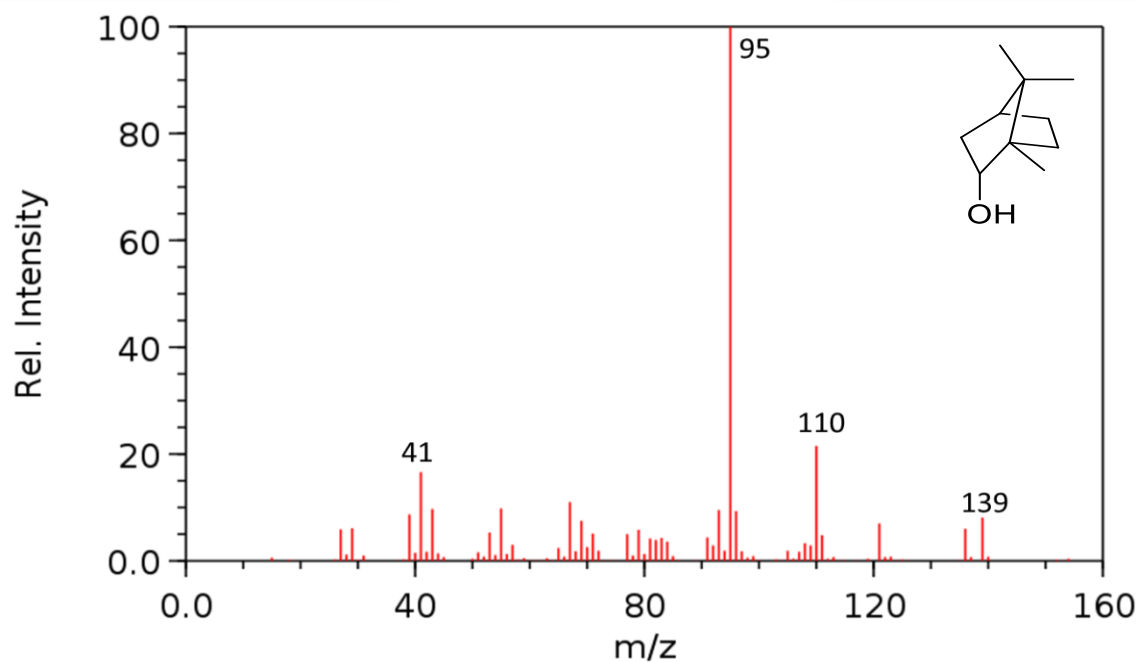


**Figure 29. Mass Spectrum of Standard Endo Borneol.** Cited from the National Institute of Standards and Technology database. Displays the unique fragmentation pattern of pure endo borneol. Significant fragments (m/z): 41, 95, 110, 136 and 139.

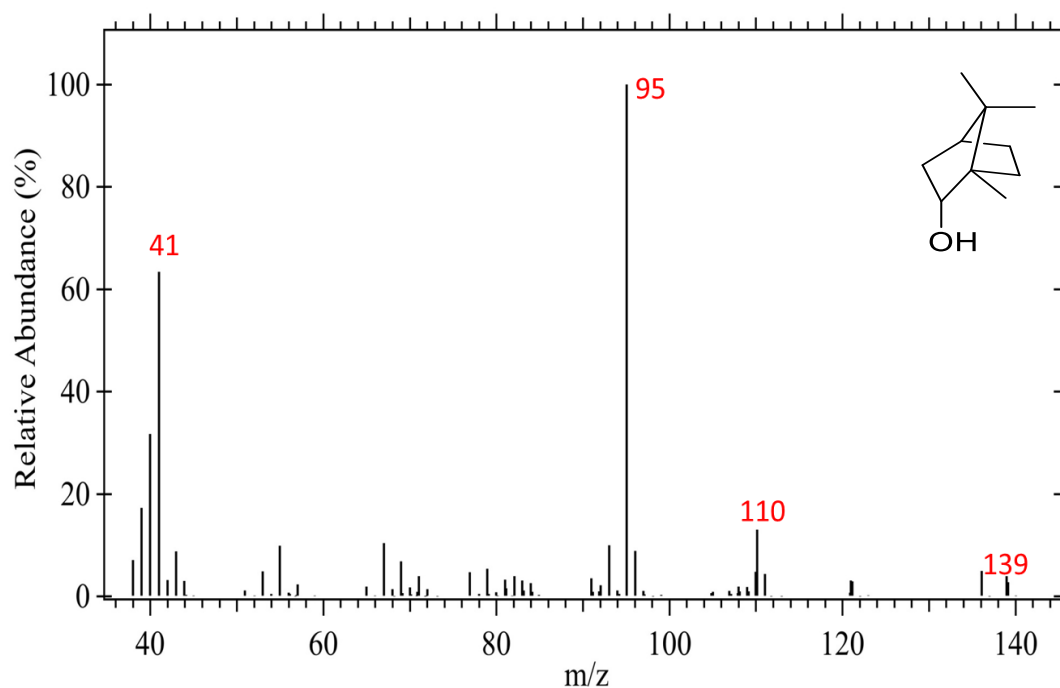


**Figure 30. Mass Spectrum of Endo Borneol Produced from Heterogeneous Reaction.** Displays fragmentation pattern of endo borneol produced from reaction of  $\alpha$ -pinene and kaolinite. Fragmentation resembles that of pure endo borneol. Similar fragments (m/z): 41, 95, 110, 136 and 139.

Similar to fenchol, the molecular weight of endo borneol is 154 amu, yet unlike the mass spectrum of standard fenchol, the mass spectrum of standard endo borneol does not display a molecular ion. The lack of a molecular ion in the MS of both standard and heterogeneously produced endo borneol suggests that the molecular ion is not stable. As with the mass spectra of fenchol, similarities between the distinct MS of standard endo borneol and heterogeneously formed endo borneol, support our product identification. For example, MS peaks such as  $m/z$  136 and  $m/z$  95, which occur in the NIST and experimental MS of endo borneol likely correlate, respectively, with the loss of a water molecule, and the combined loss of a  $C(CH_3)_2$  group and an alcohol. Other common fragments in the MS of the standard and product form of endo borneol include ( $m/z$ ) 41, 110, and 139; probable structures of the fragments are illustrated in Figure 31.

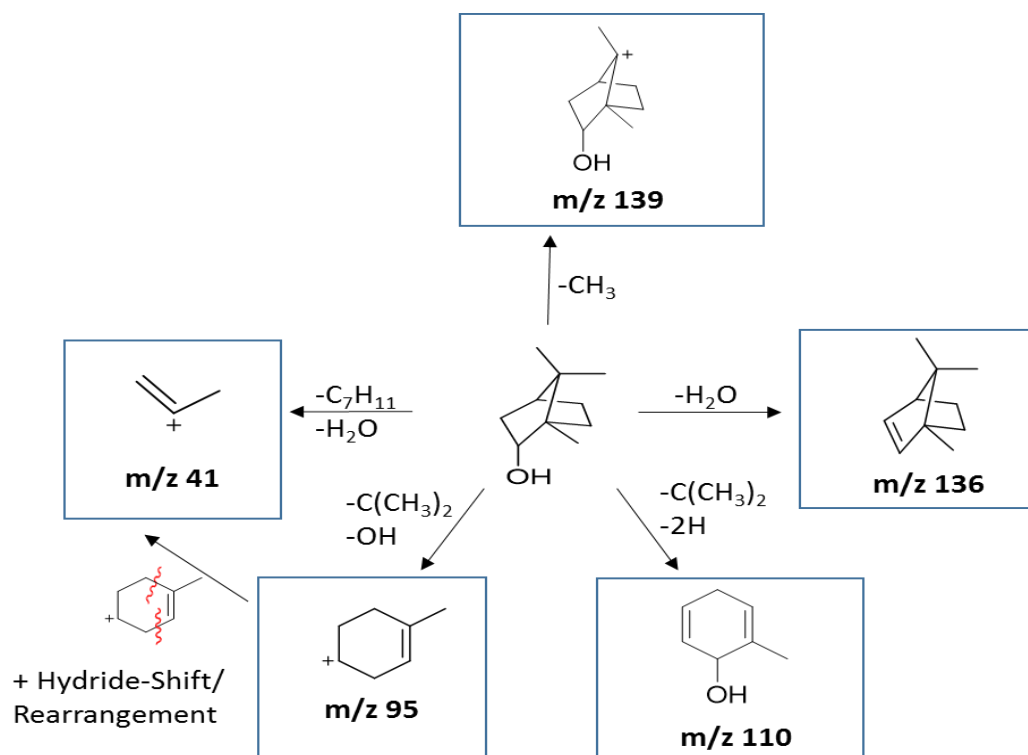


**Figure 31. Proposed Structures of Mass Fragments of Endo Borneol.** Red lines indicate places of bond cleavage. Illustrates possible sequential and non-sequential losses and structures associated with the mass fragments of endo borneol ( $m/z$ ): 41, 95, 110, 136 and 139. Note: formation of  $m/z$  136 and 110 involve methyl shifts.

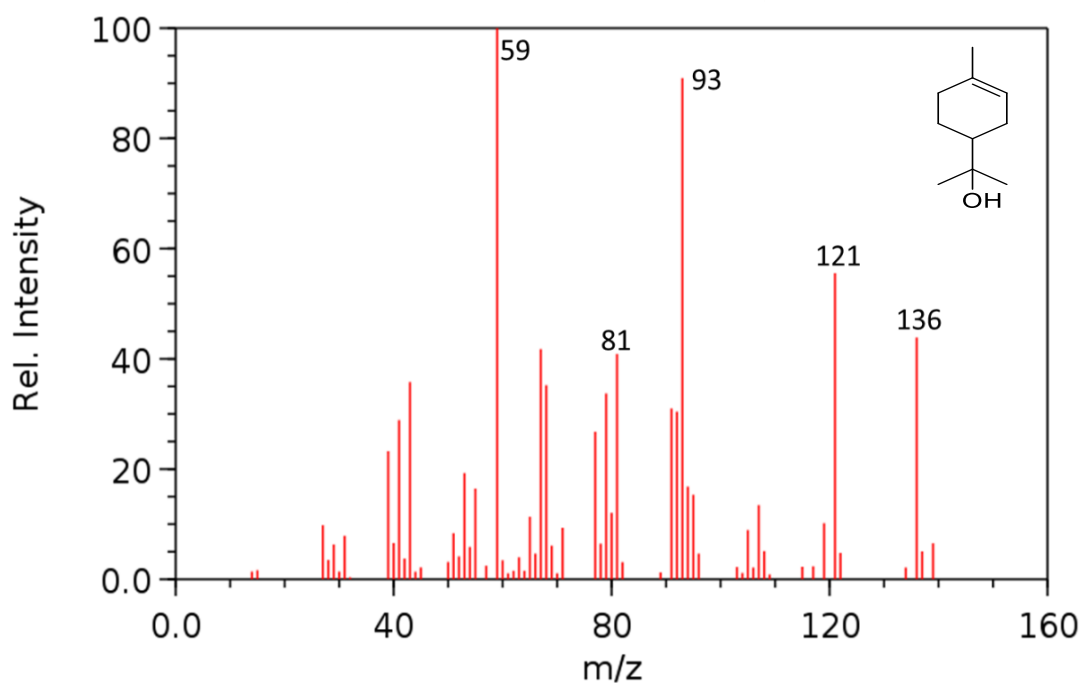


**Figure 32. Mass Spectrum of Standard  $\alpha$ -Terpineol.** Cited from the National Institute of Standards and Technology database. Displays the unique fragmentation pattern of pure  $\alpha$ -terpineol. Significant fragments (m/z): 59, 81, 93, 121 and 136.

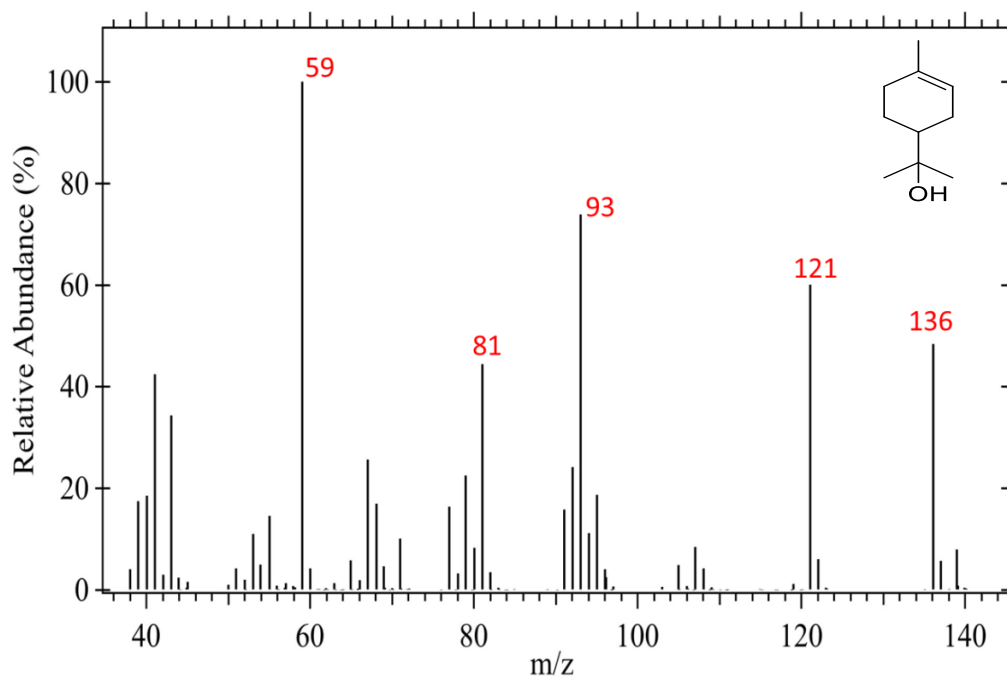


**Figure 33. Mass Spectrum of  $\alpha$ -Terpineol Produced from Heterogeneous Reaction.** Displays fragmentation pattern of  $\alpha$ -terpineol produced from reaction of  $\alpha$ -pinene and kaolinite. Fragmentation resembles that of pure  $\alpha$ -terpineol. Similar fragments include (m/z): 59, 81, 93, 121 and 136.

Although the molecular weight of  $\alpha$ -terpineol is also 154 amu, the mass spectra of standard and heterogeneously synthesized  $\alpha$ -terpineol are noticeably distinct from the MS of the other monomer organic products. Similarities between the mass spectra of standard  $\alpha$ -terpineol and  $\alpha$ -terpineol product validate that  $\alpha$ -terpineol is in fact generated as a result of reactions between ( $\alpha$ )-(+)-pinene and kaolinite. The MS of  $\alpha$ -terpineol, like that of endo bornoel, lacks a molecular ion which indicates that the molecular ion of  $\alpha$ -terpineol is unstable. Analogous fragment peaks between the MS of standard and heterogeneously synthesized  $\alpha$ -terpineol include (m/z) 59, 81, 93, 121 and 136. The most abundant fragment of  $\alpha$ -terpineol (m/z 59) appears to correlate with a bond cleavage resulting in the loss of the 6-membered ring along with a methyl group. The structure of the m/z 59 fragment is proposed in Figure 34 along with the structures and losses associated with the other fragments of  $\alpha$ -terpineol.

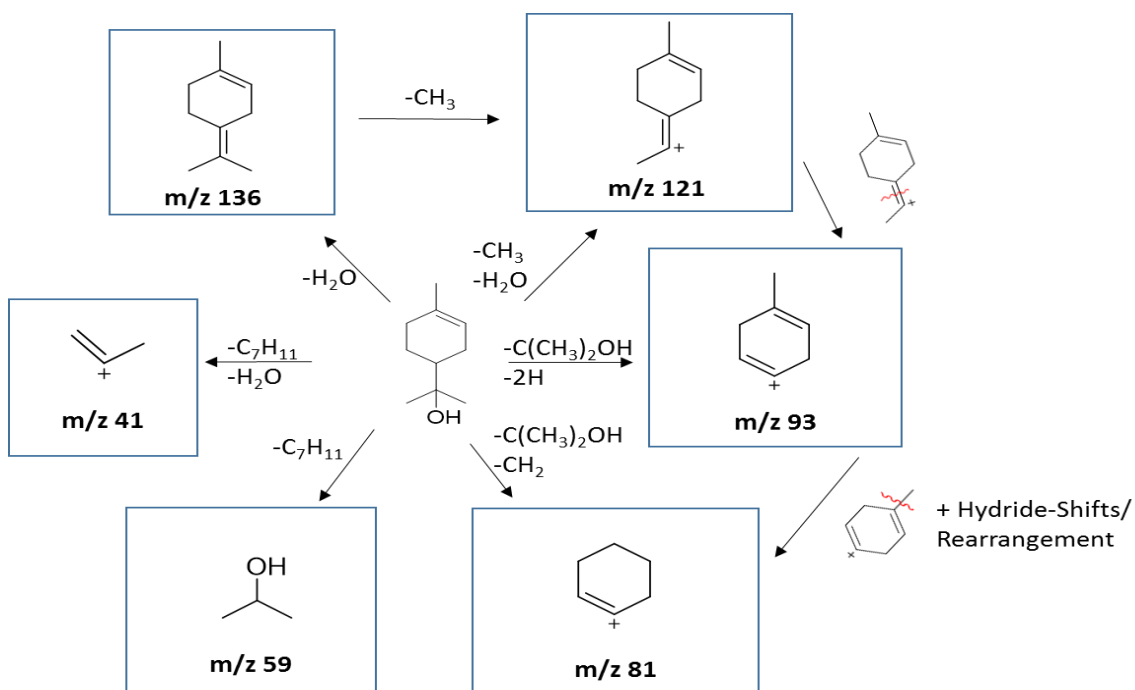


**Figure 34. Proposed Structures of Mass Fragments of  $\alpha$ -Terpineol.** Red lines indicate places of bond cleavage. Illustrates the losses and structures associated with the mass fragments of  $\alpha$ -terpineol (m/z): 41, 59, 81, 93 and 121.

Having identified the monomer products of heterogeneous reactions between ( $\alpha$ )-(+)-pinene and kaolinite using GC-MS, we can now consider the pathways by which the kaolinite surface facilitates the conversion of ( $\alpha$ )-(+)-pinene into the observed monomer organics (Figure 35).

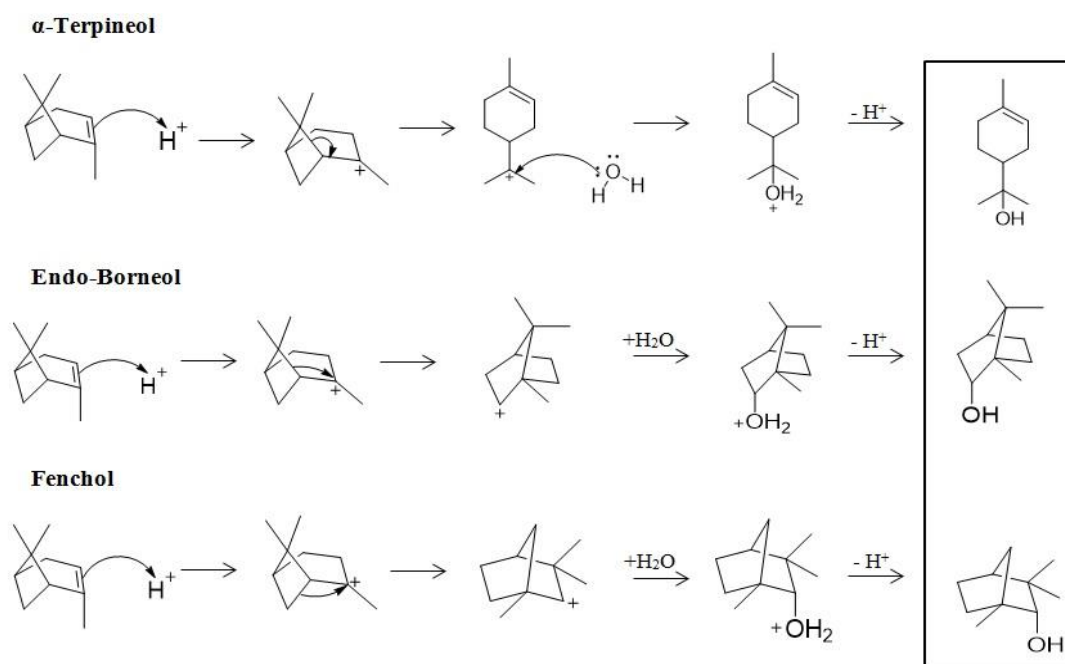


**Figure 35. Proposed Mechanisms for Formation of Major Organic Products.** Pathways for formation of  $\alpha$ -Terpineol, Endo Borneol and Fenchol can be attained via acid catalyzed hydration mechanisms.

In general, our analysis reveals that the mechanisms for the formation of  $\alpha$ -terpineol, endo borneol and fenchol involve the consumption of water. This hypothesis is supported by the observed decreases in the  $H_2O$  bending mode ( $1634\text{ cm}^{-1}$ ) of surface adsorbed water molecules displayed in Figure 20. It is likely that acidic protons or Lewis acid sites on kaolinite serve as catalysts for the formation of the observed products. We propose that the  $C=C$  in  $\alpha$ -pinene attacks an acidic proton on the kaolinite surface which



leads to the formation of a carbocation intermediate that is stabilized by the kaolinite surface via electrostatic interactions. The 4-membered ring of the first carbocation intermediate likely breaks as a result of angle strain which leads to the formation of a second more stable carbocation intermediate; the manner in which this 4-membered ring breaks leads to product differentiation. Once the second carbocation intermediate is generated, the most electron-deficient carbon of the second carbocation intermediate is then attacked by the oxygen atom of a water molecule. Finally, the abstraction of a proton by a basic site on the kaolinite surface yields a neutral oxygenated organic compound.

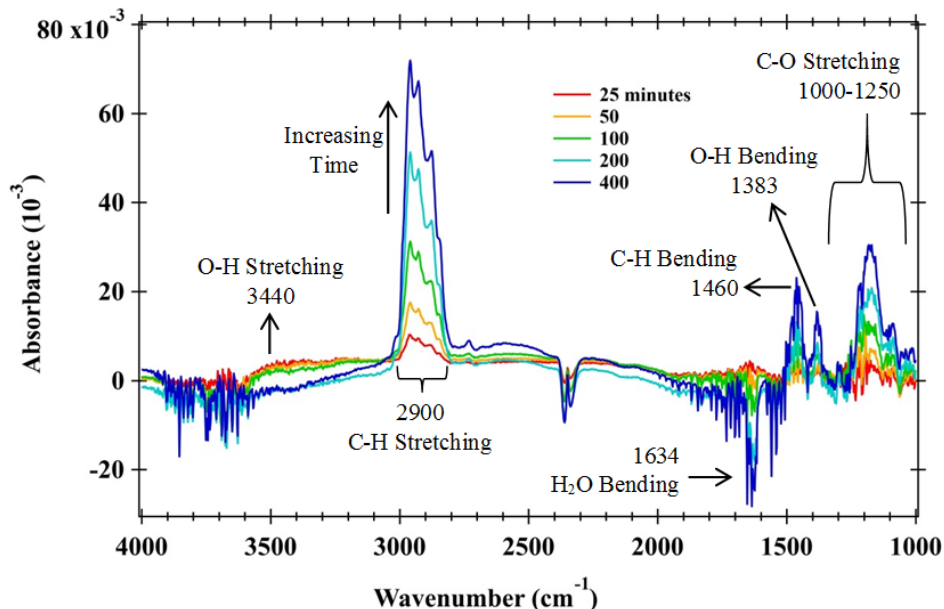


**Figure 20. Subtracted IR Spectra of Kaolinite Surface for Reaction at RH = 30% for Various Time Points.** Note: loss in absorbance at  $2350\text{ cm}^{-1}$  corresponds to loss of  $\text{CO}_{2(g)}$  over time. Heights of C-H ( $2900\text{ cm}^{-1}$ ) peaks increase and heights of  $\text{H}_2\text{O}$  bends ( $1634\text{ cm}^{-1}$ ) decrease over time. Demonstrates increasing concentration of organic product adsorbed to kaolinite surface over time and loss of  $\text{H}_2\text{O}$  as reaction progresses.

The proposed mechanisms of formation and the structures of the organic monomer products identified by GC-MS analyses agree with the various vibrational modes evidenced in the subtracted FTIR spectrum throughout the reaction (Figure 20).

The large growth in the C-H stretching band ( $2900\text{ cm}^{-1}$ ) and moderate growth in the C-H bending bands ( $1460\text{ cm}^{-1}$ ) throughout the reaction can be attributed to the formation and accumulation of  $\alpha$ -terpineol, organic dimers, endo borneol and fenchol on the kaolinite surface. The significant increase of the C-O stretching band ( $1000\text{-}1250\text{ cm}^{-1}$ ) and the relatively smaller increase of the O-H bending mode ( $1383\text{ cm}^{-1}$ ) as the reaction progresses evidence the alcohol (OH) groups in  $\alpha$ -terpineol, endo borneol and fenchol. Keeping in mind that absorbance is proportional to concentration and absorptivity, which varies for C-H, C-O and O-H bonds, the relatively larger increase in the C-H stretching bands relative to that of the C-O and O-H stretching bands correlates with the fact that the identified monomer products are not heavily oxidized; we can only hypothesize that this findings suggests that dimer products are also not heavily oxidized. We will consider the structures of the dimer products in greater detail in Section 3.4.

Having verified the identity of the monomer products generated as result of heterogeneous reactions between  $\alpha$ -pinene and kaolinite, we can now consider the contribution of these monomer products to SOA. The monomer organic products,  $\alpha$ -terpineol, endo borneol and fenchol, all have molecular weights of 154.25 amu and contain a single alcohol group. While the organics produced as a result of reactions between limonene and kaolinite also contained alcohol groups, they were composed solely (99 %) of limonene diol, which has a molecular weight of 170.25 amu and contains 2 alcohol groups. Thus, the monomer organic products of reactions between limonene and kaolinite were less differentiated and slightly heavier than the ones observed in this study. While they are not particularly large, the monomer products of reactions between  $\alpha$ -pinene and kaolinite each contain an alcohol group which

corresponds to a significant vapor pressure reduction. In Chapter 1, we observed that the addition of a single alcohol group reduces the vapor pressure of an organic compound by a factor of  $5.7 \times 10^{-3}$ . Hence, the strong hydrogen-bonding interactions that can occur between various monomer products makes them more likely to remain bound to the surface of a mineral particle. Therefore, we can conclude that reactions between  $\alpha$ -pinene and kaolinite generate lower volatility compounds that can be viable components of SOA.

### 3.4. Identification and Discussion of Dimer Products Using GC-MS

The production of high molecular weight dimers as a result of reactions between ( $\alpha$ )-(+)-pinene and kaolinite further suggests that heterogeneous pathways can contribute to the formation of secondary organic aerosols. Determining the mechanisms of formation and the structures of these extremely low volatility compounds will provide insight into the role that dimers play in heterogeneously generated SOA. Using GC-MS analyses, we propose possible mechanisms and structures for the dimer compounds produced as a result of the reactivity that we observe between ( $\alpha$ )-(+)-pinene and kaolinite.

Gas chromatography separates organic products on the basis of polarity and size; therefore, the eluted products corresponding to high molecular weight organics have relatively high retention times ranging from 57 to 62 minutes. When we look closely at this region of the TIC, we observe that relative to peaks corresponding to the monomer products, peaks between 57 and 62 minutes are significantly sharper and have very similar retention times. Thus, we can reasonably assume that the various peaks

correspond to mixtures of chemically similar fragments of the dimer products as opposed to chemically unique high molecular weight compounds (Figure 36).

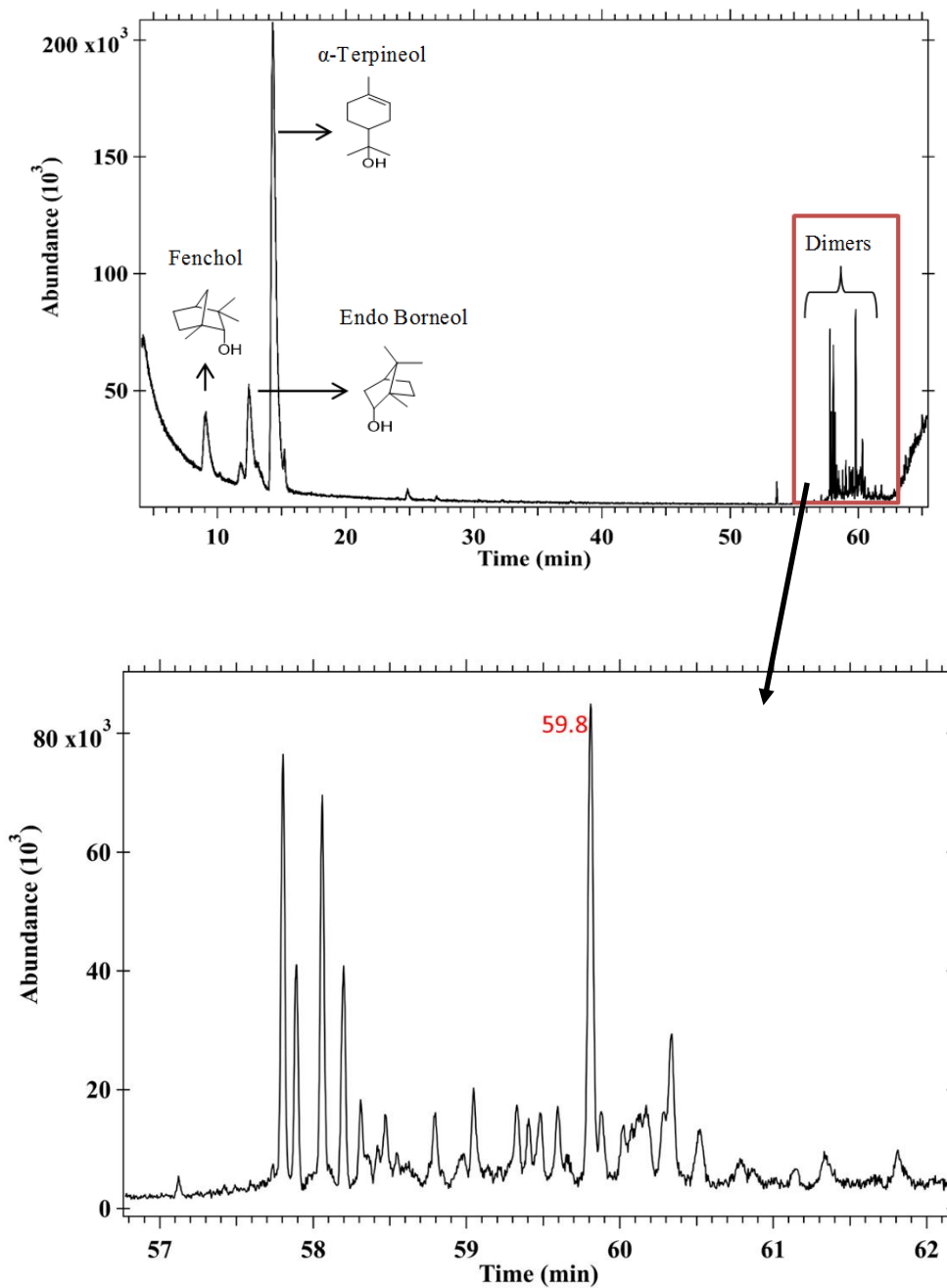


**Figure 36.** Total Ion Chromatogram of Dimer Products Eluted between 57 and 62 Minutes. TIC peaks of eluted dimer fragments are very sharp and have similar retention times. Hence, peaks in the TIC correspond to dimer fragments as opposed to intact dimer structures.

Figure 36 displays that among the various fragmented dimer peaks in the TIC, the peak with a retention time of approximately 59.8 min has the highest relative abundance and likely indicates the most stable fragments generated from the dimer products. The mass spectrum associated with this peak in the TIC is illustrated by Figure 37.

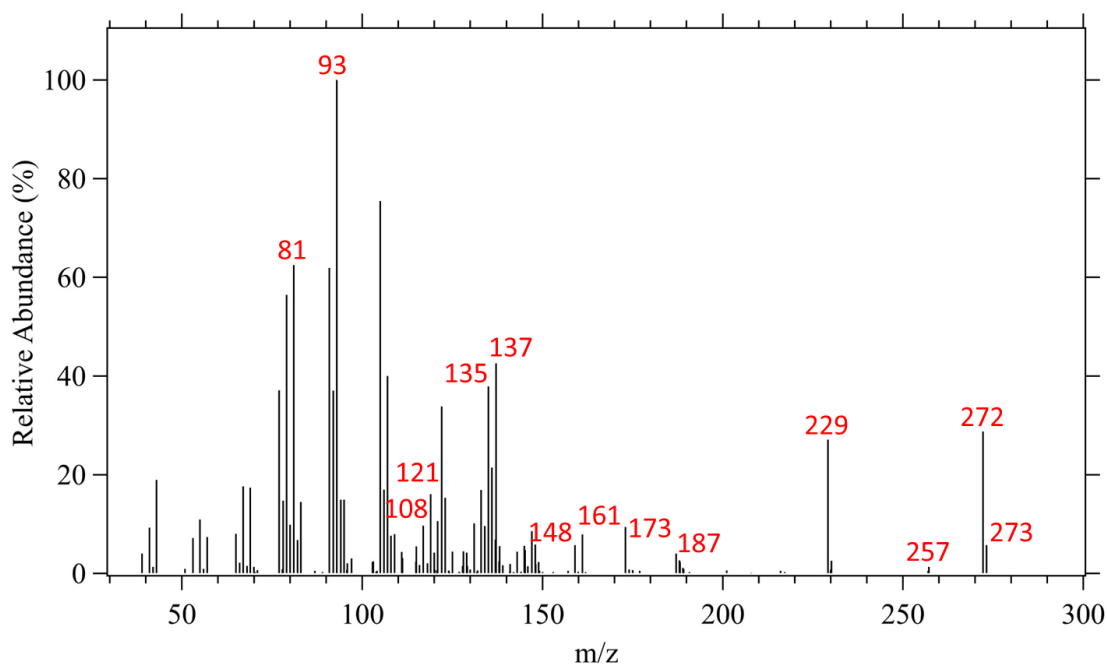


**Figure 37. MS of Dimer Fragments Eluted at 59.8 min.** These fragments were the most abundant in the TIC and likely correlate to the most stable dimer fragments. High molecular weight fragments provide information about the possible structure of the dimers. Significant peaks include (m/z): 161, 173, 187, 229, 257, 272 and 273.

Due to the fact that the dimer products are highly fragmented by GC-MS analyses, we can assume that the mass spectrum depicted in Figure 37 does not contain a molecular ion peak corresponding to an intact dimer product. However, the mass spectrum of the dimer fragments eluted at 59.8 minutes evidences several peaks with mass to charge ratios that exceed the molecular weight of both ( $\alpha$ )-(+)-pinene (136 amu) and the monomer products (154 amu). Therefore, while we cannot make conclusive assessments of the structures of the dimer products formed as a result of the reaction

between ( $\alpha$ )-(+)-pinene and kaolinite, peaks with relatively high  $m/z$  values can be used to postulate the dimer structures.

In order to explain the mass fragmentation patterns we observe for the high molecular weight dimer fragments eluted from the GC-MS, we can consider a variety of pathways by which dimer compounds may be formed. The dimer products observed by Duporte et al. as a result of reactions between  $\alpha$ -pinene and ammonium sulfate particles were generally formed as a result of linkages via an oxygen atom or oxygen containing functionality, between two oxidized products (Duporte et al., 2016). If we consider that dimers formed from reactions of  $\alpha$ -pinene and kaolinite have the same general structure as those reported by Duporte et al., then we can suppose that they may be comprised of identical or different monomer compounds.

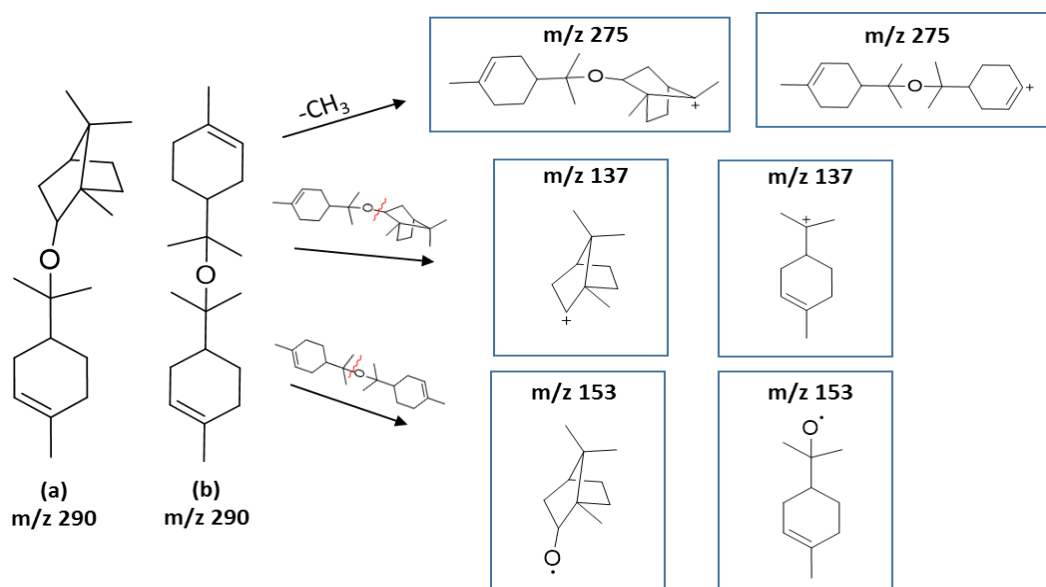


**Figure 38. Possible Dimer Structures Modeled after Duporte et al. Dimers.** Dimers are formed from linkages between monomer products via an oxygen atom. (a) Dimer formed from  $\alpha$ -terpineol and endo borneol (b) dimer formed from two  $\alpha$ -terpineol molecules. Possible fragments of these proposed structures are not consistent with the pattern of fragmentation observed in the MS of the fragments eluted at 59.8 min.

Structure (a) of Figure 38 illustrates a possible dimer formed from  $\alpha$ -terpineol and endo borneol and structure (b) depicts a dimer generated from two molecules of  $\alpha$ -terpineol; both of these potential dimer compounds have an ether functionality and a molecular weight of approximately 290 amu. Possible fragments of these potential compounds would likely result from losses of methyl groups or breakage at the oxygen linkages. However, dimers resulting from these patterns of fragmentation do not explain peaks in the MS of the dimer fragments (Figure 37) that correspond to larger fragments such as  $m/z$  272,  $m/z$  257 and  $m/z$  229. Therefore, it is unlikely that the dimers generated from the heterogeneous reaction of  $\alpha$ -pinene and kaolinite can be fully characterized by the structures proposed in Figure 38. The  $m/z$  272 peak in particular, would correspond to a loss of 18 amu from an initial molecular weight of 290 amu, which would correlate with the loss of a water molecule. Due to the fact that the dimers proposed in Figure 38 do not possess alcohol groups, the loss of molecular water as a result of ionization in the MS instrument would not be possible. Thus, the general structures of the  $\alpha$ -pinene derived dimers observed by Duporte et al. may not be the best model for the dimers observed in this study.

Thus far, our analysis suggests that the dimer structures may contain alcohol groups; therefore, we can consider an alternative formation pathway for the dimer products that does not generate an ether functionality. A potential mechanism and structure for the dimers formed as a result of reactions between ( $\alpha$ )-(+)-pinene and kaolinite is proposed in Figure 39; this structure appears to correlate well with the MS generated for the dimer fragments eluted at 59.8 min (Figure 37).

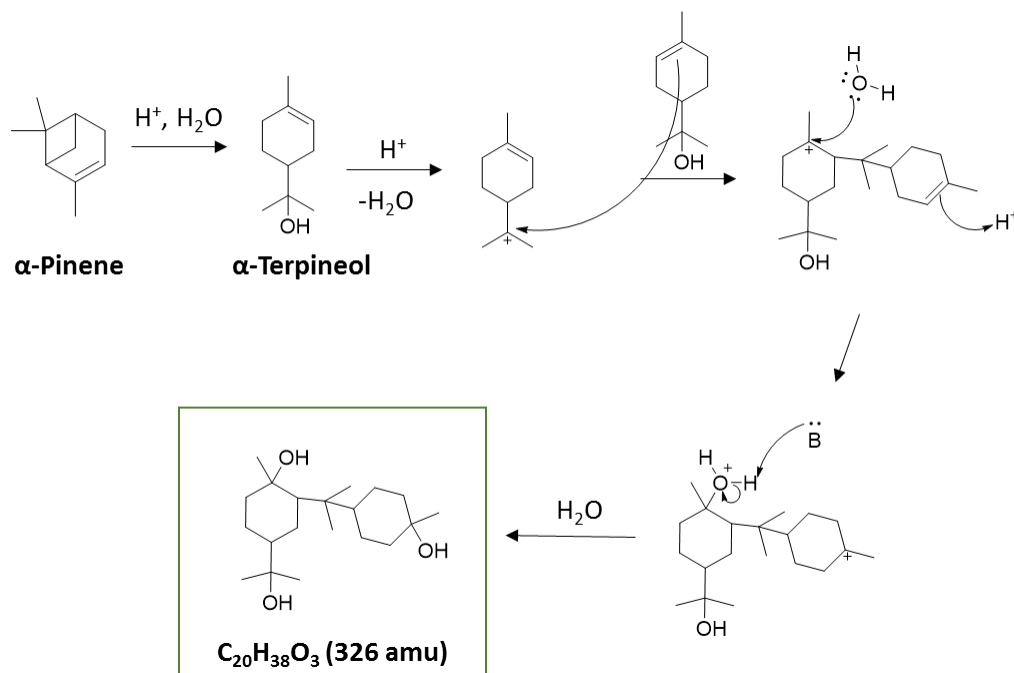


**Figure 39. Mechanism and Structure for the Formation of Proposed  $C_{20}H_{38}O_3$  Dimer.** Note: (B) denotes a generic base. The proposed  $C_{20}H_{38}O_3$  dimer is formed from two molecules of  $\alpha$ -terpineol. The formation of this dimer may involve the loss of water from one molecule of  $\alpha$ -terpineol to generate a carbocation which is then attacked by the alkene (C=C) of another  $\alpha$ -terpineol molecule. Acid catalyzed hydration may lead to the  $C_{20}H_{38}O_3$  dimer which has a molecular weight of 326.52 amu.

The proposed dimer structure is formed from two molecules of  $\alpha$ -terpineol and has a chemical formula of  $C_{20}H_{38}O_3$  and a molecular weight of 326.52 amu. In the proposed pathway for the formation of  $C_{20}H_{38}O_3$ , the alcohol group of  $\alpha$ -terpineol attacks an acidic proton (likely supplied by the kaolinite surface) to generate water, which is a good leaving group. Considering steric hindrances, it is likely that the water molecule leaves which results in the production of a carbocation intermediate; thereafter, the alkene (C=C) group of another  $\alpha$ -terpineol molecule can attack the carbocation intermediate in order to form a carbocation dimer intermediate. Finally, the acid-catalyzed addition of water may lead to the formation of the dimer compound. Possible fragments that can be



generated from  $C_{20}H_{38}O_3$  are consistent with the MS for the dimer fragments eluted at 59.8 min (Figure 40).

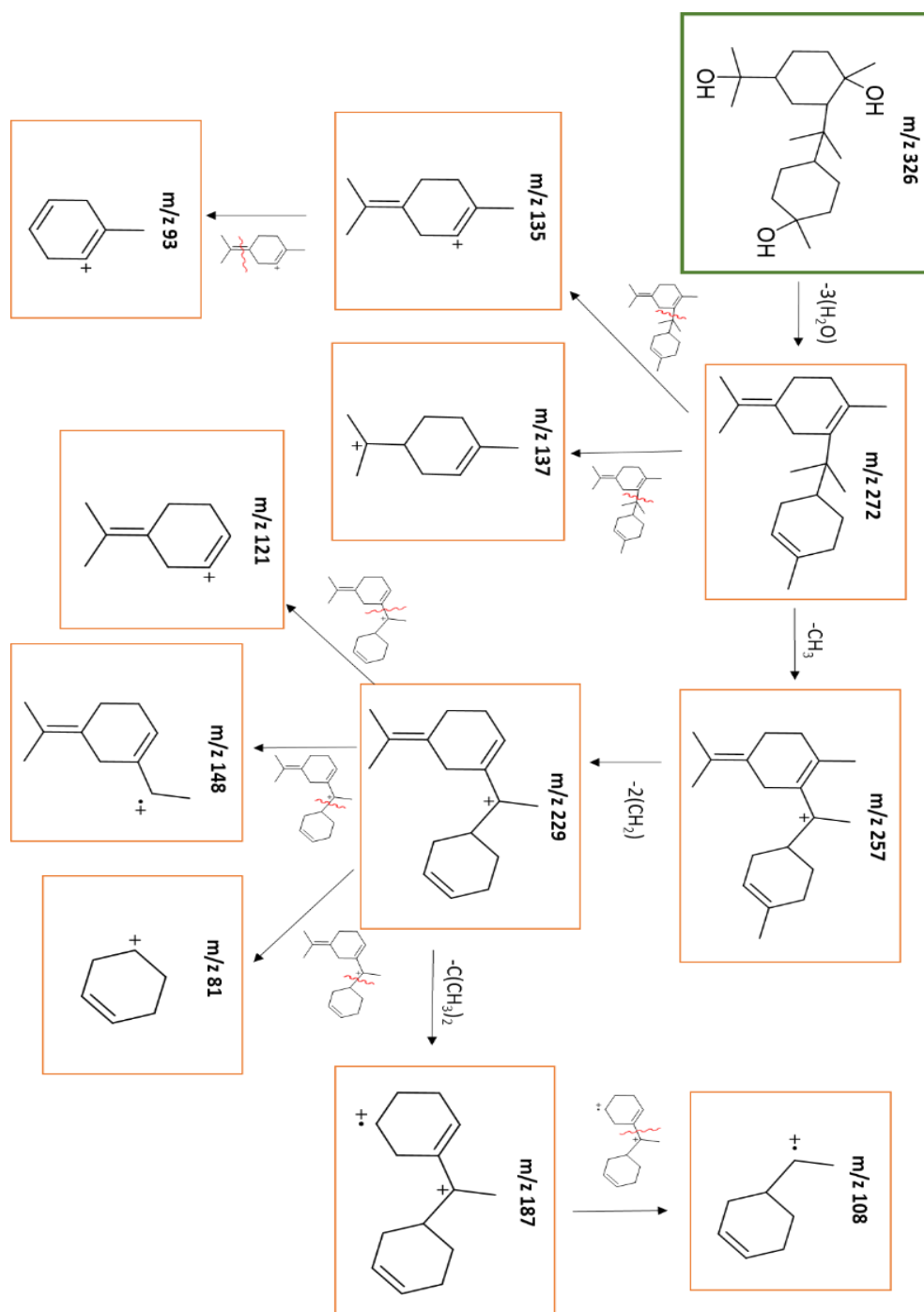


**Figure 40. Proposed MS Fragment Pattern of Potential  $C_{20}H_{38}O_3$  Dimer.** Red lines indicate possible points of cleavage. Possible MS fragments generated from the  $C_{20}H_{38}O_3$  dimer may occur as a result of sequential and non-sequential losses of various groups. The probable  $C_{20}H_{38}O_3$  dimer fragmentation pattern is consistent with the MS of the eluted dimer fragments at 59.8. Although, the  $C_{20}H_{38}O_3$  structure does not explain all of the significant MS fragments above

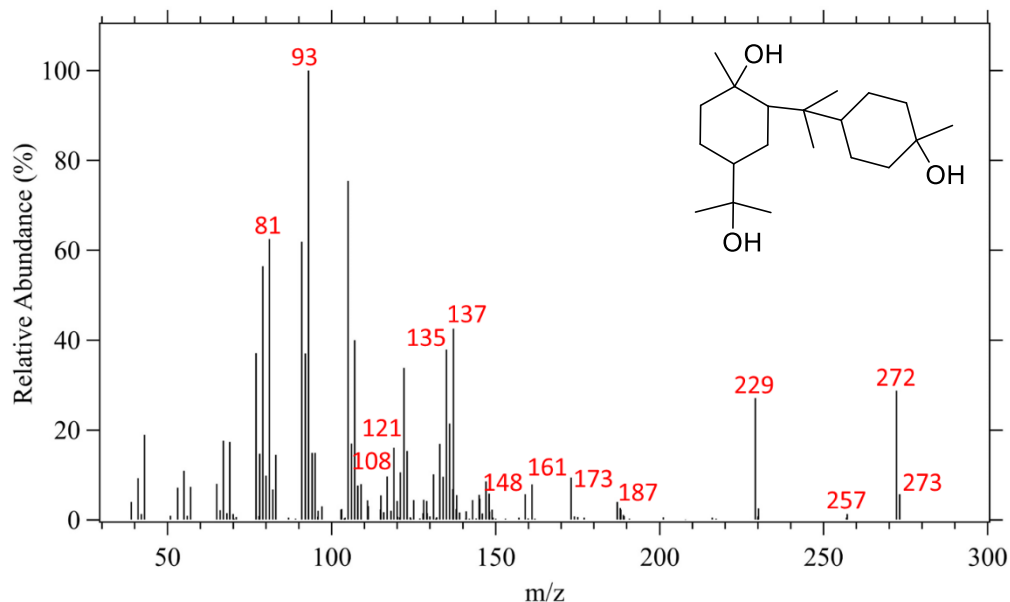


**Figure 37. MS of Dimer Fragments Eluted at 59.8 min.** These fragments were the most abundant in the TIC and likely correlate to the most stable dimer fragments. High molecular weight fragments provide information about the possible structure of the dimers; significant high m/z peaks include (m/z): 161, 173, 187, 229, 257, 272 and 273. Possible  $C_{20}H_{38}O_3$  structure appears to be consistent with fragments in this MS.

The molecular ion for the proposed  $C_{20}H_{38}O_3$  dimer would result in a peak in the MS at m/z 326; this molecular ion is likely unstable because it is absent from the MS. The fragment at m/z 272 likely correlates to the loss of three water molecules from the molecular ion. The peak at m/z 273 likely indicates the presence of  $^{13}C$  isotopes in the fragment generated from the loss of three water molecules; using the fact that each carbon will have multiplicative contribution of approximately 1.08 to the M+1 peak, we can use Equation 15 to approximate the number of carbon atoms present in the m/z 273 fragment (Harris 2010).

$$\begin{aligned} \# \text{ of } \_ \text{ carbons} &= \frac{(M + 1 \text{ abundance}) \div (M \text{ abundance})}{1.08\%} \times 100\% && \text{(Eq. 15)} \\ &= \frac{5.7429 \div 28.738}{1.08} \times 100 = 18.5 \end{aligned}$$

Although this type of calculation is typically performed for the molecular ion peak, we can use it to approximate that the  $m/z$  272 fragment contains about 19 carbon atoms; this observation is consistent with the proposed  $C_{20}H_{38}O_3$  dimer structure. The MS fragment at  $m/z$  257 may correspond to the loss of a methyl group from the  $m/z$  272 fragment and the  $m/z$  229 fragment may correspond to the loss of two ethyl ( $CH_2$ ) groups from the  $m/z$  257 fragment. The  $m/z$  187 peak may correspond to the loss of a  $C(CH_3)$  group from the  $m/z$  229 fragment. While our proposed structure agrees with some fragment peaks corresponding to molecular weights below 154 amu, other fragments with molecular weights above 154 amu, such as  $m/z$  173 and  $m/z$  161 are difficult to explain using the proposed  $C_{20}H_{38}O_3$  structure. The inability to explain these peaks may indicate that the proposed dimer structure does not accurately characterize the dimer products or may indicate the presence of other dimer products. Yet, the consistency of the proposed  $C_{20}H_{38}O_3$  dimer with multiple higher molecular weight fragments in the MS suggests that this structure is a viable starting point for determining the structure of the dimers resulting from reactions between ( $\alpha$ )-(+)-pinene and kaolinite.

Identifying the structure of the dimer products allows us to better characterize SOA generated from reactions between mineral dust aerosols and  $\alpha$ -pinene. The dimers observed by Cheshchevoi et al. 1989 as a result of reactions between saturated  $\alpha$ -pinene vapor and kaolinite clay had molecular weights of approximately 500 amu, which is nearly 1.5 times the magnitude of our proposed  $C_{20}H_{38}O_3$  dimer structure (326 amu). While the difference between the molecular weights is likely due to the fact that Cheshchevoi et al. performed their heterogeneous reactions under dry conditions, the potential for dimer compounds to possess relatively large molecular weights is made

evident by their findings. At a relative humidity level of 30 %, the  $C_{20}H_{38}O_3$  dimer compound that we propose has a molecular weight that is more than twice the magnitude of a molecule of  $\alpha$ -pinene (137 amu) or any one of the monomer organic products (154 amu). Due to the relatively large number of atoms that make them up, dimer compounds experience significant London-dispersion intermolecular forces that inhibit them from partitioning into the gas-phase. Hence, dimer compounds are considerably more likely to remain in the condensed phase once they are formed on the surface of a mineral particle and permanently alter the chemical nature of the mineral dust particle. Therefore, the formation of dimer compounds on the surface of kaolinite as a result of reactions with  $\alpha$ -pinene is a primary mechanism for the growth of SOA derived from this source. The extent to which dimer compounds are irreversibly bound to the surface of a mineral particle can be enhanced by the presence of polar groups in the dimer structures. In Chapter 1, we observed that the dimers formed as a result of gas-phase mechanisms between  $\alpha$ -pinene and ozone observed by Zhang et al. and Ehn et al. were highly oxygenated and had between 5 and 18 oxygen atoms; both Zhang et al. and Ehn et al. reported that dimer compounds were a significant portion of the SOA they observed. Similarly, dimer compounds generated from heterogeneous reactions between  $\alpha$ -pinene and ammonium sulfate seed particles were heavily oxidized, having between 5 and 11 oxygen atoms (Iinuma et al., 2007; Duporte et al., 2016). Unlike the heterogeneous dimer formation observed by Iinuma et al. and Duporte et al., the dimers we observe as a result of reactions between  $\alpha$ -pinene and kaolinite may not be heavily oxidized. This difference is reasonable when we consider that kaolinite, unlike ammonium sulfate particles, catalyzes the oxygenation of  $\alpha$ -pinene by water molecules and cannot contribute oxygen-

rich sulfate structures to the dimer compounds. Additionally, the reactions performed by Iinuma et al. and Duporte et al. were conducted in the presence of ozone ( $O_3$ ) which presents a significant difference between the heterogeneous reactions they studied and those observed in this study. Yet, the possibility that the dimers we observe may contain alcohol groups has significant implications in terms of the volatility of these compounds. The structure of the potential  $C_{20}H_{38}O_3$  dimer contains three alcohol groups; in Chapter 1, we also observed that the addition of a single alcohol group to a volatile organic compounds reduces the vapor pressure of the organic by three orders of magnitude. The presence of oxygen atoms and polar groups in a dimer allows it to experience strong dipole-dipole intermolecular interactions in addition to London-dispersion forces. Therefore, the presence of alcohol groups in the structures of dimer compounds indicates that dimers are far more irreversibly bound to the mineral surface and have a greater ability to promote SOA growth. Hence, determining the exact chemical composition of the dimers produced as a result of heterogeneous reactions between kaolinite and  $\alpha$ -pinene is an ongoing investigation in the Hinrichs lab and is critical in order to characterize the degree to which these reactions contribute to SOA. Yet, the likelihood that high molecular weight dimers containing alcohol groups can be formed as a result of heterogeneous reactions suggests that heterogeneous pathways can significantly impact both SOA quantities, due to the abundance of mineral particles, and SOA size.

## **4.0. The Effect of Relative Humidity on Reactions between ( $\alpha$ )-(+)-Pinene and Kaolinite**

### **4.1. The Importance of Relative Humidity in Atmospheric Chemistry**

While we have established that ( $\alpha$ )-(+)-pinene can react with kaolinite to form significantly less-volatile organic products, we must now consider how the presence of water vapor in the atmosphere impacts this reactivity. Verifying that organic product formation persists within a range of humid conditions will suggest that heterogeneous reactions involving  $\alpha$ -pinene that promote SOA formation and growth can be considered atmospherically relevant processes. According to the mechanistic model proposed in Chapter 3, the likelihood that a reaction between  $\alpha$ -pinene and mineral dust will occur in the atmosphere depends on whether  $\alpha$ -pinene can successfully access the reactive sites on the mineral surface when a collision takes place. Therefore, the adsorption of water molecules to mineral surfaces, which is depicted by DRIFTS spectra of kaolinite clay, reduces the availability of reactive surface sites. Thus, studying the adsorption of water onto mineral surfaces will provide insight into how water vapor affects reactions between mineral dust particles and volatile organic compounds in the atmosphere.

### **4.2. Modeling Water Uptake on the Kaolinite Surface**

In order to monitor the adsorption of water on kaolinite at varying relative humidity levels we used DRIFTS. The procedure used in this study of water uptake was modeled after the method described by Angelini et al, 2007. Dehumidified kaolinite was sequentially exposed to the following relative humidity levels: 3.9 %, 11.4 %, 14.9 %, 22.4 %, 27.6 %, 33.2 %, 44.5 %, 53.5 %, 65.5 %, and 71.8 %, by varying the flow rates of humidified and dry air. At each relative humidity level, after 20 minutes of

equilibration, an IR spectrum of the clay surface was collected. The spectra were subtracted from a spectrum of dry kaolinite prior to equilibration at each relative humidity level in order to generate spectra of only surface adsorbed water (Figure 41).

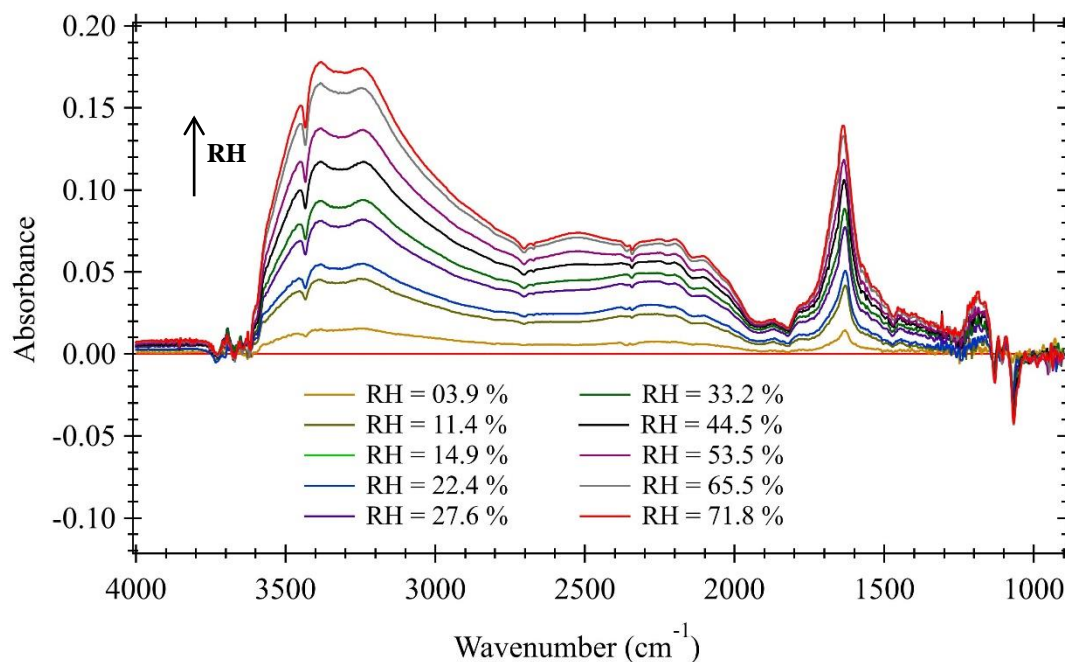


**Figure 41. Subtracted Spectra of Surface-Adsorbed Water on Kaolinite Surface.** Increased absorbance of surface-adsorbed water bending ( $1634\text{ cm}^{-1}$ ) and surface hydroxyl stretching ( $3590\text{--}2000\text{ cm}^{-1}$ ) bands indicates increased surface-adsorbed water content as relative humidity level rises.

In Figure 41, the broad stretching mode bands in the region of  $3590\text{ to }2000\text{ cm}^{-1}$  evidence increases in strong hydrogen bonding interactions between surface hydroxyl (OH) groups and surface adsorbed water molecules. The bending mode absorption peaks centered at  $1634\text{ cm}^{-1}$  correspond primarily to surface-adsorbed water molecules (Angelini et al, 2007). Figure 41 displays that as relative humidity increases, absorbance in these characteristic regions increases. The bending absorption peaks associated with surface-adsorbed water to the kaolinite surface ( $1758.8\text{ to }1538.9\text{ cm}^{-1}$ ) were integrated for all the spectra taken at the indicated relative humidity levels. The integrated

absorbance values represent the relative quantities of water adsorbed to the kaolinite surface at given relative humidity levels. A plot of integrated absorbance versus relative humidity level (Figure 42) illustrates that the quantity of water adsorbed to the kaolinite surface increases as a function of relative humidity level.

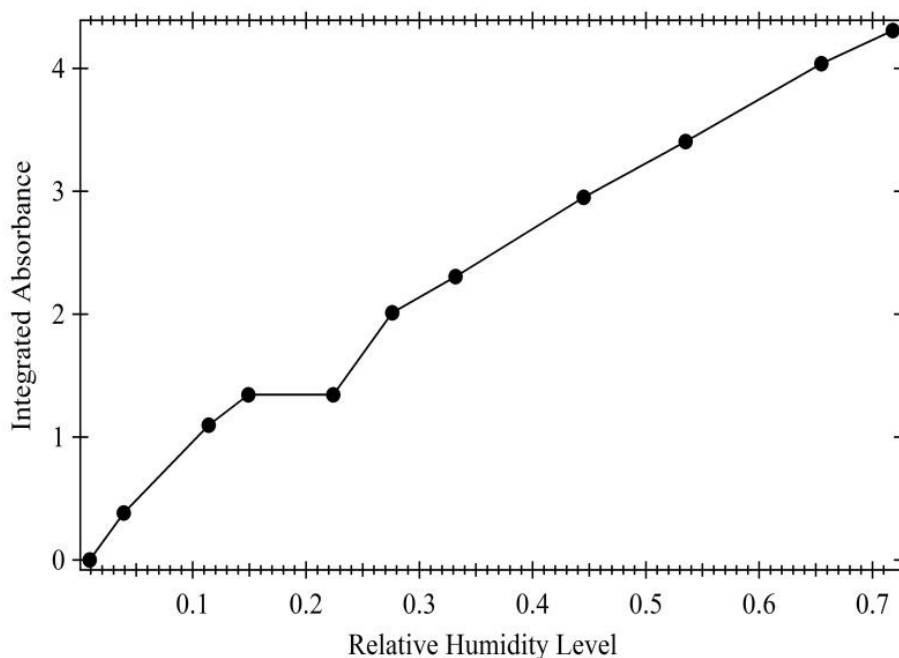
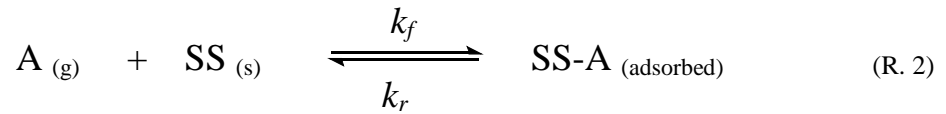


**Figure 42. Integrated Absorbance vs. Relative Humidity Level for Surface-Adsorbed Water.** Reveals that water content on clay surface increases as a function of relative humidity level. Note: RH = 20 % is simply a poor data point and is likely due to a fluctuation the experimental method.

In order to model the adsorption of gaseous water molecules to the surface of kaolinite, there are a variety of theories that we can consider. Langmuir-style adsorption is described by Reaction 2 where  $A$  represents a gas-phase molecule,  $SS$  represents an available surface site and  $SS-A$  represents an unavailable surface site; inherent in Reaction 2 are the assumptions that each surface site can hold only one gas molecule and that the number of available surface sites are fixed (Atkins and Paula, 2014).





Assuming a system at equilibrium, the rates of the forward and reverse reactions according to the Langmuir model can be equated (Eq. 16) (Eq. 17);  $k_f$  and  $k_r$  denote the rate constants of the forward and reverse reactions, respectively,  $P_A$  represents the partial pressure of the adsorbing molecule,  $N_{ss}$  denotes the number of surface sites and  $\theta$  corresponds to the surface coverage (Atkins and Paula, 2014).

$$Rate_{forward} = k_f P_A (1 - \theta) N_{ss} \quad (Eq. 16)$$

$$Rate_{reverse} = k_r \theta \times N_{ss} \quad (Eq. 17)$$

$$k_f P_A (1 - \theta) = k_r \theta \quad (Eq. 18)$$

Surface coverage ( $\theta$ ) is the ratio of occupied sites to the total number of surface sites, or alternatively, the ratio of total integrated O-H absorbance to the integrated absorbance that corresponds to a monolayer (Eq. 19). Rearrangement of Equation 18 allows us to define surface coverage using (Eq. 21), where  $K$  represents the equilibrium rate constant (Eq. 20), and allows us to define the integrated absorbance of water using Equation 22, where the partial pressure of water is replaced by relative humidity level (RH).

$$\theta = \frac{\#occupied\_sites}{\#total\_sites} = \frac{Abs}{Abs_{mono}} \quad (\text{Eq. 19})$$

$$K = \frac{k_f}{k_r} \quad (\text{Eq. 20})$$

$$\theta = \frac{KP_A}{1 + KP_A} \quad (\text{Eq. 21})$$

$$Abs = Abs_{mono} \left( \frac{K \times RH}{1 + K \times RH} \right) \quad (\text{Eq. 22})$$

The Langmuir model as described Equation 22 does not account for the enthalpy of adsorption of water onto the kaolinite surface and assumes that surface coverage is independent of the thermodynamic properties associated with water adsorption. The Langmuir model also assumes that  $\theta_{max}$  is equal to 1. These assumptions imply that water molecules form a single evenly dispersed layer on the surface of kaolinite. In order to determine whether water adsorption onto kaolinite is modeled by Langmuir adsorption theory, we fitted the Langmuir model (Eq. 22) to our plot of integrated O-H absorbance versus relative humidity level for kaolinite (Figure 43).

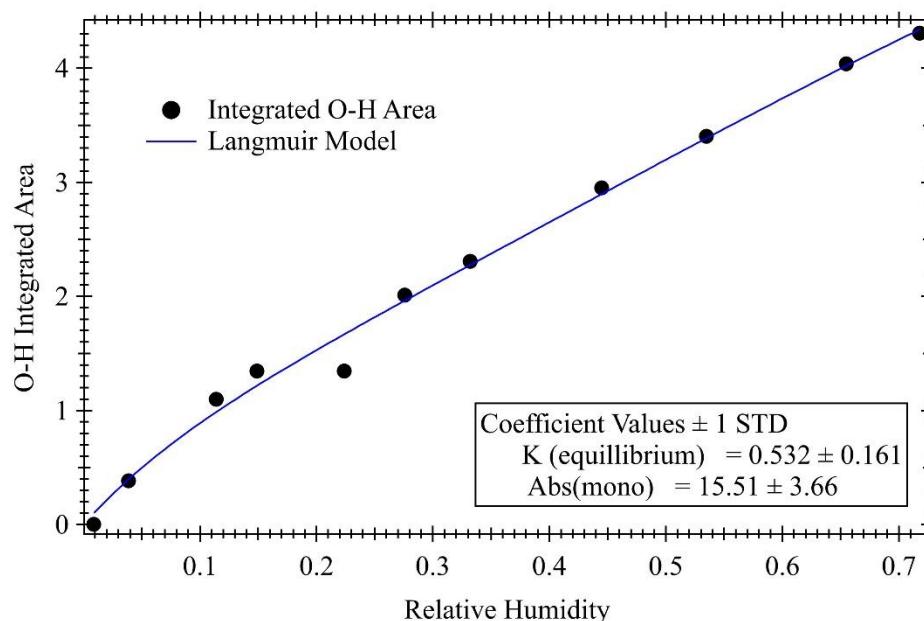


**Figure 43. Langmuir Water Adsorption Isotherm for Kaolinite.** Note: STD denotes standard deviation. Indicates that at a RH = 100 %, surface coverage is 5.29 %. This isotherm is in disagreement with findings that report that at a RH = 100 %, multiple water layers are formed on a solid surface.

While the water isotherm of kaolinite appears to fit Langmuir adsorption theory, the numerical results of the fit suggest otherwise. Using the Langmuir best fit equilibrium rate constant for kaolinite's water isotherm ( $K = 0.532 \pm 0.161$ ) and the absorbance corresponding to a monolayer ( $Abs_{mono} = 15.51 \pm 3.66$ ), at a relative humidity level of 100 %, surface coverage would be merely 5.29 %. Studies show that at a relative humidity of 100 %, multiple layers of water molecules form on a solid inorganic surface (Rubasinghege and Grassian, 2013). Therefore, we observe that Langmuir adsorption theory does not effectively characterize the water isotherm for kaolinite. Langmuir theory treats kaolinite as a homogenous surface; however, when we consider the chemical nature of the kaolinite surface, it is evident that kaolinite has various surface sites that have different chemical properties. Therefore, the favorability of water adsorption to the surface of kaolinite likely varies for different sites on the surface. Additionally, the

Langmuir model is not effective for kaolinite because the simplification that water spontaneously adsorbs directly onto the clay surface irrespective of the relative humidity level is unlikely. Considering the nature of the strong hydrogen-bonding intermolecular interactions that water molecules form with one another, thermodynamic benefits and costs likely dictate whether a molecule of water vapor binds directly onto the clay surface or onto water molecules already adsorbed to the kaolinite surface. Brunauer, Emmett, and Teller (BET) adsorption theory allows us to make these considerations and provides a better model for kaolinite's isotherm.

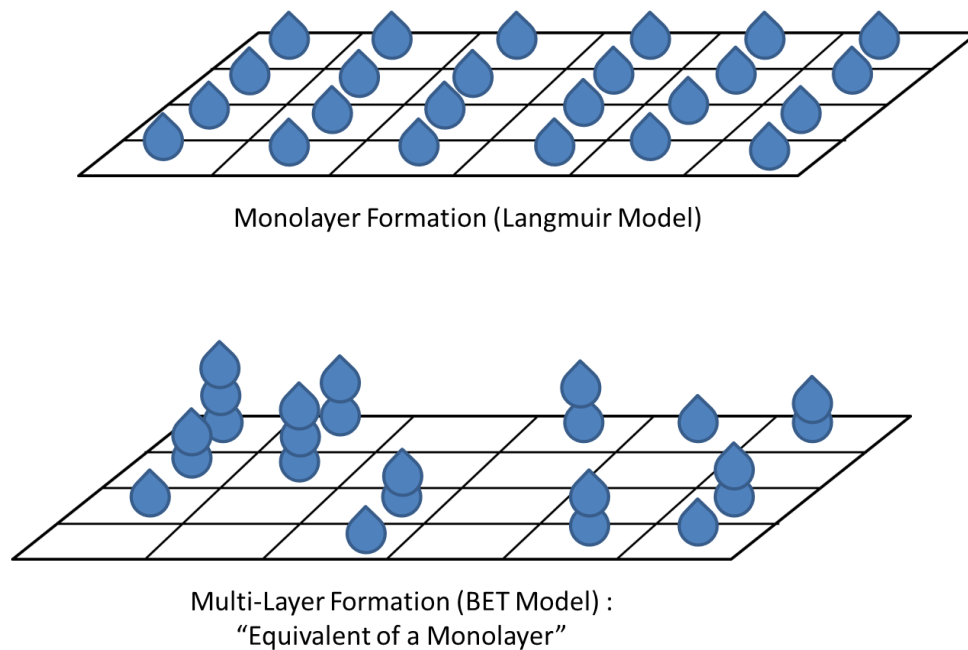


**Figure 44. Langmuir vs. BET Model of Water Adsorption to a Solid Surface.** (a) Langmuir model: assumes that a monolayer is composed of evenly distributed gas molecules on a solid surface (b) BET model: assumes that gas molecules are adsorbed variably onto a solid surface and that an equivalent of a monolayer may include multiple Langmuir-style layers. The surface of kaolinite is heterogeneous; therefore, a BET model is used to study water adsorption onto kaolinite.

Water molecules that adhere to the surface of kaolinite are likely to be adsorbed to the surface in a random fashion that leads to the formation of multiple layers; we can consider that these adsorbed layers of water molecules are in dynamic equilibrium with gaseous water molecules. A Brunauer, Emmett, and Teller (BET) model accounts for preferential adsorption of gas-phase molecules to solid-phase surfaces by assessing the quantity of adsorbed molecules on the solid surface that correspond to a monolayer (Figure 44). The BET model works best for kaolinite because it evaluates the relative humidity level where an *equivalent of a monolayer* exists on the kaolinite surface and does not assume that the molecules are evenly dispersed. BET theory approximates the layers of adsorbed molecules to a given solid surface by assuming a system at equilibrium. The original BET model (cited by Angelini et al., 2007) (Eq. 23) assumed that an infinite number of layers of gas molecules could form on a given solid surface; this model worked well for RH levels up to 30 % but did not work well for higher relative humidity levels.

$$Abs = \frac{Abs_m c RH}{(1 - RH)[1 + (c - 1)RH]} \quad (\text{Eq. 23})$$

In the original BET equation (Eq. 23), *Abs* corresponds to the integrated area of the OH bending mode absorption bands and RH stands for relative humidity. The parameter *Abs<sub>m</sub>* indicates the integrated area corresponding to an equivalent of monolayer of surface adsorbed water. The parameter *c* denotes the binding enthalpy difference between a water molecule that adheres to a solid surface and one that adheres to another water molecule, such as in bulk solvent (Eq. 24) (Figure 45).

(Eq. 24)

$$c = \exp\left(\frac{\Delta H_2^\circ - \Delta H_1^\circ}{RT}\right)$$

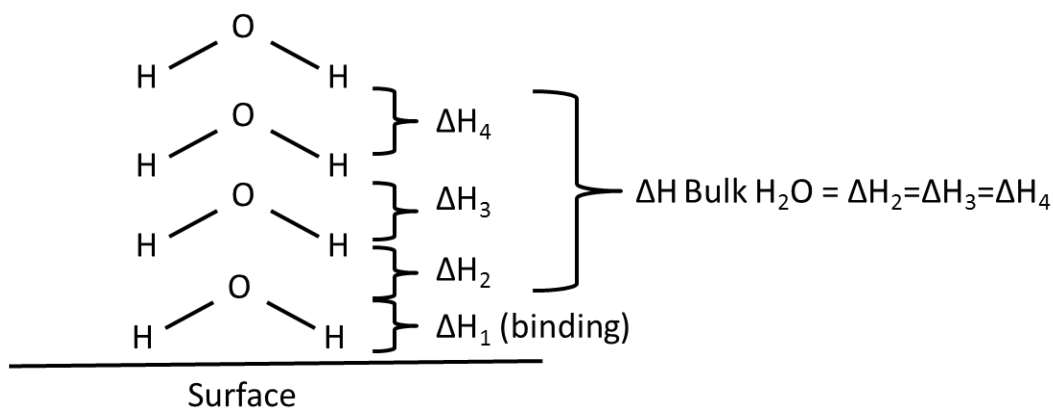


**Figure 45. Schematic of Interactions between Various Layers of Water and a Solid Surface.**  $\Delta H_1$  = binding enthalpy of first water layer and solid surface.  $\Delta H_2$  = binding enthalpy of second layer to first layer. BET assumes that  $\Delta H_2 = \Delta H_3 = \Delta H_4 = \Delta H$  of bulk  $H_2O$ . Therefore, the parameter  $c$  estimates the quotient of ( $\Delta H$  of bulk  $H_2O - \Delta H_1$ ) and ( $RT$ ) (Equation 24).

The parameter  $c$  assumes that the thermodynamic nature of interactions between subsequent layers of water molecules on a surface essentially model the thermodynamic properties of water in bulk solvent. Therefore, with the exception of interactions between the surface and the first layer ( $\Delta H_1^\circ$ ), all interactions between subsequent layers ( $\Delta H_2^\circ$ ) are assumed to be thermodynamically equivalent. Thus,  $\Delta H_2^\circ$  for water molecules in all layers aside from the first layer, have binding enthalpies equivalent to that of bulk water ( $-44.0 \text{ kJ mol}^{-1}$ ) (Woodill et al., 2013). The constants  $R$  and  $T$  denote the gas constant ( $8.31447 \text{ J mol}^{-1} \text{ K}^{-1}$ ) and temperature (K), respectively.

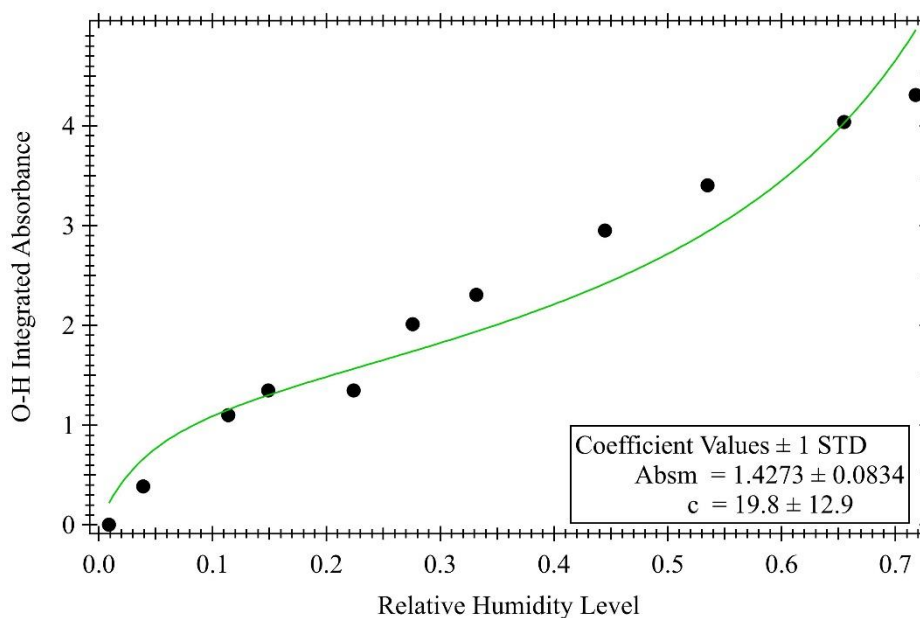


**Figure 46. Original BET Water Adsorption Isotherm for Kaolinite.** Note: STD denotes standard deviation. Indicates that the original BET water adsorption model does not accurately characterize the water isotherm for kaolinite.

Fitting the original BET model (Eq. 23) to our plot of integrated absorbance versus relative humidity level yielded the poor fit illustrated in Figure 46. Thus, we observe that the original BET model does not generate a viable isotherm for kaolinite (Figure 46). It was postulated that gas-phase molecules do not adsorb to solid surfaces to form an infinite number of layers. Therefore, a modified version of the BET model cited by Woodill et al. (Eq. 25) was fitted to the integrated absorbance plot in order to generate a more characteristic water adsorption isotherm for kaolinite (Figure 47) (Woodill et al., 2013). The modified BET theory was used to determine the relative quantity of adsorbed water necessary to form a monolayer on the kaolinite surface. The following equation outlines the modified BET model (Eq. 25) (Woodill et al., 2013).

$$Abs = \frac{Abs_m c RH}{1 - RH} \left( \frac{1 - (n+1)RH^n + nRH^{n+1}}{1 + (c-1)RH - cRH^{n+1}} \right) \quad (\text{Eq. 25})$$

The modified BET equation accounts for the same parameters as the original BET model; however, it includes a coefficient  $n$  which refers to the maximum number of layers that can form on the surface. The modified BET equation was used to generate a curve that best fit the integrated absorbance plot (Figure 47).

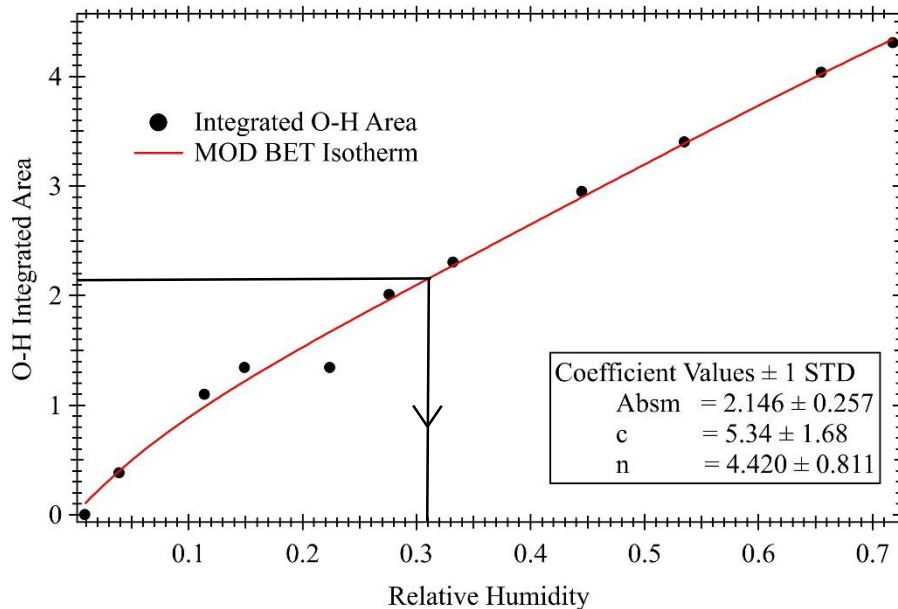


**Figure 47. Water Adsorption Isotherm for Kaolinite.** Indicates that at a relative humidity level = 31 % an equivalent of a monolayer exists on the kaolinite surface.

The following coefficient values were determined to yield the best fit:  $Abs_m = 2.146 \pm 0.257$ ,  $c = 5.34 \pm 1.68$ , and  $n = 4.420 \pm 0.811$ . The  $c$  value of 5.34 indicates that at room temperature ( $T = 22^\circ\text{C}$ ), which is the temperature at which the water adsorption studies were performed, the water-kaolinite surface binding enthalpy is approximately  $-48.1 \text{ kJ mol}^{-1}$ . The binding enthalpy of water to kaolinite ( $-48 \text{ kJ mol}^{-1}$ ) is comparable to the



binding enthalpies determined for NaCl and  $\alpha$ -Al<sub>2</sub>O<sub>3</sub> which were reported to be -50 kJ mol<sup>-1</sup> and -52 kJ mol<sup>-1</sup>, respectively (Woodill et al., 2013). The  $n$  value attained using the modified BET model suggests that the maximum number of layers of water that can form on the surface of kaolinite is about 4.420. According to the modified BET curve in Figure 47, when absorbance was approximately 2.146, the relative humidity was approximately 31 %. Therefore, at a relative humidity of 31 %, there was an equivalent of a monolayer of water on the kaolinite surface. An equivalent of a monolayer, as predicted by BET theory, does not suggest that the surface of kaolinite is evenly covered with water molecules and allows us to consider that water molecules adhere preferentially to sites on the kaolinite surface depending on the favorability of intermolecular interactions. Thus, quantifying the relative humidity at which water forms an equivalent of a monolayer (likely in the form of water droplets) on the kaolinite surface, provides insight into the availability of reactive sites for  $\alpha$ -pinene at any given relative humidity level.

### 4.3. Assessing the Effect of Relative Humidity on Reactivity

Reactions between ( $\alpha$ )-(+)-pinene and kaolinite were performed at a range of relative humidity (RH) levels in order to assess the effect of relative humidity or surface adsorbed water on reactivity. In Figure 48, we consider DRIFTS spectra collected 200 minutes after reactions between  $\alpha$ -pinene and kaolinite began; monitoring changes of the C-H stretching peaks for these reactions reveals that at a given time point during a reaction, the height of the C-H stretching peak is smaller for a reaction performed at a higher RH level than for a reaction at a lower RH humidity level. This indicates that at lower RH levels, higher concentrations of organic product are adsorbed to the kaolinite

surface and that reactivity between ( $\alpha$ )-(+)-pinene and kaolinite is inversely related to the relative humidity level.

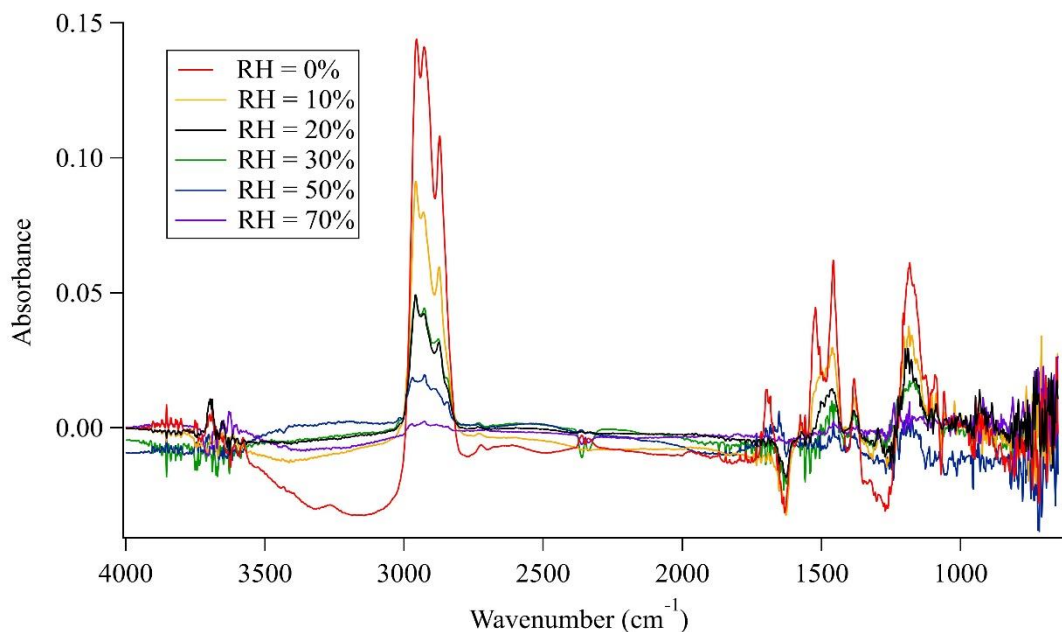


**Figure 48.** *Subtracted Spectra After 200 min of Reaction for Range of RH Levels.* Reveals that reactivity is inversely related to relative humidity level.

The area under the C-H stretching mode peaks can be integrated in order to display the relative concentrations of organic product on the kaolinite surface at given time points for various RH levels (Figure 49). After 25, 50, and 100 minutes of reactivity, the inverse relationship between RH level and product formation observed in the IR spectra at 200 minutes is evident.

The findings of our water adsorption study and BET isotherm reveal that as RH humidity levels rise, water adsorption to the kaolinite surface increases and multiple water layers form. In Figure 49, the water adsorption isotherm for kaolinite is plotted against RH level together with the integrated areas of the C-H absorption bands at various RH levels and time points. Figure 49 displays that water adsorption onto kaolinite

increases with increasing RH level while product formation decreases with increasing RH level.

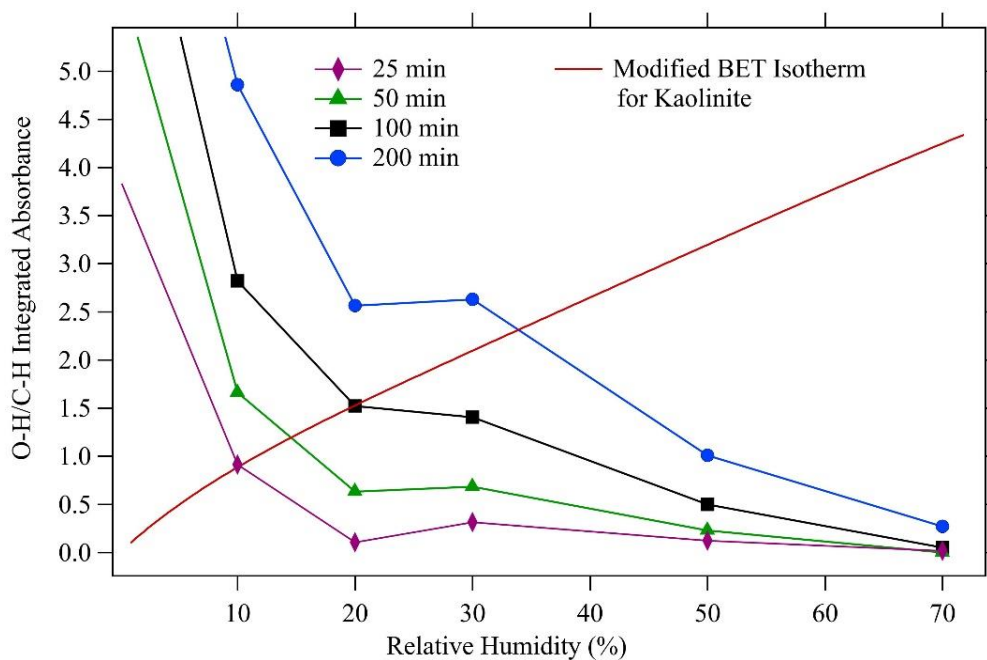


**Figure 49. Integrated Absorbance of C-H Peaks After Various Time Points of Reactivity for Various RH Levels.** Demonstrates that relative concentrations of organic product adsorbed to kaolinite surface decrease and quantity of surface-adsorbed water increases as RH level increases. Reveals that water molecules compete with  $\alpha$ -pinene molecules for surface sites on kaolinite.

This correlation implies that surface adsorbed water inhibits the reactivity of ( $\alpha$ )-(+)-pinene and kaolinite, and suggests that gaseous water and ( $\alpha$ )-(+)-pinene molecules compete for surface sites on kaolinite. This competitive adsorption theory reveals that SOA production from reactions between mineral aerosols and gaseous  $\alpha$ -pinene is more significantly subdued as the quantity of surface-adsorbed water increases. Yet, the observation that reactivity persists between relative humidity levels ranging from 0 – 70 % suggests that at atmospherically relevant conditions within this range, relative humidity does not entirely inhibit reactivity. Also, the fact that reactivity persists above a

relative humidity level of 31 %, where an *equivalent of a monolayer* is formed on the kaolinite surface, reiterates that the water layer is not uniformed and that some surface sites remain unblocked. Therefore, we can conclude that heterogeneous pathways are likely able to generate low volatility organic compounds that can contribute to SOA at atmospherically relevant conditions.

## 5.0. Placing Findings in the Context of Atmospheric Chemistry

### 5.1. Calculating the Net Uptake Coefficient

Having established that  $\alpha$ -pinene can contribute to SOA formation and growth, preliminary studies were performed to characterize the speed at which heterogeneous pathways involving  $\alpha$ -pinene contribute to the formation of SOA atmospherically. In order to assess the speed of SOA formation as a result of the heterogeneous pathways we have observed in this study, we calculated an uptake coefficient ( $\gamma$ ) which allows us to evaluate the net probability that a collision between ( $\alpha$ )-(+)-pinene in the gas-phase and the surface of kaolinite will result in a reaction. In Chapter 3, we proposed that the rate law for reactions between  $\alpha$ -(+)-pinene and kaolinite can be described as an overall second order process where the rate of reaction is proportional to a rate constant  $k$ , the pinene concentration [ $Pin$ ] and the surface site concentration [ $SS$ ] (Eq. 8).

$$Rate = k[Pin][SS] \quad (\text{Eq. 8})$$

Considering that the  $\alpha$ -pinene concentration in this study was held constant at 7 ppm, we re-modeled the above rate law into a pseudo-first order process where the rate of reaction is proportional to the surface site concentration and a new rate constant  $k_{exp}$ , which is the product of  $k$  and [ $Pin$ ].

$$Rate = k_{exp}[SS] \quad (\text{Eq. 9})$$

Using this rate law (Eq. 9) and the data collected at a relative humidity level of 10 %, we derived a relationship for the relative concentration of organic products formed on the

kaolinite surface as a function of time and fitted this relationship to our plot of integrated C-H absorbance vs. time (Eq. 14).

$$[P]_t = A_0(1 - e^{-k_1 t}) + B_0(1 - e^{-k_2 t}) \quad (\text{Eq. 14})$$

$$[P]_t = (1.806)(1 - e^{-(0.011035)t}) + (12.673)(1 - e^{-(0.0013972)t})$$

Our observation that the rate of product formation could be modeled by two rate constants where  $k_1$  is greater in magnitude than  $k_2$ , suggests that there are two distinct processes controlling product formation: one that occurs rapidly, and another that occurs slowly. Hence, the kinetic analysis we have done thus far has allowed us to characterize the manner in which product formation occurs after collisions between  $\alpha$ -(+)-pinene (at 7 ppm) and kaolinite occur. While we have insight into how product formation proceeds once successful collisions happen, it is also important to consider the likelihood that successful collisions will occur, which we can do by calculating a net uptake coefficient.

A laminar flow reactor (LFR) system was used to model heterogeneous reactions between  $\alpha$ -(+)-pinene and kaolinite in order to calculate the net uptake coefficient for this reaction. The LFR set-up (Figure 50) is composed of an outer glass tube and a kaolinite coated inner tube. In order to coat the inner glass tube of the laminar flow reactor (LFR) with kaolinite, slurry of kaolinite clay and deionized water (approx. 3:2 mass ratio, respectively) is prepared by combining the two reagents in a beaker and mixing them thoroughly. Using a brush, the interior of the glass tube is evenly coated with the kaolinite-water slurry.

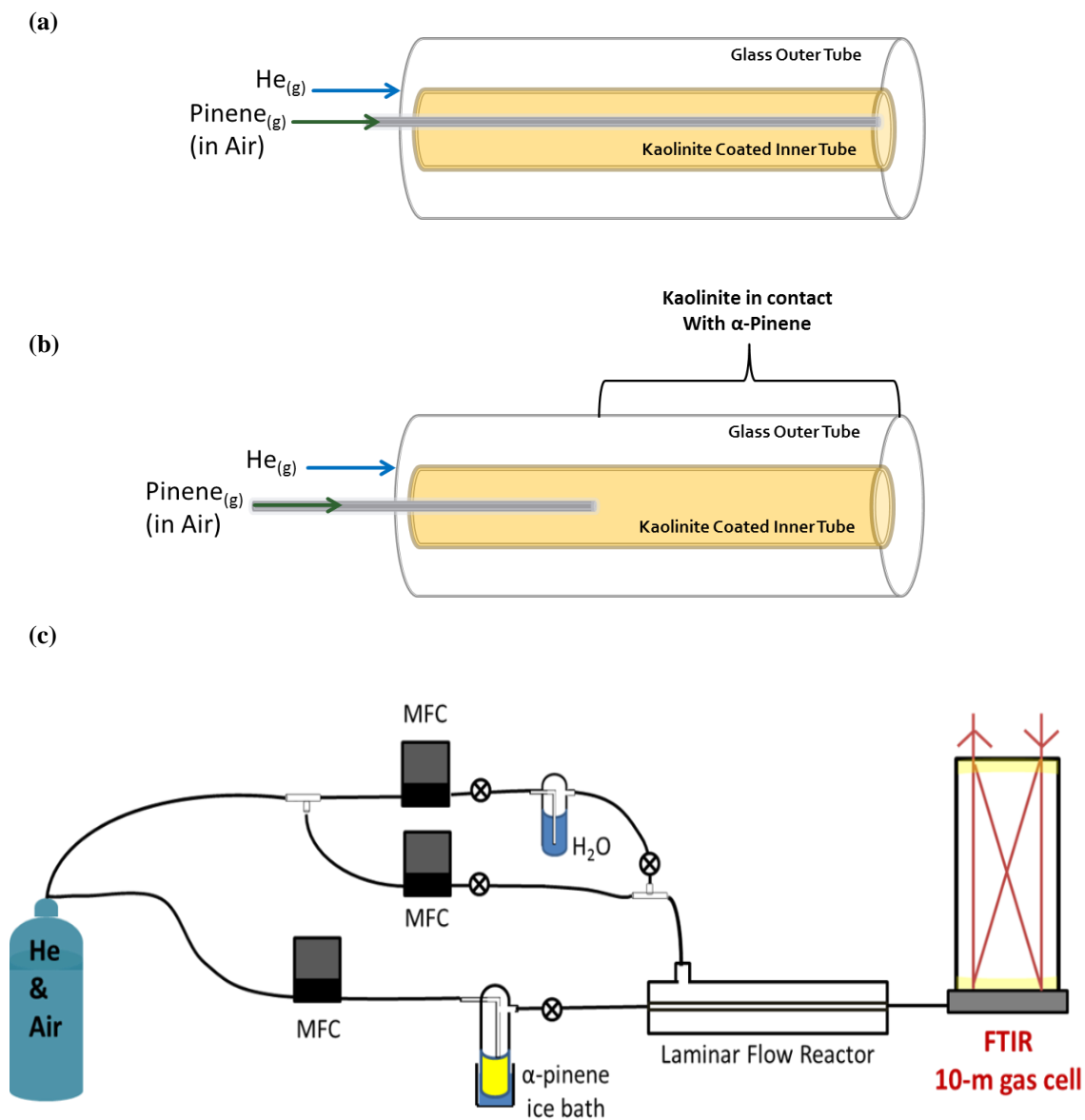


**Figure 50. Schematics of Laminar Flow Reactor.** (a) Rod pushed all the way into the LFR:  $\alpha$ -pinene passing through the metal rod does not collide or react with kaolinite coating (b) Rod pulled out of LFR:  $\alpha$ -pinene passing through metal rod can collide and react with kaolinite coating (c) overall LFR set-up. The Laminar flow reactor allows the transmission of pinene through the LFR to be measured and an uptake coefficient to be calculated.

The coated inner glass tube is placed in the LFR and dried with helium gas. The dried kaolinite coated inner tube is humidified to the desired level using a series of Mass-Flow® controllers. Compressed air is bubbled through a sample of liquid ( $\alpha$ )-(+)-pinene (CAS:

7785-70-8) in a cooling bath composed of NaCl and ice between -4 and -12 °C. While the metal rod is injected into the LFR, gaseous ( $\alpha$ )-(+)-pinene is flowed through the metal rod until the FTIR gas cell records a stable concentration of ( $\alpha$ )-(+)-pinene. The metal injector rod is then retracted for 10 minutes in order to allow gaseous ( $\alpha$ )-(+)-pinene to react with kaolinite clay in the inner glass tube. The process of injecting the metal rod until ( $\alpha$ )-(+)-pinene is at a stable concentration and retracting the metal rod for 10 minutes, is repeated in order to attain a set of data.

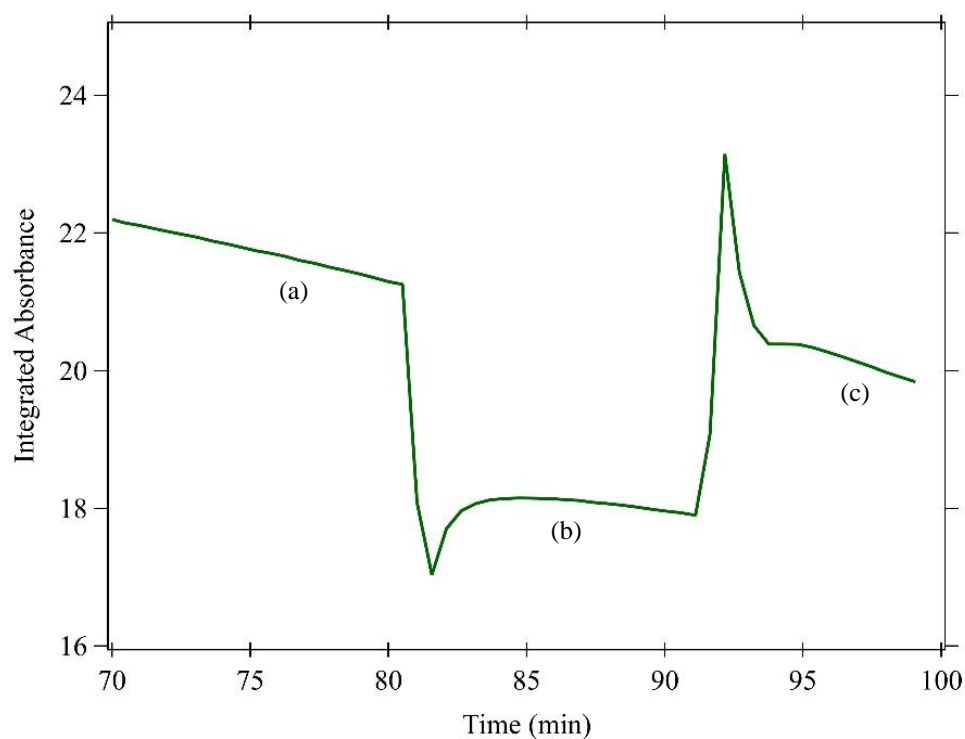


**Figure 51. Raw Laminar Flow Reactor Data Collected for Reactions at RH = 25 %.** (a) Injector rod is pushed into LFR (b) injector rod is pulled out of LFR (c) injector rod is pushed back into LFR. Regions (a) and (c) allow us to measure the initial pinene concentration; the initial  $\alpha$ -pinene concentration noticeably varies with time.

The FTIR gas cell collects spectra of the  $\alpha$ -pinene content that makes it through the LFR and reaches the gas cell; therefore, the collected spectra correlate to the content of  $\alpha$ -pinene that does not react with the kaolinite surface or the transmitted  $\alpha$ -pinene



concentration. Integration of the C-H stretching peaks over time provides the relative concentrations of transmitted  $\alpha$ -pinene throughout the experiment. A plot of the raw data collected at a relative humidity level of 25 % is displayed in Figure 51. The y-axis corresponds to the integrated C-H absorbance bands of  $\alpha$ -pinene while the x-axis is in units of time (min). In region (b) of the plot, the rod is pulled out of the LFR (Figure 50 (b)) in order to allow  $\alpha$ -pinene to react with the inner coated surface. In order to measure the relative concentration of  $\alpha$ -pinene that is lost as a result of reactions with kaolinite (which we will use later to calculate the uptake coefficient), it is necessary for us to have an accurate measurement of the initial pinene concentration.

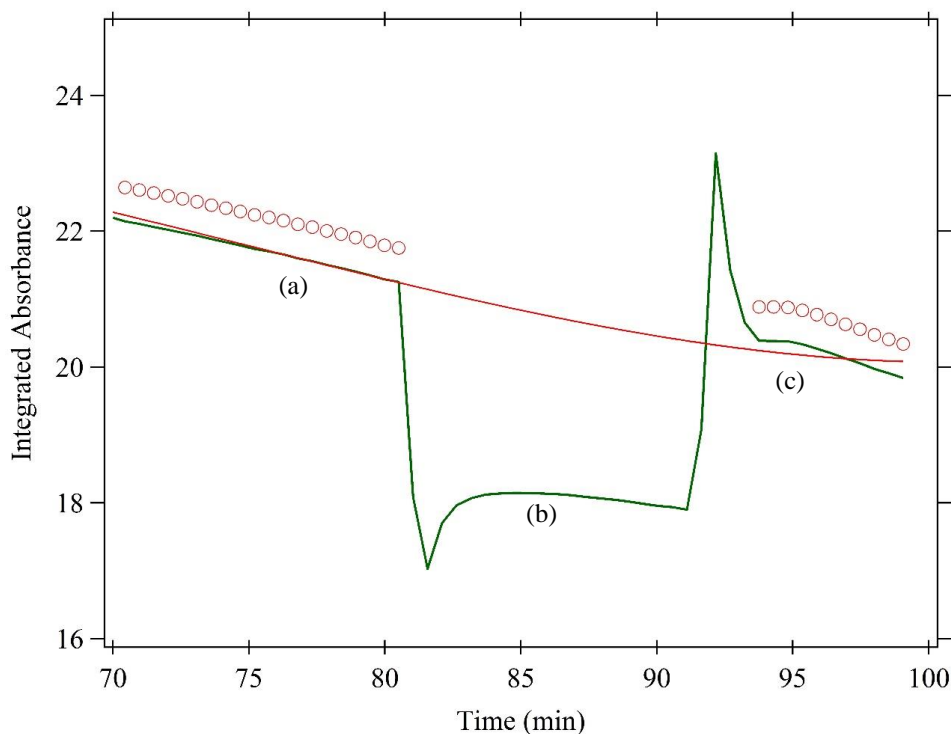


**Figure 52. Polynomial Fit of Initial  $\alpha$ -Pinene Concentration for LFR Study.** (a) Injector rod is pushed into LFR (b) injector rod is pulled out of LFR (c) injector rod is pushed back into LFR. Displays the polynomial fit for regions (a) and (c); fitting the initial  $\alpha$ -pinene concentration to a polynomial allows us to characterize it as a function of time. Note: fit is illustrated by the red line and circular markers highlight regions (a) and (c).

Due to the fact that the initial  $\alpha$ -pinene concentration varies with time, we fit regions (a) and (c) to a higher order polynomial function (illustrated by the red line in Figure 52) in order to more accurately determine the initial  $\alpha$ -pinene concentration. Equation 26 outlines the higher order polynomial function that best fit our measurement of the initial  $\alpha$ -pinene concentration.

$$[Pin]_0 = (8.0487) + (0.74904)t - (0.011316)t^2 + (5.0278e^{-5})t^3 \quad (\text{Eq. 26})$$

The quotient of the integrated areas for the time points where kaolinite is in contact with pinene (region (b)) and the integrated areas when pinene is not in contact with kaolinite (now modeled by our higher order polynomial function) is calculated over the duration of the reaction in order to generate a transmission wave (Equation 27) (Figure 53).

$$\text{Transmission} = \frac{[Pin]}{[Pin]_0} \quad (\text{Eq. 27})$$

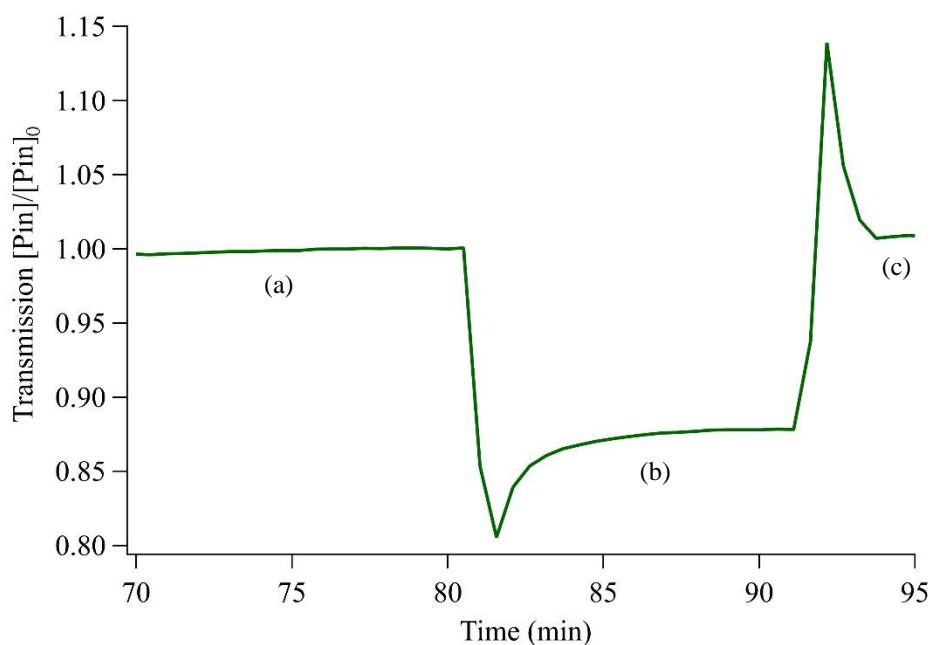


**Figure 53.** *Transmission Wave for Reaction Performed at a RH of 25 %.* (a) Injector rod is pushed into LFR (b) injector rod is pulled out of LFR (c) injector rod is pushed back into LFR. Transmission for regions (a) and (c) are near 1 and transmission of (b) is below 1.

Region (a) of the transmission wave presented for the reaction of ( $\alpha$ )-(+)-pinene and kaolinite at a RH = 25% indicates the transmission when the metal injector rod of the LFR is pushed all the way in. In region (a), the concentration of pinene initially introduced into the LFR ( $[Pin]_0$ ) is equivalent to the concentration of pinene transmitted through the LFR ( $[Pin]$ ); therefore, transmission for this region is essentially 1. In region (b) the injector rod is pulled out of the LFR so pinene reacts with the kaolinite surface such that  $[Pin]_0 \neq [Pin]$  and transmission is below one. In region (c) the injector is pushed into the LFR so that pinene can no longer react with the kaolinite surface which allows transmission to return to 1. Equation 28 defines how the uptake coefficient of  $\alpha$ -pinene on kaolinite ( $\gamma_{eff, pin}$ ) is calculated using the LFR set-up (Knopf et al., 2015).

$$\gamma_{eff, pin} = \frac{D_{tube}}{\omega_{pin} \times t} \ln \left[ \frac{[Pin]_0}{[Pin]} \right] \quad (\text{Eq. 28})$$

In the calculation of the  $\gamma_{eff, pin}$ ,  $D_{tube}$  (cm) refers to the diameter of the laminar flow reactor tube,  $\omega_{pin}$  (cm/s) refers to the thermal molecular velocity of pinene, and  $t$  (s) denotes the time of interaction between ( $\alpha$ )-(+)-pinene and kaolinite. The quotient of  $D_{tube}$  and  $\omega_{pin} \times t$  is multiplied by the natural log of the inverse of the transmission of pinene through the reactor in order to calculate  $\gamma_{eff, pin}$ . The transmission in region (b) for a full data set is used to calculate the uptake coefficient using Equation 28 ( $D_{tube} = 2.54$  cm,  $\omega_{pin} = 21525$  cm/s,  $t = 9.032$  s) (Figure 54).

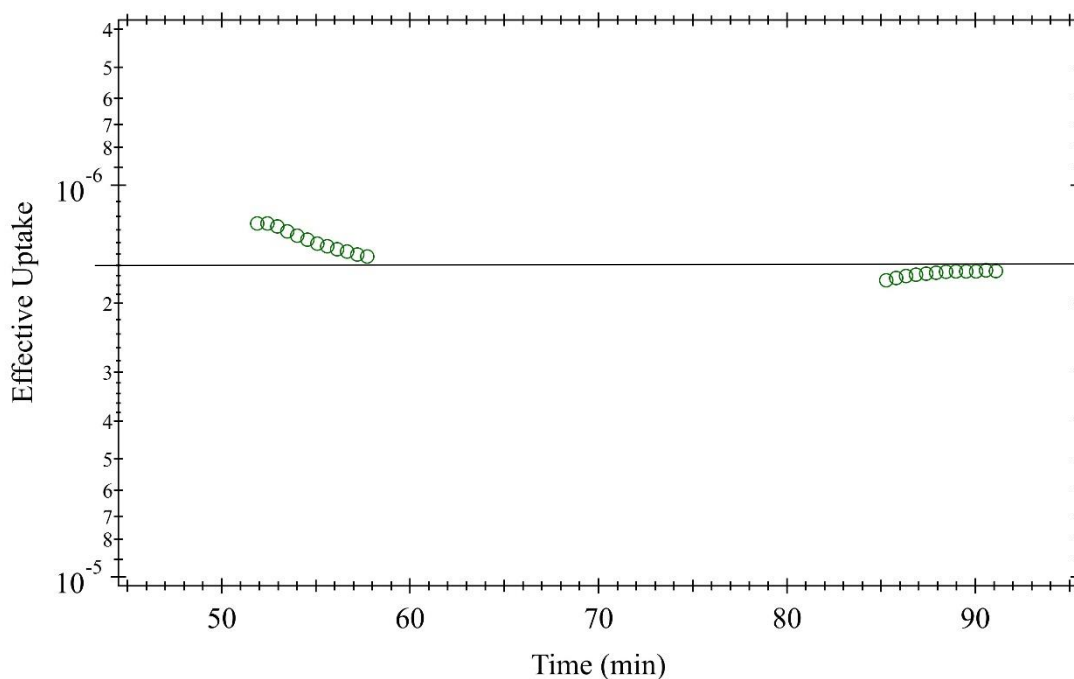


**Figure 54.** Plot of *Effective Uptake vs. Time at RH = 25 %*. Note: this plot represents two experimental runs. The average effective uptake of these two runs is  $1.6 \times 10^{-6}$ . This value indicates that every 1.6 in a million collisions between  $\alpha$ -pinene will lead to a reaction.

Using Figure 54, which represents two experimental runs, the estimated value for  $\gamma_{eff, pin}$  using these parameters is  $1.6 \times 10^{-6}$  which estimates that 1.6 in 1 million collisions between ( $\alpha$ )-(+)-pinene and kaolinite will lead to a reaction. For comparison, the uptake coefficient of limonene on kaolinite was determined to be  $9.7 \times 10^{-7}$ . Hence, limonene uptake on kaolinite is about 40 % less than  $\alpha$ -pinene uptake which suggests that reactivity between  $\alpha$ -pinene and kaolinite is more likely to lead to the formation of surface adsorbed lower volatility organics. It is important to note that for the uptake coefficient calculation presented for  $\alpha$ -pinene in this study, parameters such as  $D_{tube}$ ,  $\omega_{pin}$ , and  $t$  were taken from the LFR studies involving limonene and mineral dust; hence, the  $\gamma_{eff, pin}$  value is simply an approximation. Future studies of heterogeneous reactions involving  $\alpha$ -pinene and kaolinite should repeat this experimental procedure and calculation using values that pertain exclusively to  $\alpha$ -pinene in order to attain a more characteristic estimate of the

uptake of  $\alpha$ -pinene on kaolinite. Using the uptake coefficient, further calculations can be made to determine the atmospheric lifetime of the products of this reaction. This will allow comparisons to be made between heterogeneous and gas-phase pathways for the formation of SOA.

## 5.2. Discussion

Secondary organic aerosols are a class of atmospheric particulates that impact human health, climate and atmospheric chemistry. While ample research has been conducted to outline the formation of SOA from the gas-phase oxidation of volatile organic compounds, computational models of SOA suggest a missing SOA source. Since mineral dust particles are emitted in large quantities into the atmosphere, the question of whether heterogeneous reactions involving mineral aerosols and VOC can promote SOA has been a primary investigation in the Hinrichs lab. While reactions between limonene and mineral dust have been observed to produce lower volatility SOA components, questions remain concerning whether  $\alpha$ -pinene, which is a more abundant VOC relative to limonene, can promote SOA at atmospherically relevant conditions. Infrared spectroscopy (DRIFTS) was used to model and assess heterogeneous reactions between  $\alpha$ -pinene and kaolinite, which is a major clay component of mineral dust particles. GC-MS analyses verified that reactions between ( $\alpha$ )-(+)-pinene and kaolinite clay produced the following major low volatility organic products:  $\alpha$ -terpineol, high molecular weight dimers, endo borneol, and fenchol. The monomer products are viable components of secondary organic aerosols because they possess alcohol groups, which result in vapor pressure reductions on the order of  $10^{-3}$ . These monomer products are hypothesized to be formed via acid catalyzed hydration mechanisms. Our hypothesized mechanism for  $\alpha$ -

terpineol formation parallels the acid catalyzed synthesis of terpineol from  $\alpha$ -pinene observed and outlined by Román-Aguirre et al. (Román-Aguirre et al., 2005). Román-Aguirre et al. performed the synthesis of terpineol in the solution phase at 70 °C using chloroacetic acid and deionized water and used GC-MS to analyze their products. Román-Aguirre et al. proposed that in the synthesis of terpineol from  $\alpha$ -pinene, water served as an alcohol group donor and chloroacetic acid catalyzed the reaction. In the heterogeneous formation of the observed monomer products, we propose that acidic sites on the kaolinite clay (likely both the Lewis and Bronsted-Lowry acid sites) serve as catalysts for the formation of the lower volatility monomer SOA components.

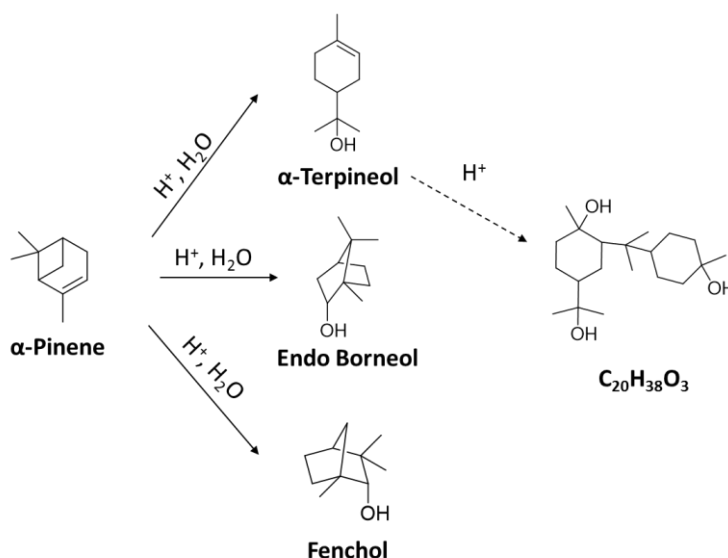


**Figure 55. Organic Monomer and Dimer Products of Reactions between  $\alpha$ -Pinene and Kaolinite.** Major products formed as a result of heterogeneous reactions between  $\alpha$ -pinene and kaolinite.

Heterogeneous reactions between ( $\alpha$ )-(+)-pinene and kaolinite produce high molecular weight dimers that have not been fully characterized. While significant MS fragmentation inhibited us from determining the exact molecular weights of the dimers produced, analyses of the fragmentation patterns enabled us to propose  $C_{20}H_{38}O_3$  as a viable possible structure of the dimer compounds. While our proposed dimer structure

(326 amu) is not as large as those reported by Cheshchevoi et al. (> 500 amu), who performed reactions between  $\alpha$ -pinene and kaolinite under dry conditions, our proposed structure suggests that at atmospherically relevant conditions, dimers may be more than twice the size of individual pinene or monomer compounds.

In Chapter 1, we considered how the relatively small sizes of aerosols allow them to harm human respiratory, circulatory and neurological health. We also considered how aerosols can impact atmospheric heating and cooling cycles by scattering or absorbing solar radiation, and their ability to react with trace gases in the atmosphere. In order to thoroughly characterize the health, climate and atmospheric chemistry impacts of aerosols, it is essential to understand their chemistry and to know their structures; these were the primary objectives of our study of heterogeneously generated SOA. Therefore, knowing the structures and formation pathways of the high molecular weight dimer products, which likely constitute a significant portion of SOA mass, is crucial in order to understand the larger implications that heterogeneously derived dimers can have. Aside from the significant London dispersion interactions that dimers can experience, the presence of a single polar group (i.e. OH group) in the dimers could imply substantial reductions in their vapor pressure as a result of dipole-dipole interactions as well. The production of oxygenated dimers would suggest that interactions between VOC and mineral aerosols atmospherically, can result in prolonged chemical changes to mineral aerosol surfaces which will characterize their impact on human health, climate and atmospheric chemistry. Therefore, it is highly recommended that experiments between  $\alpha$ -pinene and kaolinite be replicated using softer ionization techniques in order to identify a molecular ion and structure.

Characterizing the effect of RH on heterogeneous SOA formation pathways is necessary to verify that these pathways can occur under atmospherically relevant conditions. In a study of gas-phase SOA formation pathways, the effect of RH on reactions between  $\alpha$ -pinene and ozone was found by Cocker III et al. to be insignificant (2001). Yet, the heterogeneous reactions of ( $\alpha$ )-(+)-pinene and kaolinite performed in this study demonstrate an inverse relationship between reactivity and RH level as a result of competition between  $\alpha$ -pinene and water molecules for surface sites on the kaolinite clay. The ability of water vapor to reduce reactivity implies that heterogeneously derived contributions to the atmospheric SOA budget are likely less significant than contributions from gas-phase pathways. Using BET theory, we estimated that the *equivalent of a monolayer* is formed on the surface of kaolinite at a relative humidity level of 31 %. Hence, the fact that reactivity occurs above a RH level of 31% between ( $\alpha$ )-(+)-pinene and kaolinite suggests that heterogeneous SOA formation pathways can be considered atmospherically relevant.

The likelihood that reactions between  $\alpha$ -pinene and mineral aerosols in the atmosphere will occur is characterized by the probability that  $\alpha$ -pinene molecules will successfully collide surface reactive sites. The mechanism for these collisions may follow an Eley-Rideal model where organic adsorption onto the surface occurs only after  $\alpha$ -pinene successfully collides and reacts at a viable surface site. Alternatively,  $\alpha$ -pinene may initially become adsorbed to a reactive surface where it subsequently reacts with surface adsorbed water; this mechanistic model is referred to as the Langmuir-Hinshelwood model. Using density functional theory (DFT) computations, Chase et al. observed that adsorption of  $\alpha$ -pinene to quartz ( $\text{SiO}_2$ ) was 40 to 60 % irreversible which



indicates that  $\alpha$ -pinene may be considerably sticky (2017). Therefore, these findings suggest that the Langmuir-Hinshelwood mechanistic model may best characterize heterogeneous reactions involving  $\alpha$ -pinene. No experiments were performed in this study to determine the mechanistic model of reactions between  $\alpha$ -pinene and kaolinite; hence, this may be a viable investigation for future studies. We can quantify the probability that collisions between  $\alpha$ -pinene and kaolinite lead to a reaction by calculating the net uptake coefficient. Preliminary calculations at RH = 25 % estimate  $\gamma_{\text{eff, pin}}$  to be  $1.6 \times 10^{-6}$ , which indicates that in every 1 million collisions between ( $\alpha$ )-(+)-pinene and kaolinite, 1.6 of these collisions will result in a reaction. The next step of this analysis requires a calculation of the atmospheric lifetime of the reaction products in order to compare the heterogeneous pathway modeled in this study to gas-phase pathways.

In this study, we have considerably characterized the ability of reactions between  $\alpha$ -pinene and kaolinite to promote SOA, which impact human health, climate and atmospheric chemistry. However, it is important to note that atmospherically, heterogeneous reactivity does not occur exclusively between  $\alpha$ -pinene and kaolinite. In Chapter 1, we considered that mineral dust particles are diverse combinations of metal oxides and aluminum silicates and that the abundances of these various components differ with source location. Therefore, the chemical nature of mineral dust particles is quite complex since reactive sites may vary perhaps considerably as a function of source location. Therefore, in this study we have simply taken a microscopic-like view into the complicated reality of heterogeneously formed secondary organic aerosols from  $\alpha$ -pinene precursor molecules.

## Bibliography

1. Angelini, M. M.; Garrard, R. J.; Rosen, S. J.; Hinrichs, R. Z., Heterogeneous Reactions of Gaseous HNO<sub>3</sub> and NO<sub>2</sub> on the Clay Minerals Kaolinite and Pyrophyllite. *The Journal of Physical Chemistry A* **2007**, *111* (17), 3326-3335.
2. Atkins, P.; Paula, J., Adsorption and Desorption. In *Atkins' Physical Chemistry*, 10 ed.; Oxford University Press: 2014; pp 946-954.
3. Baltensperger, U.; Dommen, J.; Alfarra, M. R.; Duplissy, J.; Gaeggeler, K.; Metzger, A.; Facchini, M. C.; Decesari, S.; Finessi, E.; Reinnig, C.; Schott, M.; Warnke, J.; Hoffmann, T.; Klatzer, B.; Puxbaum, H.; Geiser, M.; Savi, M.; Lang, D.; Kalberer, M.; Geiser, T., Combined Determination of the Chemical Composition and of Health Effects of Secondary Organic Aerosols The POLYSOA Project. *Journal of Aerosol Medicine and Pulmonary Drug Delivery* **2008**, *21* (1), 145-54.
4. Bougeard, D.; Smirnov, K. S.; Geidel, E., Vibrational Spectra and Structure of Kaolinite: A Computer Simulation Study. *The Journal of Physical Chemistry B* **2000**, *104* (39), 9210-9217.
5. Capouet, M.; Peeters, J.; Nozière, B.; Müller, J. F., Alpha-pinene oxidation by OH: simulations of laboratory experiments. *Atmos. Chem. Phys.* **2004**, *4* (9/10), 2285-2311.
6. Chase, H. M.; Ho, J.; Upshur, M. A.; Thomson, R. J.; Batista, V. S.; Geiger, F. M., Unanticipated Stickiness of  $\alpha$ -Pinene. *The Journal of Physical Chemistry A* **2017**.
7. Cheshchevoi, V. N.; Palamarev, D. N.; Diner, V. A.; Polushkin, V. A., Spectral Study of the Oligomerization Products of  $\alpha$ -Pinene on Kaolinite. *Polymer Science U.S.S.R.* **1989**, *31* (10), 2274-2279.
8. Cocker III, D. R.; Clegg, S. L.; Flagan, R. C.; Seinfeld, J. H., The Effect of Water on Gas-Particle Partitioning of Secondary Organic Aerosol. Part I:  $\alpha$ -Pinene/Ozone system. *Atmospheric Environment* **2001**, *35* (35), 6049-6072.
9. Duporté, G.; Flaud, P. M.; Geneste, E.; Augagneur, S.; Pangui, E.; Lamkaddam, H.; Gratien, A.; Doussin, J. F.; Budzinski, H.; Villenave, E.; Perraudin, E., Experimental Study of the Formation of Organosulfates from  $\alpha$ -Pinene Oxidation. Part I: Product Identification, Formation Mechanisms and Effect of Relative Humidity. *The Journal of Physical Chemistry A* **2016**, *120* (40), 7909-7923.
10. Ehn, M.; Thornton, J. A.; Kleist, E.; Sipila, M.; Junninen, H.; Pullinen, I.; Springer, M.; Rubach, F.; Tillmann, R.; Lee, B.; Lopez-Hilfiker, F.; Andres, S.; Acir, I.-H.; Rissanen, M.; Jokinen, T.; Schobesberger, S.; Kangasluoma, J.; Kontkanen, J.; Nieminen, T.; Kurten, T.; Nielsen, L. B.; Jorgensen, S.; Kjaergaard, H. G.; Canagaratna, M.; Maso, M. D.; Berndt, T.; Petaja, T.; Wahner, A.; Kerminen, V.-M.; Kulmala, M.;

- Worsnop, D. R.; Wildt, J.; Mentel, T. F., A large source of low-volatility secondary organic aerosol. *Nature* **2014**, *506* (7489), 476-479.
11. Gradoń, L.; Orlicki, D.; Podgórski, A., Deposition and Retention of Ultrafine Aerosol Particles in the Human Respiratory System. Normal and Pathological Cases. *International Journal of Occupational Safety and Ergonomics* **2000**, *6* (2), 189-207.
12. Hallquist, M.; Wenger, J. C.; Baltensperger, U.; Rudich, Y.; Simpson, D.; Claeys, M.; Dommen, J.; Donahue, N. M.; George, C.; Goldstein, A. H.; Hamilton, J. F.; Herrmann, H.; Hoffmann, T.; Iinuma, Y.; Jang, M.; Jenkin, M. E.; Jimenez, J. L.; Kiendler-Scharr, A.; Maenhaut, W.; McFiggans, G.; Mentel, T. F.; Monod, A.; Prévôt, A. S. H.; Seinfeld, J. H.; Surratt, J. D.; Szmigielski, R.; Wildt, J., The Formation, Properties and Impact of Secondary Organic Aerosol: Current and Emerging Issues. *Atmos. Chem. Phys.* **2009**, *9* (14), 5155-5236.
13. Harris, D., Mass Spectrometry. In *Quantitative Chemical Analysis*, W.H. Freeman and Company: New York, NY, 2010; pp 502-512.
14. Iinuma, Y.; Müller, C.; Böge, O.; Gnauk, T.; Herrmann, H., The formation of organic sulfate esters in the limonene ozonolysis secondary organic aerosol (SOA) under acidic conditions. *Atmospheric Environment* **2007**, *41* (27), 5571-5583.
15. Jang, M.; Kamens, R. M., Newly characterized products and composition of secondary aerosols from the reaction of  $\alpha$ -pinene with ozone. *Atmospheric Environment* **1999**, *33* (3), 459-474.
16. Knopf, D. A.; Pöschl, U.; Shiraiwa, M., Radial Diffusion and Penetration of Gas Molecules and Aerosol Particles through Laminar Flow Reactors, Denuders, and Sampling Tubes. *Analytical Chemistry* **2015**, *87* (7), 3746-3754.
17. Kristensen, K.; Watne, Å. K.; Hammes, J.; Lutz, A.; Petäjä, T.; Hallquist, M.; Bilde, M.; Glasius, M., High-Molecular Weight Dimer Esters Are Major Products in Aerosols from  $\alpha$ -Pinene Ozonolysis and the Boreal Forest. *Environmental Science & Technology Letters* **2016**, *3* (8), 280-285.
18. Kroll, J. H.; Seinfeld, J. H., Chemistry of secondary organic aerosol: Formation and evolution of low-volatility organics in the atmosphere. *Atmospheric Environment* **2008**, *42* (16), 3593-3624.
19. Laaksonen, A.; Kulmala, M.; O'Dowd, C. D.; Joutsensaari, J.; Vaattovaara, P.; Mikkonen, S.; Lehtinen, K. E. J.; Sogacheva, L.; Dal Maso, M.; Aalto, P.; Petäjä, T.; Sogachev, A.; Yoon, Y. J.; Lihavainen, H.; Nilsson, D.; Facchini, M. C.; Cavalli, F.; Fuzzi, S.; Hoffmann, T.; Arnold, F.; Hanke, M.; Sellegri, K.; Umann, B.; Junkermann, W.; Coe, H.; Allan, J. D.; Alfarra, M. R.; Worsnop, D. R.; Riekkola, M. L.;

- Hyötyläinen, T.; Viisanen, Y., The role of VOC oxidation products in continental new particle formation. *Atmos. Chem. Phys.* **2008**, 8 (10), 2657-2665.
20. Lederer, M. R. A Mechanistic and Kinetic Comparison of the Reactivity of Volatile Organic Compounds on Mineral Dusts. Drew University, Madison, NJ, 2016.
21. Lederer, M. R.; Staniec, A. R.; Coates Fuentes, Z. L.; Van Ry, D. A.; Hinrichs, R. Z., Heterogeneous Reactions of Limonene on Mineral Dust: Impacts of Adsorbed Water and Nitric Acid. *The Journal of Physical Chemistry A* **2016**, 120 (48), 9545-9556.
22. Liu, X.; Lu, X.; Sprik, M.; Cheng, J.; Meijer, E. J.; Wang, R., Acidity of edge surface sites of montmorillonite and kaolinite. *Geochimica et Cosmochimica Acta* **2013**, 117, 180-190.
23. Loreto, F.; Ciccioli, P.; Cecinato, A.; Brancaleoni, E.; Frattoni, M.; Tricoli, D., Influence of Environmental Factors and Air Composition on the Emission of [ $\alpha$ ]-Pinene from *Quercus ilex* Leaves. *Plant Physiology* **1996**, 110 (1), 267-275.
24. Observatory, N. E., Dust Over the Red Sea. <http://earthobservatory.nasa.gov>, June 15, 2016.
25. N.I.S.T.,  $\alpha$ -Terpineol: Mass Spectrum. United States of America, 2014.
26. N.I.S.T., Endo Borneol: Mass Spectrum. United States of America, 2014.
27. N.I.S.T., Fenchol: Mass Spectrum. United States of America, 2014.
28. Pandis, S. N.; Harley, R. A.; Cass, G. R.; Seinfeld, J. H., Secondary organic aerosol formation and transport. *Atmospheric Environment. Part A. General Topics* **1992**, 26 (13), 2269-2282.
29. Perraud, V.; Bruns, E. A.; Ezell, M. J.; Johnson, S. N.; Greaves, J.; Finlayson-Pitts, B. J., Identification of Organic Nitrates in the NO<sub>3</sub> Radical Initiated Oxidation of  $\alpha$ -Pinene by Atmospheric Pressure Chemical Ionization Mass Spectrometry. *Environmental Science & Technology* **2010**, 44 (15), 5887-5893.
30. Peters, A.; Veronesi, B.; Calderón-Garcidueñas, L.; Gehr, P.; Chen, L. C.; Geiser, M.; Reed, W.; Rothen-Rutishauser, B.; Schürch, S.; Schulz, H., Translocation and potential neurological effects of fine and ultrafine particles a critical update. *Particle and Fibre Toxicology* **2006**, 3 (1), 13.
31. Pinder, R. W.; Bettez, N. D.; Bonan, G. B.; Greaver, T. L.; Wieder, W. R.; Schlesinger, W. H.; Davidson, E. A., Impacts of human alteration of the nitrogen cycle in the US on radiative forcing. *Biogeochemistry* **2013**, 114, 25-40.

32. Rindelaub, J. D.; Wiley, J. S.; Cooper, B. R.; Shepson, P. B., Chemical characterization of  $\alpha$ -pinene secondary organic aerosol constituents using gas chromatography, liquid chromatography, and paper spray-based mass spectrometry techniques. *Rapid Communications in Mass Spectrometry* **2016**, *30* (13), 1627-1638.
33. Román-Aguirre, M.; Torre-Sáenz, L. D. I.; Flores, W. A.; Robau-Sánchez, A.; Elguézabal, A. A., Synthesis of Terpineol from  $\alpha$ -Pinene by Homogeneous Acid Catalysis. *Catalysis Today* **2005**, *107–108*, 310-314.
34. Romanías, M. N.; Ourrad, H.; Thévenet, F.; Riffault, V., Investigating the Heterogeneous Interaction of VOCs with Natural Atmospheric Particles: Adsorption of Limonene and Toluene on Saharan Mineral Dusts. *The Journal of Physical Chemistry A* **2016**, *120* (8), 1197-1212.
35. Rubasinghege, G.; Grassian, V. H., Role(s) of adsorbed water in the surface chemistry of environmental interfaces. *Chemical Communications* **2013**, *49* (30), 3071-3094.
36. Sakulyanontvittaya, T.; Duhl, T.; Wiedinmyer, C.; Helmig, D.; Matsunaga, S.; Potosnak, M.; Milford, J.; Guenther, A., Monoterpene and Sesquiterpene Emission Estimates for the United States. *Environmental Science & Technology* **2008**, *42* (5), 1623-1629.
37. Sharpe, S. W.; Johnson, T. J.; Sams, R. L.; Chu, P. M.; Rhoderick, G. C.; Johnson, P. A., Gas-Phase Databases for Quantitative Infrared Spectroscopy. *Applied Spectroscopy* **2004**, *58* (12), 1452-1461.
38. Usher, C. R.; Michel, A. E.; Grassian, V. H., Reactions on Mineral Dust. *Chemical Reviews* **2003**, *103* (12), 4883-4940.
39. Woodill, L. A.; O'Neill, E. M.; Hinrichs, R. Z., Impacts of Surface Adsorbed Catechol on Tropospheric Aerosol Surrogates: Heterogeneous Ozonolysis and Its Effects on Water Uptake. *The Journal of Physical Chemistry A* **2013**, *117* (27), 5620-5631.
40. Yokouchi, Y.; Ambe, Y., Factors Affecting the Emission of Monoterpenes from Red Pine (*Pinus densiflora*). *Plant Physiology* **1984**, *75* (4), 1009-1012.
41. Zhang, X.; McVay, R. C.; Huang, D. D.; Dalleska, N. F.; Aumont, B.; Flagan, R. C.; Seinfeld, J. H., Formation and Evolution of Molecular Products in  $\alpha$ -Pinene Secondary Organic Aerosol. *Proceedings of the National Academy of Sciences* **2015**, *112* (46), 14168-14173.
42. Zhao, B.; Wang, S. X.; Liu, H.; Xu, J. Y.; Fu, K.; Klimont, Z.; Hao, J. M.; He, K. B.; Cofala, J.; Amann, M., NO<sub>x</sub> emissions in China: historical trends and future perspectives. *Atmos. Chem. Phys.* **2013**, *13* (19), 9869-9897.

43. Zheng, B.; Zhang, Q.; Zhang, Y.; He, K. B.; Wang, K.; Zheng, G. J.; Duan, F. K.; Ma, Y. L.; Kimoto, T., Heterogeneous chemistry: a mechanism missing in current models to explain secondary inorganic aerosol formation during the January 2013 haze episode in North China. *Atmos. Chem. Phys.* **2015**, *15* (4), 2031-2049.